Measurement of the W boson mass with the LHCb experiment

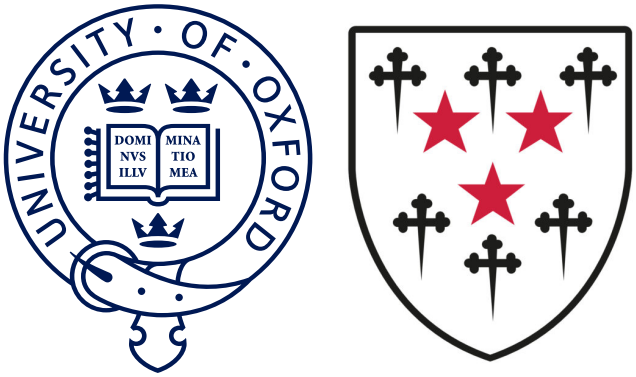

Martina Pili

Somerville College, University of Oxford

Supervisors: Dr. Mika Vesterinen, Prof. Guy Wilkinson

A thesis submitted for the degree of

Doctor of Philosophy

Trinity Term 2021

Acknowledgements

At the end of this journey, there are many people that I would like to thank.
My biggest thank you goes to Dr. Mika Vesterinen for his teaching, guidance, and patience over these years, and for allowing me to be part of such a challenging and fulfilling project.
I would like to thank Prof. Guy Wilkinson for the constant support and advice throughout the years, as well as Prof. Neville Harnew and the entire LHCb Oxford group for the encouragement and support during my DPhil.
A special thank you to the LHCb W mass team: Mika, Olli, Will, Steve, Ross and Miguel, it was a great privilege to work with you all!
I would like to extend my gratitude to the Science and Technology Facilities Council (STFC) and the Oxford Particle Physics Sub-Department for providing my funding and for allowing me to live a formative and rewarding experience at CERN.
I am very grateful to Sue Geddes and Kim Proudfoot for having been a reference point during the entire DPhil with their help.
To my Italian family abroad - Fabio, Luigi, and Maria Giovanna - thank you for the laughs and dinners between Oxford and Geneva. A special thank you to Maria Giovanna, for her endless friendship and for having shared this experience with me from the very first day.
A very special thank you to Blaise for all the love, support, and for being the best partner along this journey and in life.
Finally, I would like to dedicate this work to my family, Mamma, Papà e Vale for their encouragement, the countless phone calls, and for making sure that I always bring a little piece of Sardinia with me wherever I go :)

Declaration of originality

I declare that this dissertation is an original report of my research, has been written by me and has not been submitted for another qualification to this or any other university. The measurement of the W boson mass presented in this thesis is the result of a collaboration with a number of others. For completeness and necessary context, I have presented a full overview of the analysis. The collaborative contributions, particularly in Chapters 5 and 8, have been indicated clearly and acknowledged. Due references have been provided on all supporting literatures and resources. My main contributions to the analysis are presented in Chapters 2, 6 and 7. Additional personal contributions to the LHCb detector performance work are reported in Chapter 4.

Oxford, October 26, 2021 Martina Pili

Abstract

Precision measurements of electroweak parameters permit fundamental consistency tests of the Standard Model of Particle Physics. The resulting constraints on physics beyond the Standard Model are primarily limited by the precision of direct measurements of the mass of the W boson (m_W). Over the past thirty years, many experiments have performed measurements of m_W, but an improvement in its precision is still needed. This thesis presents the first measurement of m_W by the LHCb experiment at the facilities of the European Organization for Nuclear Research (CERN) in Geneva. This measurement is based on data collected by LHCb during the year 2016 at centre-of-mass-energy $\sqrt{s} = 13\,\text{TeV}$. A simultaneous fit is performed on the q/p_T distribution of a sample of $W \to \mu\nu$ decays and the ϕ^* distribution of a sample of $Z \to \mu\mu$ decays. The value of m_W is determined to be

$$m_W = 80354 \pm 23_{\text{stat}} \pm 10_{\text{exp}} \pm 17_{\text{theory}} \pm 9_{\text{PDF}}\ \text{MeV},$$

based on an arithmetic average of results with three different Parton Distribution Function sets. This is considered a *pathfinder* measurement aimed at starting discussions with the theory and experimental community to reduce the still large systematic uncertainties on m_W. The new methodologies and strategies adopted for this work lay the foundation of what will be the *legacy* measurement with the full dataset collected between 2015 and 2018. While this thesis describes the full measurement, greater detail will be given to the treatment of two of the most important sources of systematic uncertainty on the theoretical and experimental side, namely the Parton Distribution Functions and the measurement of the muon momenta. New methods, published in peer-reviewed journals, and *ad hoc* strategies have been developed to reduce their associated systematic uncertainties. Some of these studies have been applied to the proof-of-principle measurement described in this thesis. The others will be extremely important in the attempt of reducing the total uncertainty in future measurements of m_W.

Contents

List of Figures **xi**

List of Tables **xv**

Glossary **xvii**

Introduction **1**

1 Theoretical background **5**
1.1 The Standard Model of Particle Physics 5
1.1.1 Strong interactions 6
1.1.2 Electroweak interactions 7
1.2 Measurement of the W boson mass: state of the art 10
1.3 W and Z boson production at hadron colliders 12
1.3.1 Phenomenology of hadron collisions 12
1.3.2 Vector bosons production and decay 16
1.3.3 Measuring m_W at hadron colliders 18

2 Parton Distribution Functions and the W mass measurement **21**
2.1 Motivations 21
2.2 Simulation of W production 23
2.3 Fitting method 24
2.4 Understanding the PDF uncertainties 26
2.5 PDF uncertainty reduction 29
2.5.1 Simultaneous fit of W^+ and W^- samples 34
2.5.2 Dependence on the detector acceptance 36
2.6 Summary 37

3 The LHCb experiment at the LHC **41**
3.1 The Large Hadron Collider 41
3.2 The LHCb detector 43
3.2.1 The Vertex Locator 43
3.2.2 The Magnet and Tracking system 44

3.2.3 The Ring Imaging Cherenkov detectors . . . 49
3.2.4 The calorimeters . . . 50
3.2.5 The muon stations . . . 52
3.2.6 The trigger system . . . 54
3.2.7 Simulation . . . 58

4 RICH1 quality assurance measurements for the LHCb Upgrade I 59
4.1 The LHCb Upgrade I . . . 59
4.2 The RICH1 quartz windows . . . 62
4.3 Transmission measurements . . . 63
4.3.1 The transmission spectrum . . . 63
4.3.2 Direct measurements . . . 66
4.4 Anti-reflecting coating . . . 69
4.5 Visual inspection for surface imperfections . . . 71
4.6 Summary . . . 74

5 Strategy of the *W* mass measurement 77
5.1 Overview of the analysis . . . 78
5.2 Dataset and selection . . . 80
5.3 Signal modelling . . . 82
5.3.1 Physics modelling . . . 84
5.3.2 QED Final state radiation . . . 89
5.3.3 Muon reconstruction efficiencies . . . 89
5.3.4 Isolation, impact parameter and track quality cut efficiency modelling . . . 91
5.3.5 Polarity weighting . . . 91
5.4 Background modelling . . . 92
5.5 Summary . . . 93

6 Determine curvature biases with the "pseudomass method" 95
6.1 Motivations . . . 95
6.2 The simulated event sample . . . 96
6.3 The pseudomass method . . . 97
6.4 Validation of the method . . . 100
6.5 Application of the method . . . 103
6.6 Impact of the pseudomass method on the measurement of electroweak observables . . . 109
6.7 Summary . . . 113

7 Muon momentum measurement **115**
7.1 Detector module level alignment 116
7.2 Fill dependent momentum scale calibration 118
7.3 Higher-level curvature corrections: the pseudomass method 120
7.4 Calibration of the muon momentum in the simulation 122
7.4.1 Test of the statistical coverage of the fit 127
7.5 Uncertainty on the muon momentum measurement model 129

8 The fit method and results **133**
8.1 Design of the fit 133
8.1.1 Parametric correction at high transverse momentum 136
8.2 Results with the nominal fit model 137
8.3 Postfit plots 138
8.4 Systematic uncertainties 139
8.5 Cross-checks 140
8.6 PDF uncertainties 142
8.7 Results 145
8.8 Prospects for future measurements of m_W at LHCb and the LHC . 146

Conclusion **146**

Appendices

A Event selection criteria used in the W mass measurement **153**

B Additional plots on the muon momentum calibration **155**

C Additional information on the W mass fit configuration **159**

References **163**

x

List of Figures

1.1 Running of α_s for different Q-values 7
1.2 Corrections to the W boson propagator 11
1.3 The relations between Standard Model observables 12
1.4 Schematic view of parton interactions 13
1.5 Examples of PDFs for different parton species 14
1.6 Bjorken-x values probed at different Q^2 and rapidities. 15
1.7 Feynman diagrams for the $W \to \ell\nu_\ell$ processes 17
1.8 Transverse momentum spectrum of vector bosons 17
1.9 Schematic representation of the Collins Soper frame. 18
1.10 Three hypothetical examples of muon p_T distribution from $W \to \mu\nu$ decays 19

2.1 The simulated muon p_T distributions for five different m_W hypotheses 24
2.2 The distribution of the χ^2 versus m_W for 1000 PDF replicas 25
2.3 The $W^\pm$ rapidity distributions decomposed into the main partonic subprocesses 27
2.4 The ratios of a subset of PDF replicas with respect to the central replica. 27
2.5 The variations in the shapes of the p_T^W, y and $\cos\theta^*$ distributions predicted with a subset of PDF replicas 30
2.6 The distributions of $\langle p_T^W \rangle$ and $\langle y \rangle$ for a subset of PDF replicas . . . 31
2.7 The variations in the shapes of the p_T and η distributions predicted with a subset of PDF replicas 31
2.8 The distribution of $\langle p_T \rangle$ and $\langle \eta \rangle$ produced using a subset of replicas of the NNPDF3.1 set and divided by the central replica 32
2.9 The distribution of the χ^2 versus m_W for 1000 PDF replicas: single toy dataset 33
2.10 The distribution of PDF uncertainty for 1000 toy datasets 33
2.11 The distribution of the W^- versus W^+ mass for 1000 PDF replicas 35
2.12 the distribution of χ^2 versus m_W for a one-dimensional and two-dimensional fit 35
2.13 The distribution of the PDF uncertainty for 1000 toy datasets . . . 36

2.14 PDF uncertainty as a function of the p_T range 37
2.15 PDF uncertainty as a function of the η range 37

3.1 CERN accelerators complex 42
3.2 Layout of the LHCb detector 44
3.3 A schematic diagram of the LHCb Vertex Locator 45
3.4 The primary vertex resolution along the x and z coordinates 45
3.5 The resolution of the x and y components of the impact parameter 46
3.6 The Silicon Tracker 46
3.7 Different types of track at LHCb 47
3.8 View of the LHCb magnet 48
3.9 Momentum resolution for LHCb long tracks 48
3.10 Optical scheme of the RICH detectors 49
3.11 Interaction of several particle species with different subdetectors . . 51
3.12 View of the LHCb muon system 53
3.13 workflow of the LHCb trigger during the Run 2 54

4.1 Scheme of the LHCb detector in the Upgrade I 61
4.2 Schematic drawing of the mechanical and optical system modifications of the upgraded RICH 1 detector 62
4.3 One of the quartz coupons delivered at CERN 64
4.4 Change in the intensity of a light beam passing through a glass plate 65
4.5 Transmission spectrum of Spectrosil® 2000 66
4.6 Setup of Perkin Elmer Lambda 650 UV-VIS spectrometer 67
4.7 Transmission spectra of four quartz coupons 68
4.8 Design of the Integration Sphere 69
4.9 Transmission spectra with standard setup versus integration sphere 70
4.10 Diffusion spectra of quartz coupons 70
4.11 Fresnel reflection and antireflective coating 71
4.12 Standard MIL-0-13830 72
4.13 Scratches in quartz plate number 2 73
4.14 Digs in quartz coupons 74
4.15 Digs in large plate number 6 74

5.1 Change in the muon q/p_T distribution from a 300 MeV shift in m_W 79
5.2 Variations in the $p_T^{W^+}$ spectrum for changes in α_s (left) and k_T^{intr} . . 84
5.3 The measurement of the A_0 and A_3 angular coefficients by the ATLAS collaboration. 85
5.4 Impact of the A_3 angular coefficient on the muon p_T shape 87
5.5 Validation of the candidate boson production models 88

5.6 The p_T distribution for candidates in the QCD background model . 93

6.1 Global mis-alignment in a simplified configuration of the LHCb detector 97
6.2 Representation of the angles that define the variable ϕ^* 99
6.3 The distribution of p_T^Z and the pseudomass for different cuts on ϕ^* . 99
6.4 The parametric fit of the M^+ and M^- pseudomass distributions in the presence of a $\Delta x = 50\,\mu\text{m}$ 100
6.5 Validation of the pseudomass method 101
6.6 The pseudomass asymmetry in bins of the muon η 102
6.7 The pseudomass corrections for different examples of misalignment . 104
6.8 Impact of the pseudomass method on alignment-sensitive quantities 105
6.9 Impact of the pseudomass method on alignment-sensitive quantities: profile plots 107
6.10 Impact of the pseudomass method on alignment-sensitive quantities: profile plots for multiple toy data sets 108
6.11 The pull distributions for 90 toy measurements of m_{W^+} and $\sin^2\theta^{\text{eff}}_{\text{lept}}$ 111
6.12 The shift in the extracted (left) m_{W^+} and (right) $\sin^2\theta^{\text{eff}}_{\text{lept}}$ values with respect to the reference value, in 90 toys 112

7.1 Minimisation of track residuals 116
7.2 Dimuon invariant mass of the 2016 $Z \to \mu\mu$ sample 118
7.3 Fill dependent momentum scale calibration 119
7.4 Muon $1/p_T$ distributions in magnet-up and magnet-down data after the Z custom alignment 120
7.5 The pseudomass corrections applied to data and simulation as a function of the bin index 121
7.6 The dimuon invariant mass distribution before and after pseudomass corrections 122
7.7 Three alignment-sensitive quantities before and after pseudomass corrections 123
7.8 Muon $1/p_T$ distributions in magnet-up and magnet-down data after the pseudomass alignment 123
7.9 Correlations between momentum scale fit parameters 126
7.10 The dimuon mass distributions for selected J/ψ, $\Upsilon(1S)$ and Z candidates. All fit categories with both muons within the $2 < \eta < 4.4$ region are combined. The data are compared with the postfit model of simulation plus (for the quarkonia models) background. 127
7.11 Results of the coverage test for one of the 200 toys 129
7.12 The pull distributions for 200 toys, for each parameter of the detector response model 130

8.1 Implementation of the k-factor 136
8.2 Projections of the W and Z terms from the fit 138
8.3 Postfit plots for the Z sample 139
8.4 The χ^2 versus δm_W distribution including all model variations considered 141
8.5 The χ^2 versus m_W distribution including all PDF variations considered 145
8.6 Summary of measurements of m_W 148

B.1 Momentum scale postfit plots for the Z sample 156
B.2 Momentum scale postfit plots for the $\Upsilon(1S)$ and J/ψ samples . . . 157

List of Tables

1.1 Elementary particles in the Standard Model 6

3.1 `isMuon` criteria for different muon momentum ranges 53

5.1 The W selection cuts 81
5.2 The Z selection cuts 81

6.1 The bias in the pull distributions used to validate and correct the pseudomass method. 103
6.2 The biases in the values of m_{W^+}, m_{W^-} and $\sin^2\theta^{\text{eff}}_{\text{lept}}$ for different examples of mis-alignment 108
6.3 Biases in m_W for a 5 µm mis-alignment along x before and after pseudomass corrections 111

7.1 η-dependent categorisation of the momentum scale fit mass plots . . 125
7.2 Postfit values of the six parameters in the momentum smearing model. 126
7.3 Statistics for a single toy in the statistical coverage study 128

8.1 The postfit values of the m_W fit with the NNPDF3.1 PDF set. The uncertainties quoted are statistical. 138
8.2 List of contributions to the systematic uncertainty on m_W. Negligible contributions are not listed. 140
8.3 A list of m_W fit results where the data and simulation samples are split into two orthogonal subsets. The uncertainties quoted are only statistical. 142
8.4 A list of m_W fit results with variations in the fit range around the default $p_T^{\text{min}} = 28\,\text{GeV}$ and $p_T^{\text{min}} = 52\,\text{GeV}$. The second column reports the χ^2 values, the third column reports the shifts in m_W with respect to the default fit and the third column lists the statistical uncertainties on m_W. 143
8.5 A list of m_W fit results with variations in which physics parameters are floating. 143
8.6 PDF uncertanties in the m_W determination 144

A.1 The Υ selection cuts 153
A.2 The J/ψ selection cuts 154
A.3 The W selection cuts 154
A.4 The Z selection cuts 154

C.1 Summary of the components included in the Z term in the default m_W fit configuration. 160
C.2 Summary of the components included in the W term in the default m_W fit configuration. 160
C.3 The fiducial regions and cross-sections that are assumed in in the m_W fit. 161

Glossary

ALICE . . . . A Large Ion Collider Experiment

ATLAS . . . . A Toroidal LHC ApparatuS

CMS . . . . . Compact Muon Solenoid (experiment)

CB . . . . . CrystalBall (function)

CDF . . . . . the Collider Detector at Fermilab

CT18 . . . . . one of the Parton Distribution Function's sets used in this analysis

DYTurbo . . . one of the Monte Carlo generators used in this analysis

D0 . . . . . collider experiment at Fermilab

ECAL . . . . . Electromagnetic Calorimeter (for the LHCb detector)

EW . . . . . Electroweak

FSR . . . . . Final State Radiation

HCAL . . . . . Hadronic Calorimeter (for the LHCb detector)

HLT1(2) . . . High Level Trigger 1(2)

IP . . . . . Impact Parameter

ISR . . . . . Initial State Radiation

IT . . . . . Inner Tracker

LEP . . . . . Large Electron Positron collider

LHC . . . . . Large Hadron Collider

LHCb . . . . . Large Hadron Collider beauty (experiment)

MC . . . . . Monte Carlo

MINUIT . . . numerical minimization computer program

MSHT . . . . . one of the Parton Distribution Function's sets used in this analysis

(N)LL . . . . . (Next to) Leading Log (approximation)

(N)LO . . . . . (Next to) Leading Order (approximation)

NNPDF . . . . one of the Parton Distribution Function's sets used in this analysis

OT . . . . . Outer Tracker

PID . . . . . Particle Identification

PDF . . . . . Parton Distribution Function

POWHEG . . one of the Monte Carlo generators used in this analysis

Pythia . . . . . one of the Monte Carlo generators used in this analysis

QA . . . . . Quality Assurance

QCD . . . . . Quantum Chromodynamics

QSUM . . . . Quadrature sum

RICH . . . . . Ring Imaging CHerenkov (detector)

RMS . . . . . Root Mean Square

SM . . . . . Standard Model

SPD . . . . . Scintillating Pad Detector

TT . . . . . Trigger Tracker

VELO . . . . . VErtex LOcator (detector)

Introduction

Global fits to precision electroweak (EW) observables are a powerful probe of physics beyond the Standard Model, but their sensitivity is currently limited by the precision of the W boson mass (m_W) measurement. The precise determination of m_W is an important consistency test of the Standard Model, as it is related to the well measured Higgs boson and top quark masses via loop-induced radiative corrections. Beyond the Standard Model fields might contribute as additional corrections to the W boson propagator. A global fit to precision electroweak data, excluding direct measurements of m_W, yields a Standard Model prediction of $m_W = 80.354 \pm 0.007\,\text{GeV}$ [1]. The W boson was discovered at the CERN proton-antiproton collider (Sp$\bar{\text{p}}$S) and its first mass measurement, $m_W = 81 \pm 5\,\text{GeV}$ [2], was consistent with the Standard Model prediction at that time. Measurements of m_W at the CERN electron-positron collider LEP and in proton-antiproton collisions at the Tevatron by the CDF and D0 experiments followed, with a combined uncertainty of 16 MeV [3, 4]. At the Large Hadron Collider (LHC), ATLAS was the first experiment to measure m_W. The result, $m_W = 80.370 \pm 0.019\,\text{GeV}$ [5] is as precise as the CDF standalone measurement. The combination of the ATLAS, Tevatron and LEP results yields $m_W = 80.379 \pm 0.012\,\text{GeV}$ [6], which is still less precise than the Standard Model prediction. An improvement in the precision of the direct measurement is therefore well justified.

At hadron colliders, W bosons are produced mainly via the annihilation of a quark and an antiquark. At the Tevatron collider W bosons were primarily produced by the annihilation of a valence quark from the proton and a *valence* antiquark from the antiproton. The LHC is a more challenging environment to measure m_W than LEP or the Tevatron because of the phenomenology of its proton-proton collisions (pp). In contrast to proton-antiproton ($p\bar{p}$) collisions, at the LHC only

sea antiquarks contribute to W production. It is therefore important to know the Parton Distribution Functions (PDFs) for sea quarks, and particularly for second generation quarks, since roughly 20% of the W production at the LHC involves at least one of them (in contrast to the 5% contribution at the Tevatron).

The LHCb detector [7] at the LHC is a single-arm *forward* spectrometer, with full charged particle tracking and identification capabilities in an acceptance region that is almost complementary to the so-called *central* region sampled by ATLAS and CMS. A previous study [8] suggests that a measurement of m_W by LHCb would have a great impact in a combination with the other LHC experiments because of the predicted partial anti-correlation of the PDF uncertainties between measurements in the central and forward rapidity regions. Further studies to understand what drives this source of uncertainty and how to reduce it in a standalone measurement of m_W by LHCb have been performed [9]. Given the need of improvement in the precision and the interesting findings of Ref. [8], it is worth tackling the challenge of a m_W measurement with LHCb.

This thesis reports the first measurement of m_W at LHCb using $W \to \mu\nu$ decays from a subset of events collected by the experiment between 2015 and 2018 [10]. This *proof-of-principle* measurement presents novel techniques to reduce the dominant sources of uncertainty which previous results at other experiments identified in the W production modelling and the lepton momentum measurement calibration. While this thesis shows that the experimental sources of systematic uncertainty are quite under control at LHCb, more work needs to be done to further reduce the theory uncertainties. This requires a joint effort between theory and experimental groups. Even though the theory community made huge improvements over the years in providing more reliable tools to predict the kinematics of vector boson production and decay, further improvements are needed. The present work aims at becoming a benchmark for discussion with the theory community, such that the subsequent *legacy* measurement of m_W at LHCb (which will use a much larger dataset) will benefit from the discussion and collaboration with the rest of the community.

The present thesis work is articulated in eight chapters. Chapter 1 provides a brief introduction of the Standard Model of Particle Physics, the basic analytic formulation to understand the key elements of the m_W measurement, and the state-of-the-art of measurements of m_W at hadron colliders. Chapter 2 summarises the results of a phenomenology study performed on simulated events, to understand the PDF uncertainties in a measurement of m_W at LHCb and propose a method to reduce them. Chapter 3 provides a general description of the LHCb detector and highlights the components that are of primary importance for the measurement of m_W. Chapter 4 briefly describes how the LHCb detector will change in view of the Upgrade I. In this context, quality assurance measurements performed at CERN on the upgraded RICH1 detector will be discussed. Chapter 5 describes the strategy adopted to perform the m_W measurement. Since the main contribution of the author's thesis to the present analysis is the muon momentum calibration, two chapters are dedicated to this topic. Chapter 6 describes a new method developed to correct for detector misalignment effects at hadron collider experiments. The application of the method to real data, as well as the full muon momentum calibration in the m_W measurement is described in Chapter 7. Finally, Chapter 8 reports the extraction of m_W from a fit to data and simulated events, and the estimation of the uncertainties associated to it.

It is anticipated that, for brevity, natural units with $c = 1$ are used throughout the text and the majority of the figures, with exception of some figures from separate studies or publications.

1 Theoretical background

This chapter introduces the basic theoretical formalism of the Standard Model and its fundamental symmetries. The importance of a precise measurement of the W boson mass in the understanding of the theory and its role in the search for physics beyond the Standard Model is highlighted.

1.1 The Standard Model of Particle Physics

The Standard Model (SM) [11–13] is, at the time of writing, the most accurate theory describing the known elementary particles in nature and their interactions. According to the SM, the fundamental constituents of matter are twelve spin-$\frac{1}{2}$ *fermions*, namely six *quarks* and six *leptons*, each with an anti-matter equivalent. Fermions interact via three fundamental forces, mediated by five spin-1 *bosons*: the photon (γ), the $W^{\pm}$ and Z^0 and the gluon (g) are the mediators of *electromagnetic*, *weak* and *strong* forces, respectively. A fourth fource, the *gravitational* force, is not described by the SM. An additional spin-0 particle, the *Higgs* boson (H), provides the mechanism that makes the W and Z bosons massive particles, while the photon remains massless. Table 1.1 summarises the fundamental particles described by the SM. Quantum field theory provides the mathematical framework for the SM, in which particles and their interactions are described in terms of fields defined

Table 1.1: The elementary particles of the Standard Model.

	Fermions			Bosons
Leptons:	$\begin{pmatrix} e^- \\ \nu_e \end{pmatrix}$	$\begin{pmatrix} \mu^- \\ \nu_\mu \end{pmatrix}$	$\begin{pmatrix} \tau^- \\ \nu_\tau \end{pmatrix}$	$\gamma, W^\pm, Z^0, g$
Quarks:	$\begin{pmatrix} u \\ d \end{pmatrix}$	$\begin{pmatrix} c \\ s \end{pmatrix}$	$\begin{pmatrix} t \\ b \end{pmatrix}$	H

at every point of space-time, with a Lagrangian term controlling their dynamics. The theory formalism is built under the requirement that the SM Lagrangian is invariant under *local gauge transformations*, i.e. assuming a transformation of the field like $\psi \rightarrow \psi e^{i\phi(x)}$, where local specifies that the phase (ϕ) depends on the space-time coordinates (x). This requires the existence of gauge bosons and their interaction with the fermion fields. The strength of each interaction described in the SM is regulated by a coupling parameter which varies with the interaction energy scale. In its mathematical formulation, the SM is a $SU(3)_C \times SU(2)_L \times U(1)_Y$ gauge theory, where $SU(3)_C$, $SU(2)_L$ and $U(1)_Y$ are the gauge groups of colour, weak isospin and hypercharge, respectively. More details on each interaction will be given in the following sections.

1.1.1 Strong interactions

The strong interaction is described by the theory of Quantum Chromodynamics (QCD). The interaction is mediated by eight massless gluons corresponding to the eight generators of the $SU(3)_C$ local gauge symmetry group. The single electric charge of Quantum Electrodynamics (QED) is replaced by three conserved *colour* charges, which are three orthogonal states in the SU(3) colour space. The coupling with gluons happens only between particles that have colour charge, such as quarks. Leptons are colour neutral, and therefore do not experience the strong force. The QCD coupling constant associated to colour exchange at the interaction vertex is denoted with α_s. The running of the QCD coupling constant with the energy

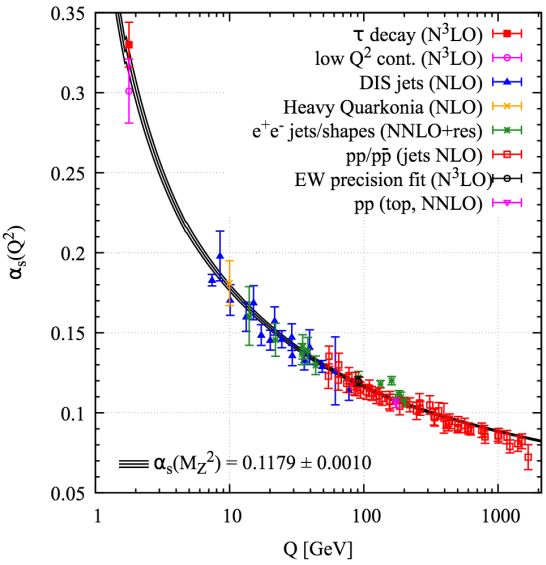

Figure 1.1: Running of the α_s coupling for different Q-values [6].

scale Q, for n_f quark flavours, is given by

$$\frac{d\alpha_s}{d\log Q} = -\Big(11 - \frac{2n_f}{3}\Big)\frac{\alpha_s^2}{2\pi} + \mathcal{O}(\alpha_s^3). \tag{1.1}$$

This means that at low energy scales α_s is large (i.e. α_s $\mathcal{O}(1)$), leading to the *confinement* of quarks in colourless hadrons. In this regime, perturbation theory can not be used to describe the associated physics phenomena. At $Q > 100$, which is the typical scale of modern high-energy collider experiments, $\alpha_s \sim 0.1$, which is sufficiently small for perturbation theory to be a valid computational approach. This feature of QCD is called *asymptotic freedom*. Figure 1.1 [6] shows several measurements of α_s at different values of the energy scale Q.

1.1.2 Electroweak interactions

The theoretical unification of the electromagnetic and weak forces into a single electroweak theory was postulated in 1960 by Glashow, Weinberg and Salam [11, 13] in the GSW model. The weak interaction is described by the $SU(2)_L$ gauge group, where the subscript L denotes that the gauge interaction only affects left-handed chirality particles and right-handed chirality antiparticles. In this picture leptons

are represented as left-handed isospin *doublets*

$$L_e = \begin{pmatrix} e^- \\ \nu_e \end{pmatrix}_L \quad L_\mu = \begin{pmatrix} \mu^- \\ \nu_\mu \end{pmatrix}_L \quad L_\tau = \begin{pmatrix} \tau^- \\ \nu_\tau \end{pmatrix}_L , \tag{1.2}$$

and right-handed isospin *singlets* $R_{e,\mu,\tau} = e_R, \mu_R, \tau_R$, which are unaffected by $SU(2)_L$ and do not couple with the gauge bosons of the symmetry. In a similar way, quarks are represented as left-handed isospin doublets

$$L_{ud'} = \begin{pmatrix} u \\ d' \end{pmatrix}_L \quad L_{cs'} = \begin{pmatrix} c \\ s' \end{pmatrix}_L \quad L_{tb'} = \begin{pmatrix} t \\ b' \end{pmatrix}_L , \tag{1.3}$$

and right-handed isospin singlets $u_R, c_R, t_R, d_R, s_R, b_R$. The weak eigenstates (d', s', b') are related to the physical (mass) eigenstates via the Cabibbo-Kobayashi-Maskawa (CKM) matrix [14, 15]

$$\begin{pmatrix} d' \\ s' \\ b' \end{pmatrix} = \begin{pmatrix} V_{ud} & V_{us} & V_{ub} \\ V_{cd} & V_{cs} & V_{cb} \\ V_{td} & V_{ts} & V_{tb} \end{pmatrix} \begin{pmatrix} d \\ s \\ b \end{pmatrix} . \tag{1.4}$$

The magnitude of the CKM matrix elements determines the strength of the weak interaction between physical up-type and down-type quarks. The $SU(2)_L$ group has three generators, T_1, T_2 and T_3. Each generator is associated to a gauge field $W_\mu^{(1),(2),(3)}$, corresponding to three gauge bosons $W^{(1),(2),(3)}$. The *physical* W bosons, i.e. W^+ and W^-, can be expressed as linear combinations of $W^{(1)}$ and $W^{(2)}$. However, the Z boson cannot coincide with $W^{(3)}$ because experiments have proved that Z bosons can couple also to right-handed particles [16], which is forbidden in the $SU(2)_L$ symmetry. Given that the gauge fields associated to the Z boson and the photon are both neutral, the GSW model proposes to express them as combinations of two neutral gauge bosons, one of which is $W^{(3)}$. The $U(1)_Q$ gauge symmetry of electromagnetism is replaced with a new $U(1)_Y$ local gauge symmetry, associated to a new boson denoted as B and a new quantum number, the weak hypercharge (Y_W). The weak hypercharge can be expressed in terms of the third component of the weak isospin ($I_W^{(3)}$) and the electric charge (Q):

$$Y_W = 2(Q - I_W^{(3)}) \tag{1.5}$$

According to the GSW model, for invariance under $U(1)_Y$ and $SU(2)_L$ local gauge transformations, the weak hypercharges of the particles in a weak isospin doublet must be the same (i.e. $Y_{e_L} = Y_{\nu_L}$). The gauge fields B and $W^{(3)}$ mix to give the physical γ and Z bosons. The fact that they can be expressed by linear combinations of fields corresponding to the generators of $SU(2)_L$ and $U(1)_Y$ represents the essence of the electroweak unification:

$$\begin{pmatrix} Z \\ \gamma \end{pmatrix} = \begin{pmatrix} \cos\theta_W & \sin\theta_W \\ -\sin\theta_W & \cos\theta_W \end{pmatrix} \begin{pmatrix} W^{(3)} \\ B \end{pmatrix}, \tag{1.6}$$

where θ_W is the angle that relates the coupling constants of the $SU(2)_L$ and $U(1)_Y$ groups, g and g':

$$\tan\theta_W = \frac{g'}{g}. \tag{1.7}$$

At the lowest order in the electroweak theory (denoted as "tree level"), the SM predicts a relation between the mass of the W and Z bosons via the θ_W angle:

$$\cos\theta_W = \frac{m_W}{m_Z}. \tag{1.8}$$

The electroweak Lagrangian does not contain mass terms for the gauge bosons since such terms would violate local gauge invariance. In a symmetric gauge theory, therefore, the gauge bosons must be massless. This is in fact true for photons and gluons. However, for the weak interaction the symmetry must somehow be broken since the W and Z bosons are known to be massive. Spontaneous symmetry breaking is a way to break the symmetry of a theory, preserving local gauge invariance and keeping the theory renormalisable. A complex scalar field known as the *Higgs* field (ϕ) in a scalar potential of the form:

$$V(\phi) = -\mu^2\phi^\dagger\phi + \lambda(\phi^\dagger\phi)^2 \tag{1.9}$$

is introduced. The vacuum state is the lowest energy state of the field ϕ, and correspond to the minimum of $V(\phi)$. If $\mu^2 < 0$ the resulting potential has a minimum at $\phi = 0$. However, if $\mu^2 > 0$, the lowest energy state does not occurr at $\phi = -0$. Instead the minimum of the potential is found for $\phi^\dagger\phi = -\mu^2/2\lambda \equiv v^2/2$

and the field is said to have a non-zero vacuum expectation value v. Since the potential is symmetric, there are two possible vacuum states. The choice of the vacuum state is known as *spontaneous symmetry breaking*. When the Lagrangian of the theory is written by expanding the Higgs field around the vacuum state, $\phi(x) = v + h(x)$, the previously massless gauge fields acquire mass terms, thus allowing the associated gauge bosons to be massive:

$$m_W = \frac{vg}{2} \quad \text{and} \quad m_Z = \frac{v\sqrt{g^2 + g'^2}}{2}, \tag{1.10}$$

whilst allowing the photon to remain massless. The mass of the W boson (m_W) is therefore determined by the coupling constant of the $SU(2)_L$ gauge interaction (g) and the vacuum expectation value of the Higgs field. The Higgs mechanism for the spontaneous symmetry breaking of the $SU(2)_L \times U(1)_Y$ gauge group of the SM can also be used to generate the masses of fermions [17].

1.2 Measurement of the *W* boson mass: state of the art

At tree level the W boson mass (m_W) can be expressed as a function of the Higgs vacuum expectation value and the weak isospin coupling as shown in Eq. 1.10. Going beyond tree level the boson masses and couplings receive loop-level corrections. The W mass can be related to the Z boson mass (m_Z), the fine-structure constant (α) and the Fermi constant (G_F) by [18, 19]:

$$m_W^2(1 - \frac{m_W^2}{m_Z^2}) = \frac{\pi\alpha}{\sqrt{2}G_F}(1 + \Delta), \tag{1.11}$$

where the term Δ includes all the additional contributions to m_W arising from higher order corrections to the W boson propagator. These are driven by the gauge couplings and the masses of heavy particles in the SM, such as the top quark and the Higgs, as shown in Fig. 1.2. New particles and interactions which are often implied by theories beyond the SM could have a non-negligible effect on m_W through these corrections. Therefore, the precise measurement of m_W represents a fundamental test of the internal consistency of the SM and a probe

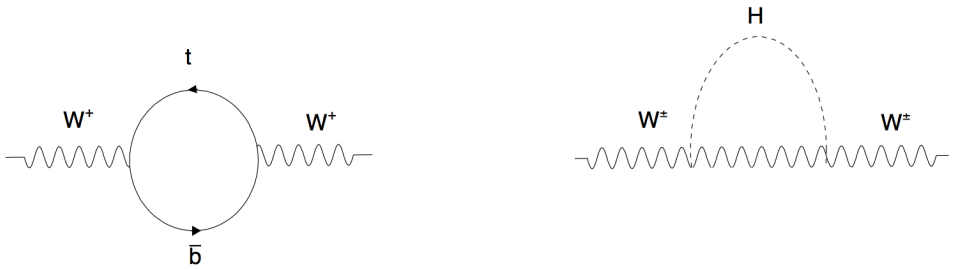

Figure 1.2: The corrections to the W boson propagator from the top quark (left), and Higgs boson (right).

of the possible existence of New Physics. As far as *direct* measurements of m_W are concerned, the most updated average is [6]

$$m_W^{\mathrm{PDG}} = 80379 \pm 12 \text{ MeV}. \tag{1.12}$$

This average is dominated by the results [3, 4, 20] of the CDF and D0 experiments at the Tevatron collider in proton-antiproton ($p\bar{p}$) collisions, and by the most recent ATLAS [5] measurement at the Large Hadron Collider (LHC) in proton-proton ($p\bar{p}$) collisions. The CMS experiment at the LHC [21] has performed a W-like measurement of the Z boson mass [22], using events with a Z boson decaying into a pair of oppositely charged muons and where one muon is removed from the event to mimic the $W \to \mu\nu$ decay topology. This proof-of-principle measurement is intended as a validation of the analysis techniques developed for a high precision measurement of m_W. At the time of writing, no measurement of m_W has been published by CMS.

Global fits to the electroweak parameters put stringent constraints on the prediction for m_W in the SM. A global fit of electroweak observables, excluding measurements of m_W, yields a prediction of [1]

$$m_W^{\mathrm{pred.}} = 80354 \pm 7 \text{ MeV}, \tag{1.13}$$

thus highlighting that an improvement in the precision of the direct measurement (Eq. 1.12) is needed. Figure 1.3 shows the relation among the masses of the top quark (m_t), the Higgs boson (m_H) and the W boson (m_W) within the SM. The grey contour represents the region of phase-space accessible without including the direct measurements of m_W, m_t and m_H. The direct measurements of these parameters

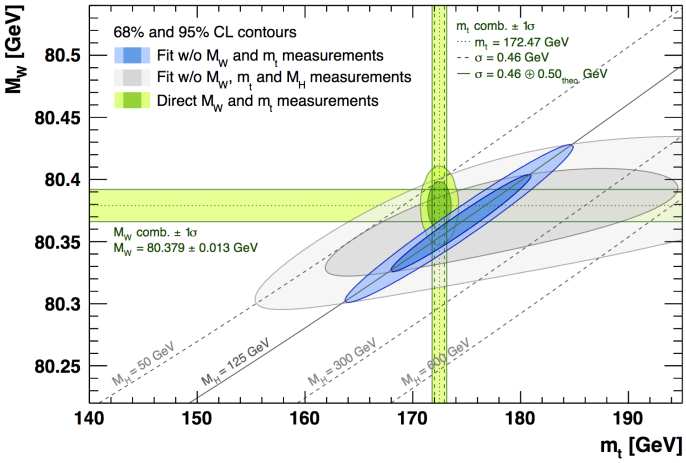

Figure 1.3: The relation among the masses of the top quark (m_t), the Higgs boson (m_H) and the W boson (m_W) within the SM. The grey contour represents the region of phase-space accessible without including the direct measurements of m_W, m_t and m_H. The direct measurements of these parameters restrict the range to the green and blue bands.

restrict the range to the green bands and the blue ellipse. It should be noted that the blue ellipse corresponds to the result of the global fit *including* the measured m_H as input [23, 24]. This greatly constrains the SM prediction for m_W. The green and blue bands cross each other within uncertainty (hinting a consistency within the SM), but an improvement in the precision of the measurement of m_W can definitively confirm or disprove such hypothesis.

1.3 *W* and *Z* boson production at hadron colliders

In order to accurately measure m_W at hadron colliders it is crucial to understand the physics behind the production and decay of vector bosons. The following sections briefly describe the phenomena that characterise these processes.

1.3.1 Phenomenology of hadron collisions

The interaction between high energy quarks and gluons, generally referred to as *partons*, within the hadron can be split into several stages. The entire sequence is summarised in Fig. 1.4. The first step is the *hard scattering* process, which is the

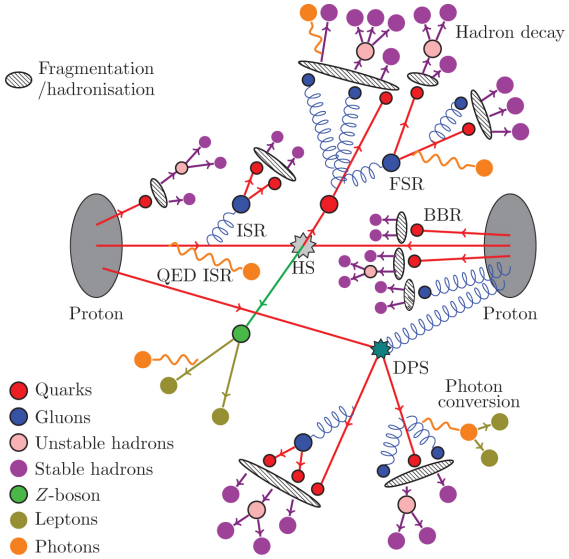

Figure 1.4: Schematic view of parton interactions, from the hard scattering process to the hadronisation, from Ref. [25].

fundamental interaction between partons, after which new particles are produced. This can be anticipated by emission of *initial state radiation* (ISR) from the incoming partons, and is typically followed by the radiation of additional partons by the outgoing partons (both processes are commonly referred to as *showering*), and by the emission of final state radiation (FSR). Once the partons energy approaches the $Q \sim 100$ threshold mentioned in Eq. 1.1, the confinement regime is restored. The *hadronisation* process is responsible for the production of *jets* of colourless hadrons. The centre-of-mass energy of the hard scattering process ($\sqrt{\hat{s}}$) can be expressed in terms of the centre-of-mass energy of the hadron-hadron collisions ($\sqrt{s}$)

$$\hat{s} = (x_1 p_1 + x_2 p_2)^2 \approx x_1 x_2 s, \tag{1.14}$$

where $p_{1,2}$ are the four-momenta of the two colliding hadrons and $x_{1,2}$ are the fractions of the hadron momenta carried by the partons contributing to the process (also known as "Bjorken-x"). These fractions are distributed according to the so called *Parton Distribution Functions* (PDFs), and depend on the parton species and the Q^2 value of the collision. PDFs are extracted by fitting various hadron-hadron and hadron-lepton scattering data over a range of x and Q^2 values. Examples of PDFs for different parton species at $Q^2 = 10^4\,\text{GeV}$ (corresponding to $\sqrt{\hat{s}} \approx m_W$),

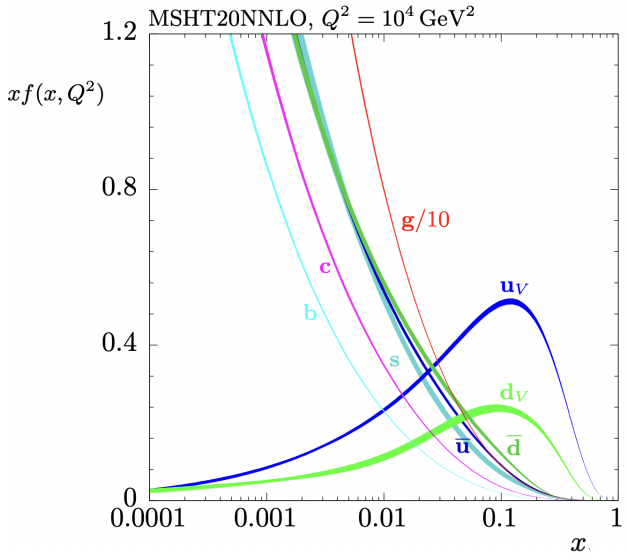

Figure 1.5: Examples of PDFs for different parton species at $Q^2 = 10^4\,\mathrm{GeV}$, from the MSHT set [26].

from the MSHT group [26], are shown in Fig. 1.5. Other sets of PDFs are available from different groups, such as CTEQ [27] and NNPDF [28]. Extrapolation of the PDFs to different Q^2 values is controlled by the Dokshitzer-Gribov-Lipatov-Altarelli-Parisi (DGLAP) equations of QCD [29–31].

Finally, the cross section $\sigma_{AB\to X}$ for the production of the final state X from two colliding hadrons A and B can be factorised in terms of the hard scattering cross section $\sigma_{ab\to X}$ involving partons a and b:

$$\sigma_{AB\to X} = \sum_{a,b} \int_0^1 \int_{x_b=0}^{x_b=1} dx_a dx_b f_a(x_a, Q^2) f_b(x_b, Q^2) \sigma_{ab\to X}(x_a, x_b, Q^2, \mu_F, \mu_R), \tag{1.15}$$

where $f_{a,b}$ is the PDF for partons a and b, μ_F is the factorisation scale, which separates the long-distance, non-perturbative interactions from the hard scattering and μ_R is the renormalisation scale. At a fixed order QCD calculation the factorisation and renormalisation scales are arbitrary parameters, but the cross section calculated using all orders of the perturbative expansion should not depend on them. The sum in Eq. 1.15 runs over all the possible pairs of partons that can contribute to the hard scattering. The integral runs over the fraction of the hadron momentum carried by the considered partons.

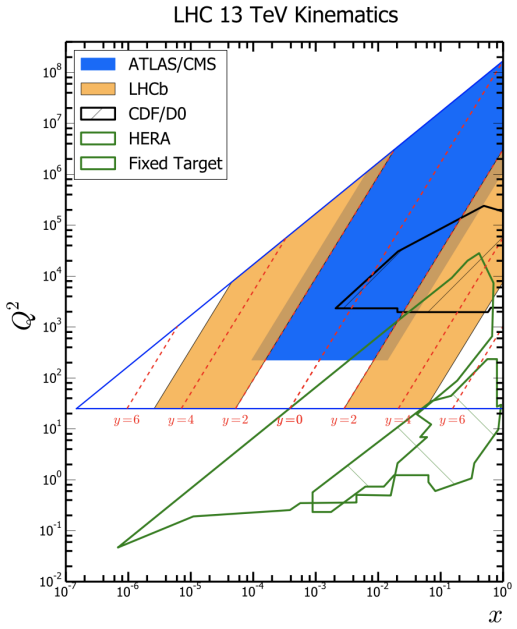

Figure 1.6: Bjorken-x values probed at different Q^2 and rapidities.

Different ranges of Bjorken-x can be probed depending on $\sqrt{s}$, Q^2 and the rapidity ($y = \frac{1}{2}\frac{E+p_L}{E-p_L}$, where E and p_L are the energy and the component of the momentum along the beam axis, respectively) of the vector boson produced in the collision. These quantities are related by the simple equation:

$$x_{1,2} = \frac{m}{\sqrt{s}} e^{\pm y}, \tag{1.16}$$

where $x_{1,2}$ are the Bjorken-x values of the incoming partons and m is the centre-of-mass energy of the hard scattering process. Figure 1.6 shows the values of x that can be probed by the experiments at the Large Hadron Collider at CERN and by other fixed-target experiments. It can be clearly seen that the LHCb experiment, which will be the focus of this thesis, probes an almost complementary range of x values with respect to ATLAS and CMS. The majority of the collisions analysed by LHCb involve a low-x parton and a high-x (*boosted*) parton. This difference between LHCb and the other experiments is crucial for precision electroweak measurements at the Large Hadron Collider, especially in view of the *combination* of such measurements, as will be explained in the following chapters.

1.3.2 Vector bosons production and decay

At lowest order (LO) in perturbation theory, electroweak vector bosons are produced with zero transverse momentum (i.e. $p_T^V = 0$, with $V = Z, W$). However, at next-to-leading order (NLO) in α_s, an incoming quark can radiate a gluon thus generating a non zero p_T, as shown in Fig. 1.7 (right) in the case of W boson production (it is also possible to have processes like $qg \to Vq$, where a jet recoils against the vector boson). If the emitted gluon has low momentum (*i.e.* it is a *soft* gluon), the process is called *infrared* divergent. The presence of divergences complicates the description and modelling of the vector boson transverse momentum at low p_T. The coefficient of α_s^n in the differential cross section contains a $1/p_T^2$ term, multiplied by a series of logarithms $\log^m(Q^2/p_T^2)$, with $m = 0, 1, ..., 2n-1$, that diverges at low p_T. This problem can be overcome by expressing the expansion in powers of α_s in terms of the logarithms as the Taylor expansion of an exponential. The large logarithms are thus "resummed" to all orders in α_s [32, 33] giving a finite result. This result is then matched to the fixed order calculation. The accuracy of the resummation depends on the order of the logarithms considered, therefore many applications distinguish between the leading-log (LL), next-to-LL (NLL) and next-to-NLL (NNLL) approximations. Figure 1.8 from Ref. [34] shows an example of p_T^V distribution at different orders of the analytic resummation. The resummation procedure gives a finite result across the entire p_T range. A good understanding of the vector boson transverse momentum spectrum is crucial, particularly in the determination of m_W where its mis-modelling affects the modelling of the kinematics of its decay products, thus significantly affecting the precision of the measurement.

For the purpose of this thesis, the Drell Yan process, i.e. the production of a virtual photon (γ^*), Z, or W via the interaction of two partons and its subsequent decay into a pair of leptons (e.g. $q\bar{q}' \to V \to \ell\ell$) will be described in detail. As mentioned in the previous section, an incoming quark can radiate a gluon and generate a non-zero p_T^V. For example, the Feynman diagrams for the $W \to \ell\nu_\ell$ process with and without gluon emission are shown in Fig. 1.7.

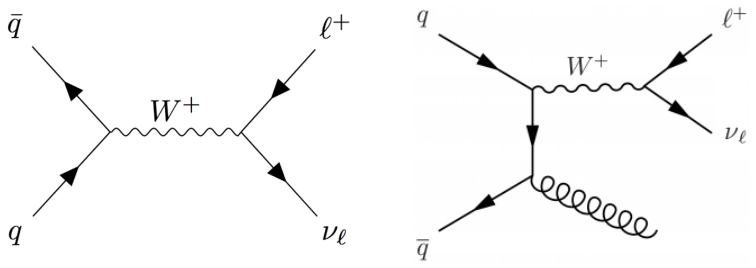

Figure 1.7: Feynman diagrams for the $W \to \ell\nu_\ell$ process, without (left) and with (right) gluon emission.

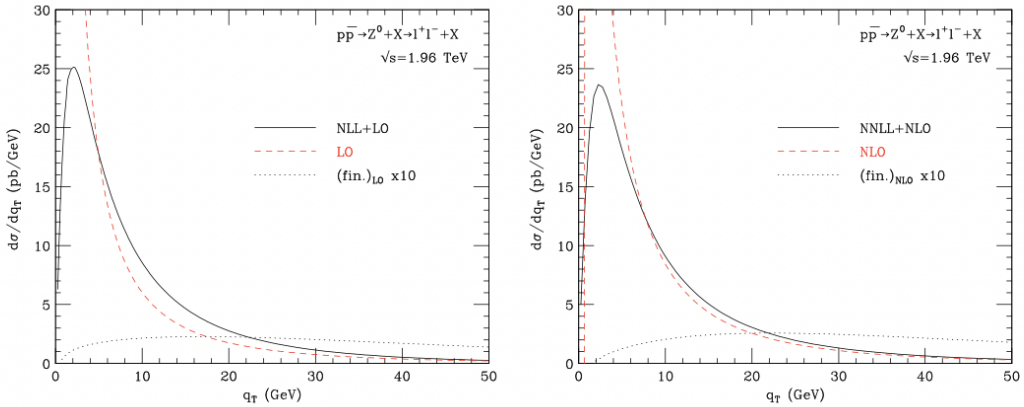

Figure 1.8: Example of vector boson transverse momentum distribution at different order in the analytic resummation, from Ref. [34]. The p_T (here denote as q_T) spectrum of Z bosons at the Tevatron Run 2: results at NLL+LO (left panel) and NNLL+NLO (right panel) accuracy. The finite component of the transverse momentum spectrum (dotted line) is also shown.

The production and decay of W and Z bosons in Drell Yan processes can be described by a five-dimensional differential equation in the vector boson and lepton kinematics (at the *Born-level*, i.e. neglecting QED final state radiation):

$$\begin{aligned}\frac{d^5\sigma}{dp_T^2 dy dM d\cos\theta d\phi} = \frac{3}{16\pi}\frac{d^3\sigma}{dp_T^2 dy dM} \\ \times\Big[(1+\cos^2\theta^*) + A_0\frac{1}{2}(1-3\cos^2\theta^*) \\ + A_1 \sin 2\theta^* \cos\phi^* + A_2\frac{1}{2}\sin^2\theta^*\cos 2\phi^* \\ + A_3 \sin\theta^*\cos\phi^* + A_4\cos\theta^* \\ + A_5 \sin^2\theta^*\sin 2\phi^* + A_6 \sin 2\theta^*\sin\phi^* + A_7\sin\theta^*\sin\phi^*\Big],\end{aligned} \tag{1.17}$$

where p_T, y, M are the transverse momentum, rapidity and mass of the vector boson,

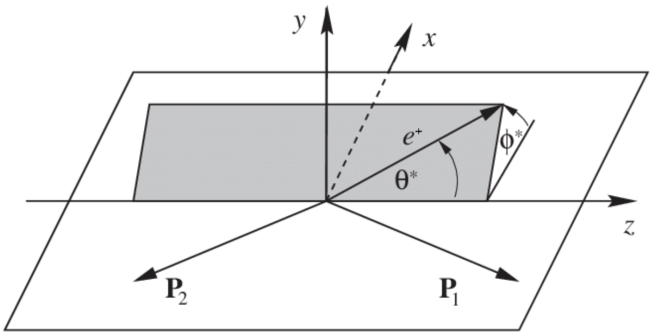

Figure 1.9: Schematic representation of the Collins Soper frame.

respectively, and θ^* and ϕ^* are the polar and azimuthal angle that the positively charged lepton forms with the axis that bisects the quarks direction (also known as Collins Soper Frame [35]). A schematic representation of the Collins Soper frame is shown in Fig. 1.9. It is important to mention that Eq. 1.17 only holds if no kinematic cuts are applied on the leptons. The cross section can be decomposed in terms of the *unpolarised* cross section (the first factor in Eq. 1.17), and a linear combination of nine functions of θ^*, ϕ^* with eight coefficients A_i which depend on the vector boson p_T, rapidity and mass, and represent the helicity cross sections divided by the unpolarised cross section. The $A_5 - A_7$ coefficients are non-zero only at order $\mathcal{O}(\alpha_s^2)$.

1.3.3 Measuring m_W at hadron colliders

At hadron collider experiments, it is not possible to fully reconstruct the W boson mass from the invariant mass of its decay products because of the missing neutrino tracks. Therefore, measurements of m_W at hadron colliders have to date been based on three different mass-sensitive final state variables in $W \to \ell\nu_\ell$ decays, where ℓ can be either an electron or a muon. These observables are the transverse momentum of the charged lepton (p_T^ℓ), the missing transverse momentum (p_T^{miss}) and the transverse mass $m_T = \sqrt{2p_T^\ell p_T^{\text{miss}}(1 - \cos\Delta\phi)}$, where $\Delta\phi$ is the opening angle between the charged and neutral lepton momenta in the plane transverse to the beams. The kinematic peaks of these distributions are the most sensitive part to m_W. The charged lepton and the neutrino are produced back-to-back in the rest frame of the W boson, therefore the transverse mass distribution is peaked at $m_T = m_W$,

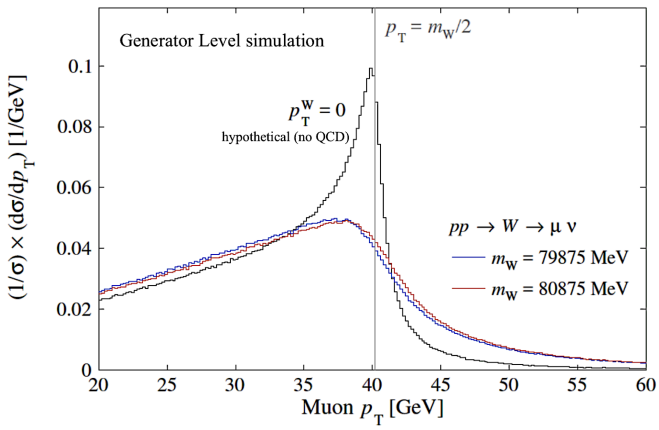

Figure 1.10: Three hypothetical examples of muon p_T distribution from $W \to \mu\nu$ decays: with $p_T^W = 0$ in black, with $p_T^W \neq 0$ but two different m_W values in red and blue.

while the p_T^ℓ and p_T^{miss} distributions peak at $m_W/2$. These peaks are smeared out by non-zero p_T^W distribution and by the detector resolution. The accurate modeling of these distributions is the key challenge of the m_W measurement.

Reaching a sufficiently accurate description is even more complicated when considering the mechanisms of W production in high energy proton-proton collisions, such as those of the LHC. Mainly first generation quarks contribute to W production, but noticeable contribution come from second generation sea quarks (20% at the LHC against 5% at Tevatron). The fraction depends on the PDFs and has a direct impact on p_T^W, and therefore on the observables used to measure m_W.

The analysis presented in this thesis extracts m_W from the p_T distribution of muons from $W \to \mu\nu$ decays. Figure 1.10 shows an example of the muon p_T distribution from a "generator-level" simulation (i.e. a simulation that does not model the reconstruction process of tracks withing the detector and the interaction of particles with the detector's material). The hypothetical distribution with $p_T^W = 0$ is shown in black, while two realistic p_T shapes whose extracted m_W values differ by 1 GeV are shown in red and blue. Despite the large difference in m_W the two distributions look very similar. This gives a hint of how crucial the good modeling of the muon p_T shape is.

In order to measure m_W a template fit of the distributions described above is performed. Predictions of the final states distributions with different m_W hypotheses

(i.e. "templates") are obtained by reweighting the simulated events according to a Breit Wigner distribution. Templates are then compared to the measured distribution and a χ^2 minimisation is performed to extract the best-fit template and the corresponding value of m_W.

2

Parton Distribution Functions and the W mass measurement

The uncertainty on the first measurement of m_W at the Large Hadron Collider (LHC) by the ATLAS experiment was dominated by the uncertainty on the Parton Distribution Functions (PDFs). The measurement of m_W with the LHCb experiment will be affected and could be potentially dominated by this source of uncertainty. Therefore, the author of this thesis performed a phenomenology study on simulated events before analysing the real data. This study aims at understanding how the PDF uncertainty arises in a measurement of m_W at LHCb, and proposes a strategy to reduce it. The results reported here have been published in Ref. [9].

2.1 Motivations

As reported in Chapter 1, the world average of direct measurements of m_W is dominated by the results at the Tevatron in proton-antiproton ($p\bar{p}$) collisions, and by the first measurement at the LHC in proton-proton (pp) collisions with the ATLAS experiment. In $p\bar{p}$ collisions W bosons are primarily produced by the annihilation of valence quarks and antiquarks. By contrast, gluons and sea quarks play a critical role in the pp collisions at the LHC. Measurements of m_W at the LHC are therefore expected to be more susceptible to theoretical uncertainties

in the modelling of W production than at the Tevatron [8, 36–39]. The ATLAS Collaboration reported a measurement of $m_W = 80370 \pm 19 \pm 14\,\text{MeV}$ where the first and second uncertainties are experimental and theoretical, respectively [5]. The dominant contribution to the theoretical uncertainty, around 9 MeV, can be attributed to the PDFs. A key challenge of future measurements by ATLAS and CMS will be to reduce the PDF uncertainty.

The current ATLAS and CMS detectors are capable of reconstructing charged leptons in the approximate "central" pseudorapidity range $|\eta| < 2.5$, where $\eta = -\ln(\tan(\theta/2))$ with θ being the angle between the particle direction and the beam axis. LHCb [40], instead, is a single-arm spectrometer with full charged particle tracking and identification capabilities over the "forward" range $2 < \eta < 5$, which is mostly orthogonal to the acceptance of ATLAS and CMS. A detailed description of the experiment will be given in Chapter 3. While LHCb is primarily designed for the study of beauty and charm hadrons, it has a strong track record in measurements of W and Z production in muonic final states (e.g. [41, 42]). As for precision electroweak tests, LHCb has already measured the effective weak mixing angle $\sin^2\theta^{\text{lept}}_{\text{eff}}$ [43], but the possibility of a measurement of m_W was not considered until recently.

Ref. [44] proposed a new measurement of m_W by LHCb based on the muon transverse momentum (p_T) distribution with $W \to \mu\nu$ decays. Figure 2.1 shows how the shape of the p_T distribution varies with the m_W hypothesis in simulated events. The maximum variation in the normalised distribution, which occurs at $p_T \sim 42\,\text{GeV}$, is around 10^{-4} per MeV of shift in m_W. Large W samples are therefore required to resolve this subtle change in the shape of the p_T distribution. During the years from 2015 and 2018 of the LHC data-taking period (denoted as "Run 2"), the LHCb experiment has collected around 10 million of $W \to \mu\nu$ events. Using the methods described in Ref. [44] it is estimated that this dataset could yield a m_W measurement with a statistical uncertainty of roughly 10 MeV. This means that the measurement should not be statistically limited, but it is important to understand how well the theoretical uncertainties, in particular those related to the PDFs,

can be controlled. Ref. [44] estimated that the PDF uncertainties in a standalone LHCb measurement would be larger than those in ATLAS and CMS. However, the uncertainty on the LHCb measurement would be partially anticorrelated with those of ATLAS and CMS. Therefore, the introduction of a LHCb measurement into a LHC m_W average has the potential to reduce the overall PDF uncertainty. Given the large size of the LHCb Run 2 dataset, and anticipated future data with LHCb Upgrade I [45] and the proposed Upgrade II [46], it is important to study in greater detail the cause of the PDF uncertainty in a measurement of m_W by LHCb, and possible strategies to reduce it.

2.2 Simulation of W production

A sample of 10^8 Monte Carlo events of the type $pp \to W \to \mu\nu + X$, at a centre-of-mass energy $\sqrt{s} = 13\,\text{TeV}$, is generated using POWHEG [47] with the CT10 [48] PDFs. These events are subsequently processed with PYTHIA [49] to simulate the QCD parton showering. No LHCb detector response is simulated for this study. Unless otherwise specified, events are analysed if they satisfy $30 < p_T < 50\,\text{GeV}$ and $2 < |\eta| < 4.5$[1]. Roughly 10% of the initial event sample falls into this kinematic region. The invariant mass of the W decay products (M) is assumed to follow a relativistic Breit-Wigner distribution:

$$\frac{d\sigma}{dM} \propto f(M) = \frac{M^2}{(M^2 - m_W^2)^2 + M^4\Gamma_W^2/m_W^2}, \tag{2.1}$$

where m_W and Γ_W are the mass and the width of the W boson, respectively. The events are generated with a nominal value of m_W [6] but can be reweighted according to Eq. 2.1 to emulate a different m_W hypothesis. A similar set of weights can be assigned to emulate the effect of different PDFs. In the measurement of m_W with LHCb data described in this thesis, the full PDF uncertainty considers an envelope of PDF sets from several groups, including for example the MMHT14 [50] and CT14 [51] sets, but for the current study the NNPDF3.1 [28] set with 1000

[1]The $2 < |\eta| < 4.5$ selection is chosen to make better use of the available samples: the events falling in the negative η region are equivalently treated as those with positive η.

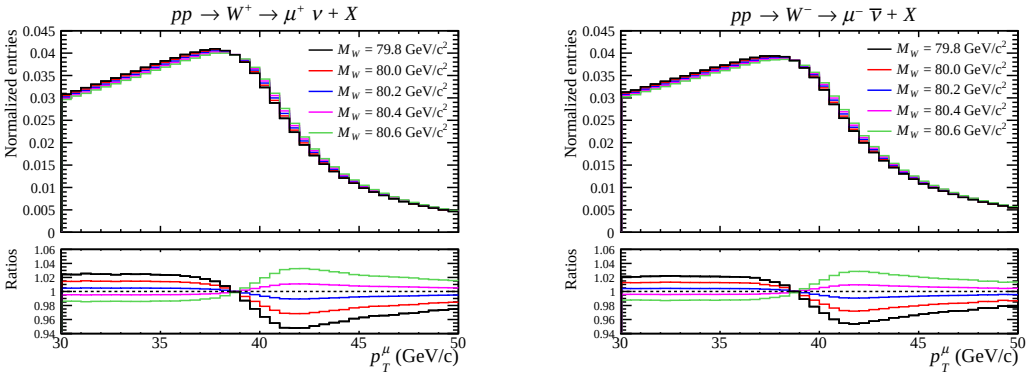

Figure 2.1: The simulated muon p_T distributions in $W \to \mu\nu$ decays (left W^+, right W^-) with five different m_W hypotheses. The ratios are with respect to the prediction with $m_W = 80.3\,\text{GeV}$.

equiprobable *replicas* is used. PDF replicas, provided by theory groups, can be obtained in different ways. Those provided by the NNPDF group are generated by performing PDF fits to Monte Carlo replicas of the experimental data. Other groups, instead, provide variations of the PDF parameters in an eigenvector basis.

2.3 Fitting method

The generated event samples are scaled to the $6\,\text{fb}^{-1}$ of LHCb Run 2 data, and yield an expectation of 7.2 (4.8) million W^+ (W^-) events in the $30 < p_T < 50\,\text{GeV}$ and $2 < \eta < 4.5$ region. A 20% charge asymmetry in $W \to \ell\nu$ decays is expected for events in this fiducial region, as reported in Ref. [52]. Toy data histograms are generated by randomly fluctuating the bins around the nominal p_T distribution, assuming these yields and Poisson statistics. These histograms can be generated with different PDF sets using the reweighting procedure already described. The current study neglects experimental systematic uncertainties, such as those due to the knowledge of the momentum scale and the dependence of the muon identification efficiency on p_T and η. These aspects are addressed in the measurement of m_W with real data, and will be described from Chapter 5 onwards.

The toy data histograms are compared to templates with different PDF and m_W hypotheses. The normalisation of each template is scaled to match the toy data such that the fit only considers the shape information. For a given PDF hypothesis

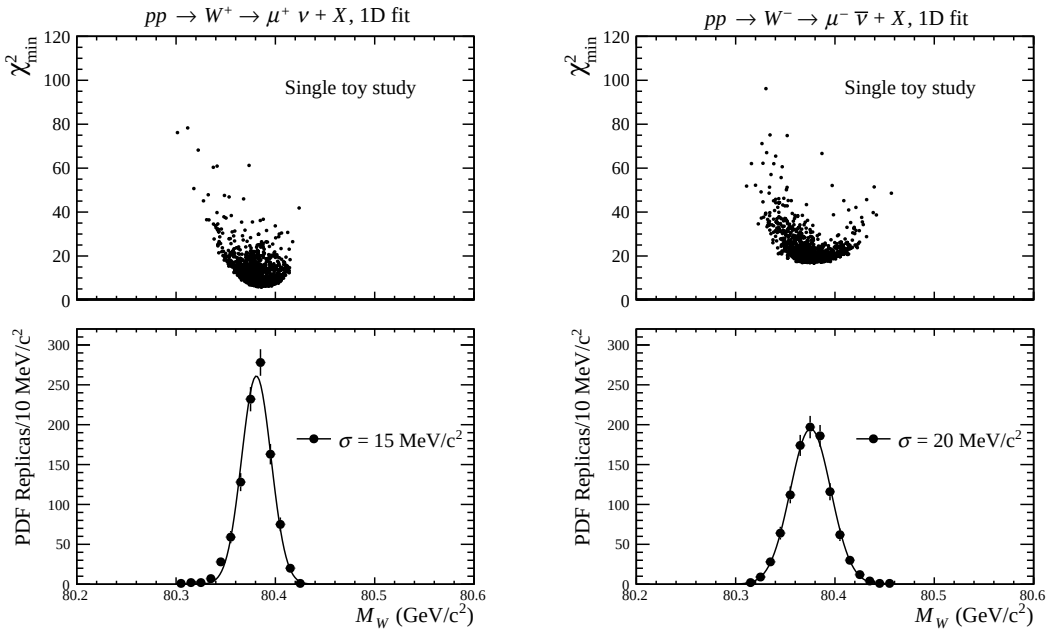

Figure 2.2: Upper: the distribution of the χ^2 versus m_W for a fit to a single toy dataset, which assumes the LHCb Run 2 statistics, with each of the 1000 NNPDF3.1 replicas. Lower: the distribution of the m_W values with a Gaussian fit function overlaid.

a single-parameter (1D) fit determines the value of m_W that minimises the χ^2 between a toy and the templates. The 68% C.L. statistical uncertainty corresponds to a variation of $\Delta\chi^2 = 1$ with respect to the parabola minimum.

Fig. 2.2 shows, separately for the two W charges, how the results of a fit to a single toy dataset vary with the PDF replica used in the templates. Forty bins in p_T (with bin width of 0.5 GeV) are used in the template fit. The fitted m_W values follow approximately Gaussian distributions with widths of 15 (20) MeV for the W^+ (W^-). The broadly parabolic distributions of the best-fit χ^2 (χ^2_{min}) versus m_W indicate that the PDF replicas that most severely bias m_W tend to give a measurably poorer fit quality. Before evaluating how this information could be used to constrain the PDF uncertainty, it is important to first try to understand in more detail the underlying mechanism behind the PDF uncertainty.

2.4 Understanding the PDF uncertainties

Figure 2.3 shows how the different partonic subprocesses (e.g. $q\bar{q}' \to W$) contribute to the cross-section for W production as a function of rapidity (y). The dominant $W^+(W^-)$ production subprocesses involve valence $u(d)$ quarks. Annihilation of gluons with sea quarks (gq_s) contributes with around 20%. Contributions from only second generation quarks annihilation are below 10%.

Since the u, $\bar{d}$, d and $\bar{u}$ species seem to be the most important, it is interesting to see if there are any obvious patterns in their respective PDFs for the replicas corresponding to biased m_W determinations. The final results are derived using the full set of 1000 NNPDF3.1 equiprobable replicas but, for visual purposes, the studies in this section make use of a subset of them. Fig. 2.4 shows how the Bjorken-x dependencies of the u, $\bar{d}$, d and $\bar{u}$ PDFs vary between the subset of replicas. Each line is a ratio with respect to the central replica, and is assigned a colour according to the bias in m_W as evaluated using the method described in Section 2.3. For clarity, the replicas for which the shift in m_W is close to zero ($|\Delta M| < 10$ MeV) are not drawn. In the study of the single partonic species, only the relevant W charge templates are included in the fit that extracts m_W. No obvious patterns can be seen in the u and $\bar{d}$ PDFs, which dominate W^+ production. However, a clear pattern can be seen for the high-x (above $x \sim 0.1$) d PDF, whereby the replicas that tend to bias m_W upwards (downwards) tend to have a smaller (larger) parton density. A qualitatively similar pattern, though with the opposite sign, is seen in the $\bar{u}$ PDF.

The PDF uncertainty on the m_W measurement arises because the p_T distribution depends on the W production kinematics, which are regulated by the W transverse momentum (p_T^W), rapidity and polarisation. As a proxy for the W polarisation, the distribution of the angle θ^* in the Collins-Soper frame [35] can be considered. Because of the vector-axial coupling of the W boson to fermions in the Standard Model, in the W production in the process $q\bar{q}' \to W$ the *spin* of the W is aligned with that of the quark (i.e. it is left-handed). As for the W *direction*, it follows that of the highest x parton (i.e. the particle that carries the largest fraction of the proton momentum) which, according to the PDFs, tends to be the quark rather

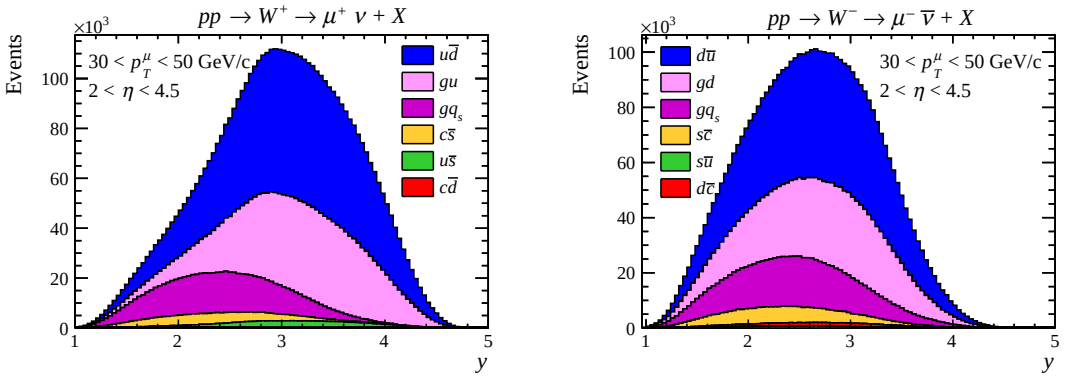

Figure 2.3: The (left) W^+ and (right) W^- rapidity distributions decomposed into the main partonic subprocesses.

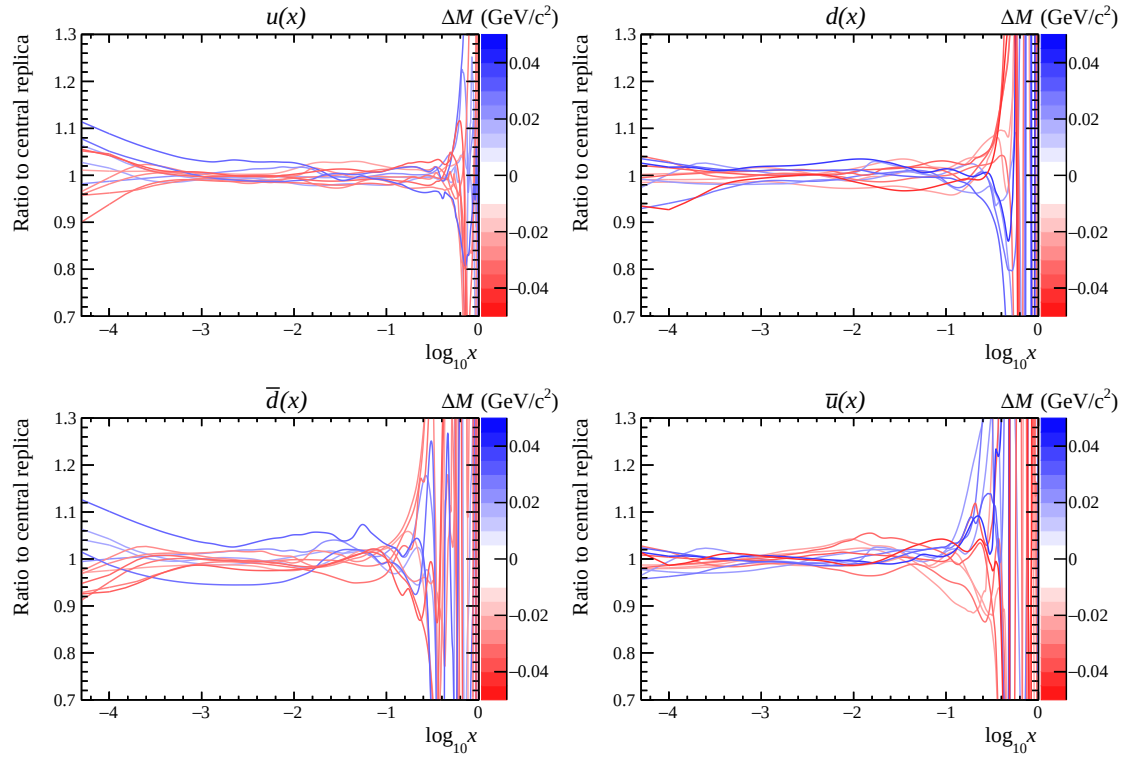

Figure 2.4: The ratios of a subset of NNPDF3.1 replicas with respect to the central replica, for the x dependence of the (clockwise from upper left) u, d, $\bar{u}$ and $\bar{d}$ PDFs. Each line is marked with a colour indicating the shift of the m_W value determined from a fit to the p_T distribution of a single toy dataset. For clarity, the replicas for which the shift in m_W is close to zero are not drawn.

than the antiquark. This effect is particularly enhanced at high rapidities, where the W spin is thus aligned opposite to the direction of the momenta of both the W boson and the quark. Therefore, a measurement of the $\cos\theta^*$ angle provides information on the direction of the W boson and, consequently, on its helicity or polarisation. Figure 2.5 shows how the p_T^W, y and $\cos\theta^*$ distributions vary between a subset of NNPDF3.1 replicas. Each line is assigned a colour according to the bias in m_W for that replica. The underlying shapes of the distributions are also indicated by the filled histograms. A particularly striking pattern can be seen in the variation of the rapidity distributions. The replicas that bias m_W upwards (downwards) tend to enhance (suppress) the W^+ cross-section at large rapidities. The opposite is seen for the W^-. Other clear patterns, though with smaller absolute variations, can be seen in the p_T^W and $\cos\theta^*$ projections. It is instructive to consider the two-dimensional projections of these patterns. Figure 2.6 shows the mean of the y distribution versus the mean of the p_T^W distribution. Each point represents a single NNPDF3.1 replica using the already described m_W dependent colour scale. There is a clear anticorrelation between the changes in the shapes of the y and p_T^W distributions which is expected from the kinematics and is enhanced by the forward acceptance cuts applied to the lepton, but further patterns can be seen in the colour distribution. In the W^+ case, the replicas that bias m_W upwards (downwards) tend to predict larger (smaller) $\langle y \rangle$ values and smaller (larger) $\langle p_T^W \rangle$ values. The opposite pattern is seen for the W^- case. These striking patterns are helpful in understanding how biases in m_W are correlated to the underlying W production kinematics.

Special focus is given to the muon kinematic distributions. Ref. [53] showed that correlated changes in the shapes of the η and p_T distributions in the phase-space acceptance of ATLAS and CMS can be used to further constrain the PDFs. This approach has been extensively used by CMS in the measurement of the W boson rapidity and helicity [54]. It is therefore interesting to consider a similar approach in the LHCb phase-space acceptance. Figure 2.7 shows how the muon p_T and η distributions vary with the PDF replicas. The replicas that bias m_W upwards (downwards) correspond to a decrease (increase) in the predicted cross-section at

high p_T with respect to low p_T. An intriguing observation, however, is that the replicas that provide the largest bias on m_W change not only the shape of the p_T distribution but also that of the η distribution. This is a *measurable* change of up to several percent, which could be exploited to constrain the PDF uncertainty. Figure 2.8 shows the mean p_T versus the mean η for each replica, with the m_W dependent colour scale as before. The replicas that bias m_W tend to be clearly separated in this two-dimensional plane, which encourages to consider exploiting this information to constrain the PDF uncertainty.

2.5 PDF uncertainty reduction

In Section 2.3 it was noted that the traditional one-dimensional fit to the p_T distribution already suggests a potential for *in situ* constraints of the PDF uncertainty. In particular, it was observed that replicas that tend to severely bias m_W also lead to poorer fit quality. It is therefore interesting to evaluate the possibility of favouring the replicas that give better fit results over the others. In order to do this, the fit is now compared with and without the inclusion of replica weights. Using the NNPDF prescription [55, 56], each replica is assigned a weight according to the best-fit χ^2 (χ^2_{min}) for a fit with n degrees of freedom (n):

$$P(\chi^2_{\text{min}}) \propto \chi^{2\,(n-1)}_{\text{min}} e^{-\frac{1}{2}\chi^2_{\text{min}}}. \tag{2.2}$$

This has the effect of disregarding replicas that are incompatible with the data. An alternative approach is to use the PDFs represented by Hessian eigenvectors and profile them in the analysis [57]. Section 2.4 encourages the consideration of a fit to the two-dimensional (p_T versus η) distribution to further constrain the PDF uncertainty. The two-dimensional fit uses three bins in η within the ($2 < \eta < 4.5$) range and forty bins in p_T within the ($30 < p_T < 50\,\text{GeV}$) range already described. Figure 2.9 shows, separately for the W^+ and W^- cases, the distribution of m_W and χ^2 values for the two-dimensional fit to a single toy dataset. The distributions of m_W values are shown with and without the replica weights. In the W^+ case the width of the weighted distribution is roughly a factor of three smaller than

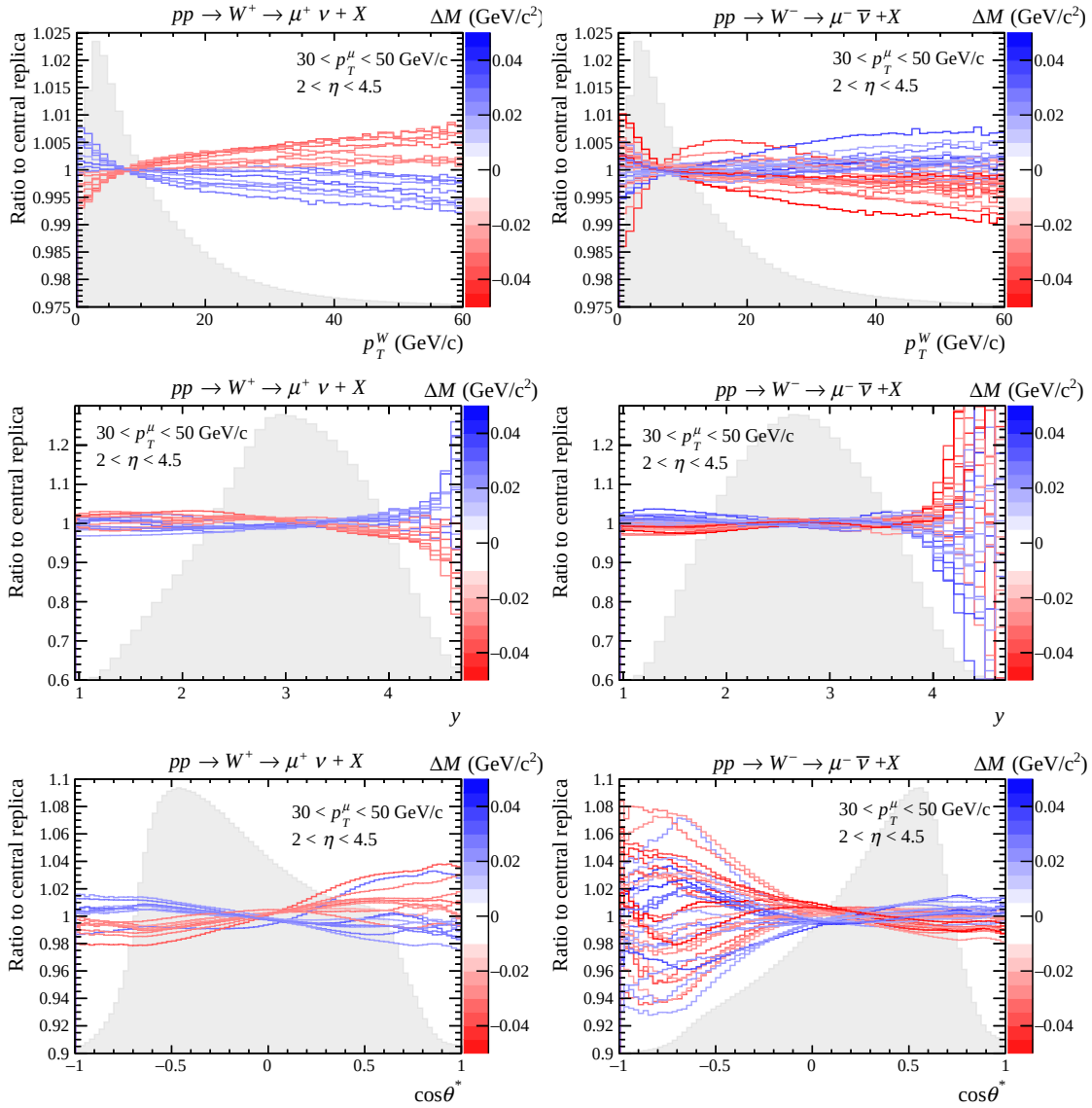

Figure 2.5: The variations in the shapes of the p_T^W, y and $\cos\theta^*$ distributions predicted with a subset of NNPDF3.1 replicas. Each line is marked with a colour indicating the shift of the m_W value determined from a fit to the p_T distribution of a single toy dataset. For clarity, the replicas for which the shift in m_W is close to zero are not drawn.

the unweighted distribution. For the W^- the width is reduced by roughly 50%. The effective number of replicas after reweighting

$$N_{\text{eff}} = \frac{(\Sigma_{i=1}^{N} w_i)^2}{\Sigma_{i=1}^{N} w_i^2} \quad \text{with} \quad w_i = P(\chi^2_{i,\text{min}}), \tag{2.3}$$

where N is the total number of replicas, gives an indication of the statistical reliability of the method. It is estimated that $N_{\text{eff}} = 113$ (105) for the W^+ (W^-) sample. The high constraining power of the proposed method is manifest in the

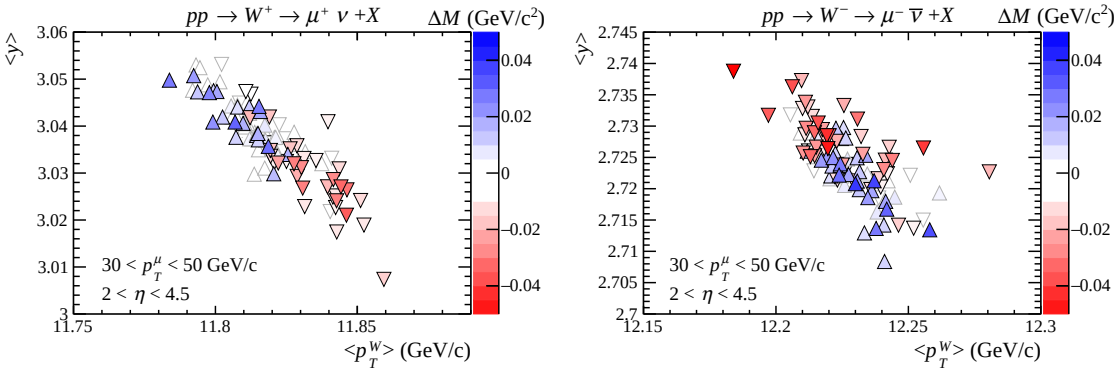

Figure 2.6: The distributions of $\langle p_T^W \rangle$ and $\langle y \rangle$ for a subset of replicas of the NNPDF3.1 set. Each marker is assigned a colour according to the shift of the m_W value determined from a fit to the p_T distribution of a single toy dataset. The markers drawn with an up (down) pointing triangle correspond to ΔM values greater (less) than zero.

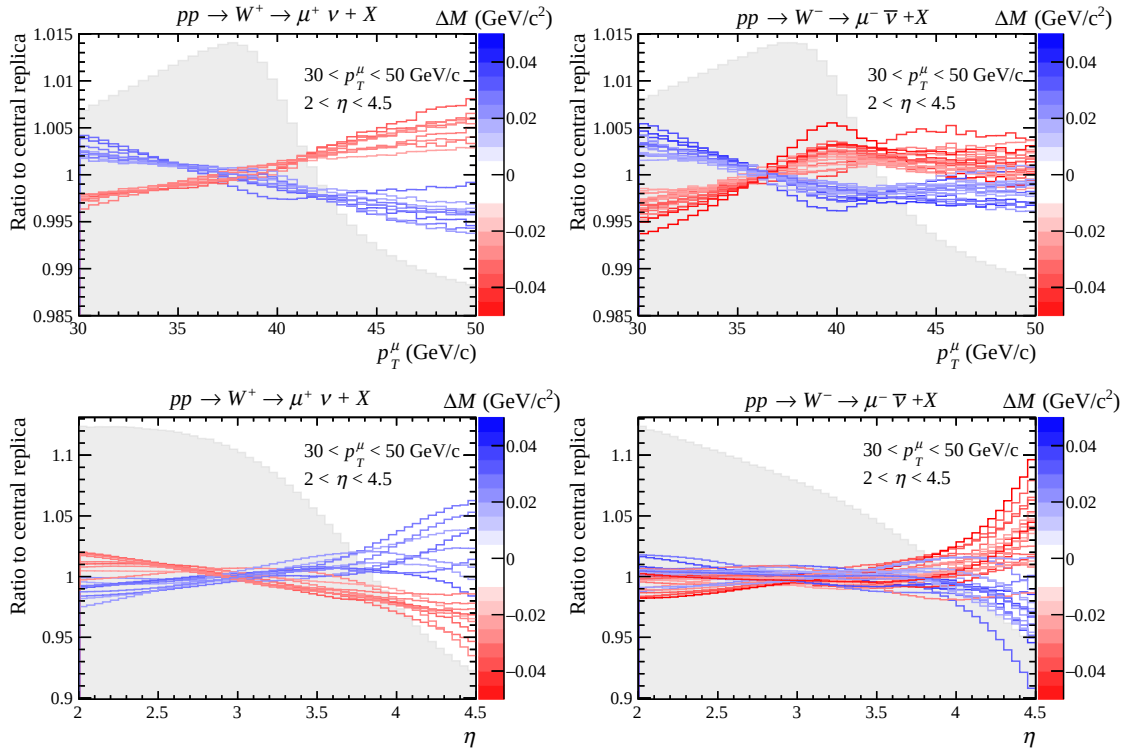

Figure 2.7: The variations in the shapes of the p_T and η distributions predicted with a subset of NNPDF3.1 replicas. Each line is marked with a colour indicating the shift of the m_W value determined from a fit to the p_T distribution of a single toy dataset. For clarity, the replicas for which the shift in m_W is close to zero are not drawn.

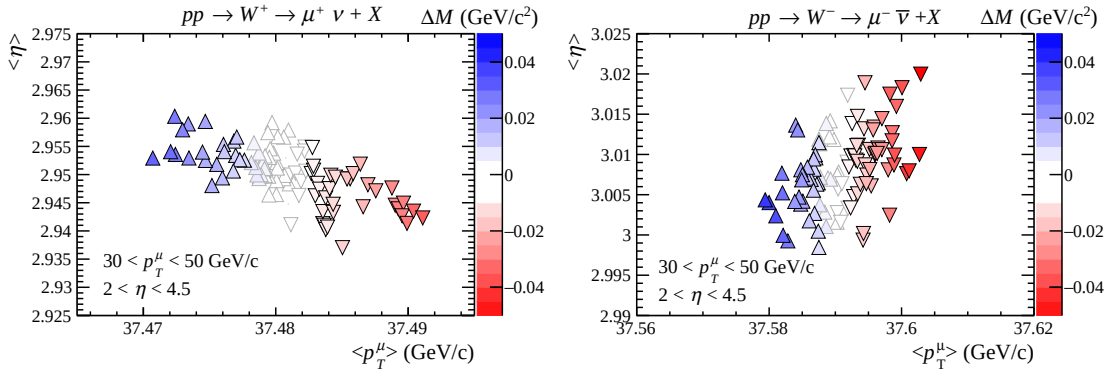

Figure 2.8: The distribution of $\langle p_T \rangle$ and $\langle \eta \rangle$ produced using a subset of replicas of the NNPDF3.1 set and divided by the central replica. Each marker is assigned a colour according to the shift of the m_W value determined from a fit to the p_T distribution of a single toy dataset. The markers drawn with an up (down) pointing triangle correspond to ΔM values greater (less) than zero.

large reduction of the effective number of replicas.

The weights are clearly dependent on the toy data, so it is now important to consider the results with multiple toy datasets. For a single toy dataset the PDF uncertainty is defined by the RMS of the m_W values for the 1000 replicas. Figure 2.10 shows the distribution of the PDF uncertainty for 1000 toy datasets, comparing the one-dimensional fit with and without weights, and the two-dimensional fit with weights. In the one-dimensional case the weighting reduces the uncertainty by an average factor of 10 (20)% for the W^+ (W^-), with a larger spread of the distributions under data fluctuations. In the one-dimensional weighted case this is estimated to be about 0.8 (1.2) MeV for the W^+ (W^-), in contrast to the 0.04 (0.07) MeV of the unweighted case. The two-dimensional weighted case corresponds to a most probable improvement by a factor of roughly two (1.5) for the W^+ (W^-), with a spread under data fluctuations of 0.9 (1.2) MeV. Since the outcome of the PDF replica weighting depends on the data, the computation of the PDF uncertainty becomes much more sensitive to the statistical fluctuations of the data itself. This explains the broadening of the PDF uncertainty distributions once the weighting is applied. This effect becomes even larger for the two-dimensional fit because of its higher constraining power. However, even considering the broadening effect, there is a clear separation between the two-dimensional weighted PDF uncertainty distribution and

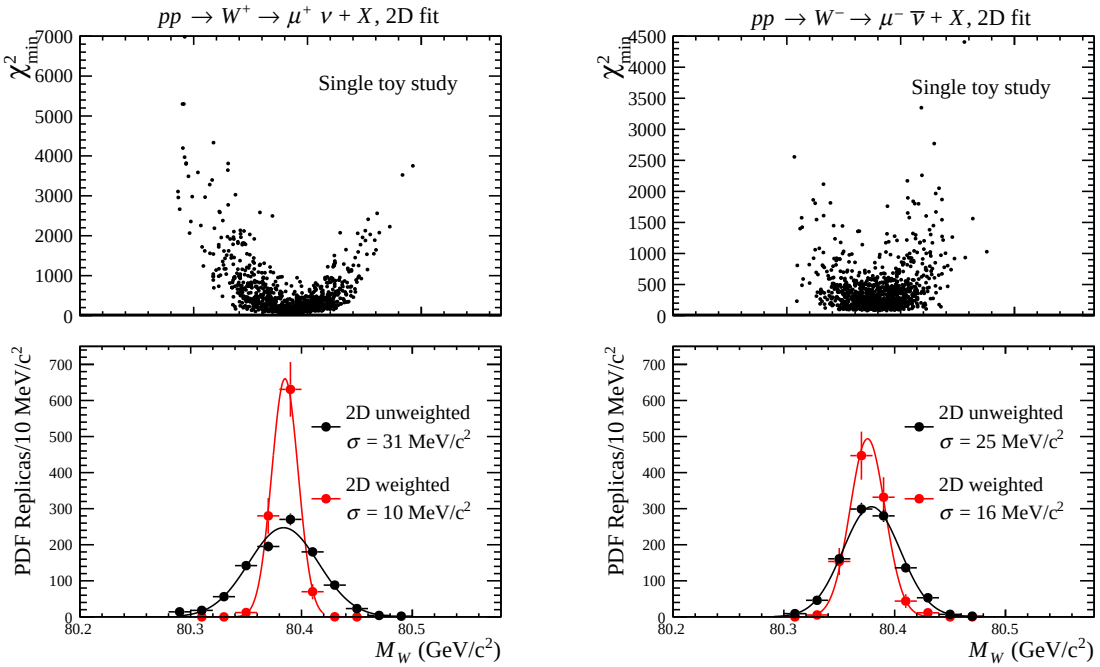

Figure 2.9: Upper: the distribution of the χ^2 versus m_W for a two-dimensional fit to a single toy dataset, which assumes the LHCb Run 2 statistics, with each of the 1000 NNPDF3.1 replicas. Lower: the distribution of the extracted m_W values, with a Gaussian fit function overlaid, without (black) and with (red) weighting.

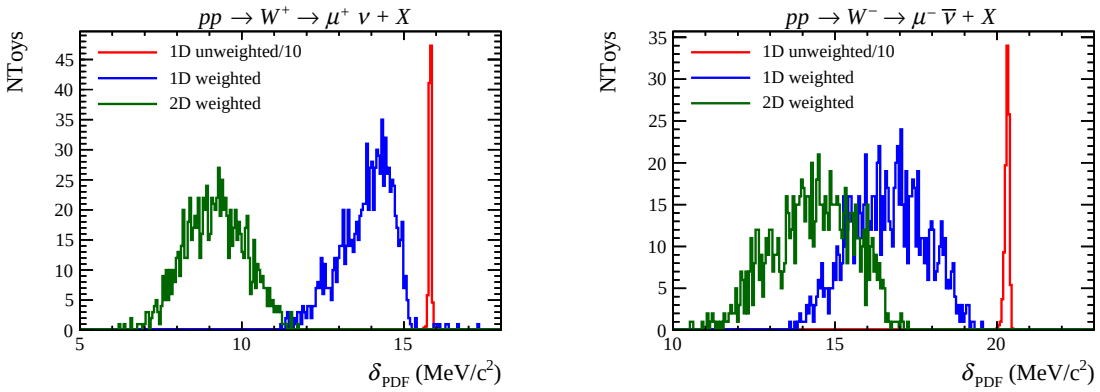

Figure 2.10: The distribution of the PDF uncertainty evaluated for 1000 toy datasets using three different methods: p_T fit without weighting, p_T fit with weighting, (p_T, η) fit with weighting. The one-dimensional unweighted distribution is arbitrarily scaled down by a factor of ten.

that of the one-dimensional unweighted (reference) fit approach. These encouraging results strongly motivate the adoption of the two-dimensional fit method by LHCb.

2.5.1 Simultaneous fit of W^+ and W^- samples

Following the promising results shown for separate fits to the W^+ and W^- data it is now interesting to consider the combination of the two charges. Figure 2.11 shows, separately for the one-dimensional and two-dimensional approaches, the W^+ versus W^- fit results for a single toy dataset. Each point represents a different PDF replica. Interestingly, for both fit approaches, there is a partial anti-correlation, which implies a partial cancellation of the PDF uncertainty when the W^+ and W^- data are combined. It is now interesting to see how this partial anti-correlation is affected by the introduction of the weights and the transition to a two-dimensional fit. Therefore, in Figure 2.11 ten percent of the points corresponding to the largest product (over the two W charges) of $P(\chi^2_{\text{min}})$ values are highlighted. Unfortunately, in both the one- and two-dimensional fit cases, the correlation coefficient for the subset of favoured replicas is much lower. Figure 2.12 shows the χ^2_{min} versus m_W values for combined (W^+ and W^-) fits to a single toy dataset. Each point corresponds to a different NNPDF3.1 replica, and the results are shown separately for the one-dimensional and two-dimensional fits. The distributions of m_W values with and without weights are shown with corresponding Gaussian fits overlaid. With these data the weights have very little effect on the width of the distribution in the one-dimensional case. The effective number of replicas (N_{eff}) after reweighting, computed using Eq. 2.5, is indeed 928. In the two-dimensional case, however, there is roughly a factor of two of improvement. The effective number of replicas estimated for this case ($N_{\text{eff}} = 35$) is showing a very large constraining power of the data and suggests that, for the final measurement, a more robust approach like the Hessian method or an increase of the number of replicas in the reweigting procedure, is necessary to guarantee the statistical reliability of the results obtained with the two-dimensional fit.

Figure 2.13 shows the distribution of the PDF uncertainty in 1000 toy datasets, in combined fits of the W^+ and W^- data. Compared to the traditional one-dimensional fit, the addition of the weighting typically improves the PDF uncertainty by around 10%. The two-dimensional fit with weighting is, however, typically around a factor

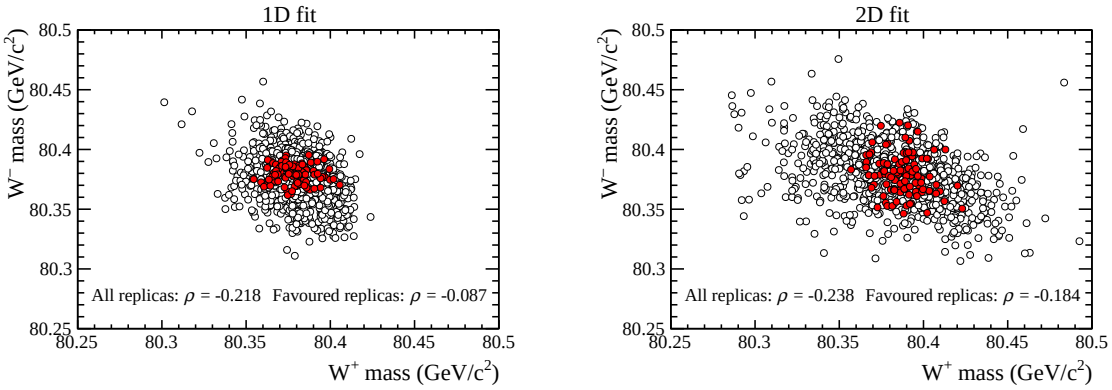

Figure 2.11: The distribution of the W^- versus W^+ mass determined from a single toy dataset with each of the NNPDF3.1 replicas. Ten percent of the replicas with the highest $P(\chi^2)$ (product over the two W charges) are assigned red markers.

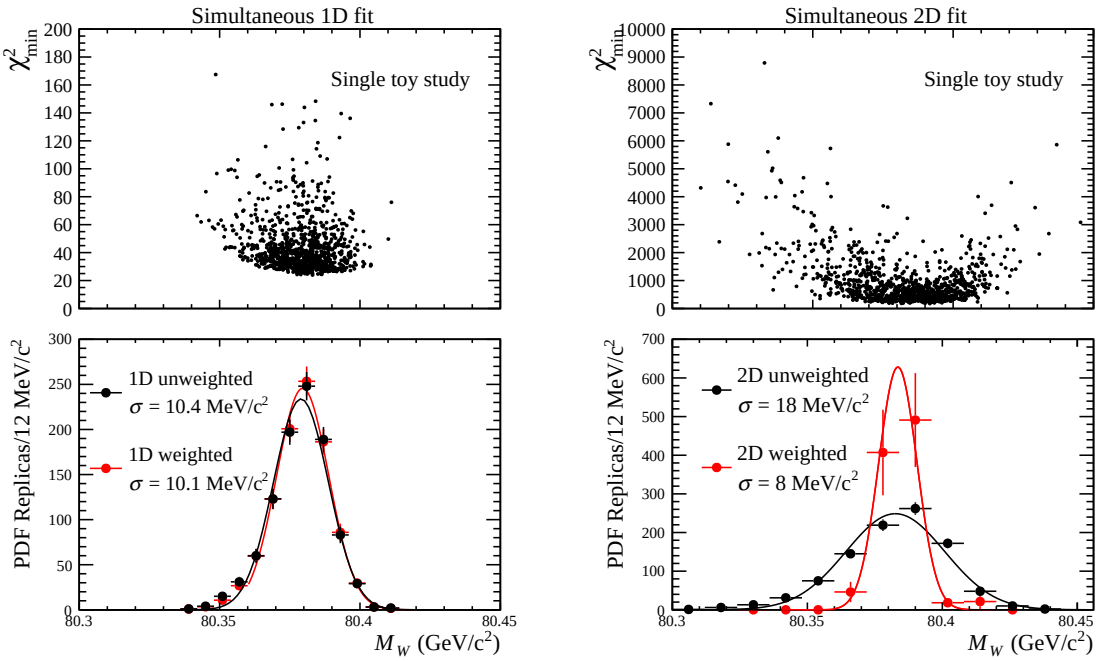

Figure 2.12: Upper: the distribution of χ^2 versus m_W for a one-dimensional (left) and two-dimensional (right) simultaneous fit of W^+ and W^- data to a single toy dataset, which assumes the LHCb Run 2 statistics, with each of the 1000 NNPDF3.1 replicas. Lower: the extracted m_W values, with a Gaussian fit function overlaid, without (black) and with (red) weighting.

of two better. Ref [9] also considers an alternative approach where the W^+ and W^- data are analysed separately, and the corresponding m_W values are combined in a weighted average. This results in larger uncertainties, and therefore encourages the simultaneous fit of W^+ and W^- data with a single shared m_W fit parameter.

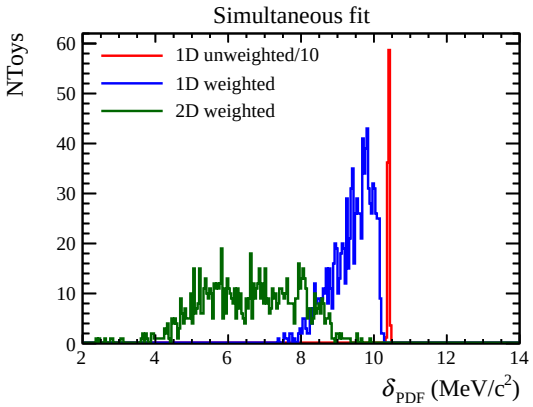

Figure 2.13: The distribution of the PDF uncertainty evaluated for 1000 toy datasets from a simultaneous fit to W^+ and W^- data. Three different fit methods are compared: p_T fit without weighting, p_T fit with weighting, (p_T, η) fit with weighting. The one-dimensional unweighted distribution is arbitrarily scaled down by a factor of ten.

2.5.2 Dependence on the detector acceptance

The study has thus far been restricted to events in the range $30 < p_T < 50$ GeV and $2 < \eta < 4.5$. It is interesting to now consider how the results depend on this choice, since the LHCb acceptance extends slightly outside this η range, and LHCb is able to reconstruct muons with far smaller p_T values. Figure 2.14 shows how the PDF uncertainties depend on the width of the p_T interval, which is symmetric around $m_W/2$. Each band is centered on the mean of the distribution of the PDF uncertainty evaluated for 1000 toy datasets and its width is defined as the RMS of the same distribution. With the simple one-dimensional unweighted fit the PDF uncertainty grows approximately linearly with the width of the p_T interval. This is also the case for the one- and two-dimensional weighted fits, though the slope is less severe. Despite this study suggests that choosing a smaller fit range yields smaller PDF uncertainties, the reduction of this range has an impact on the statistical precision of the measurement as well. Figure 2.15 considers separately the dependence on the minimum and maximum η value. The uncertainty is found to reduce when the η range is extended in either direction. It was also verified that the uncertainty does not change significantly if the number of η bins is increased from the nominal value of three. Using only three bins should make the modelling

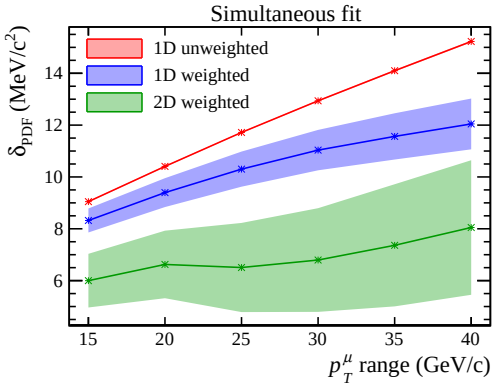

Figure 2.14: PDF uncertainty as a function of the p_T range (the full width, centered around $m_W/2$) used in the simultaneous fit. The bands report the mean and the RMS of the distribution of the PDF uncertainty evaluated for 1000 toy datasets. The η range is set to $2 < \eta < 4.5$. In the two dimensional fits three η bins are used.

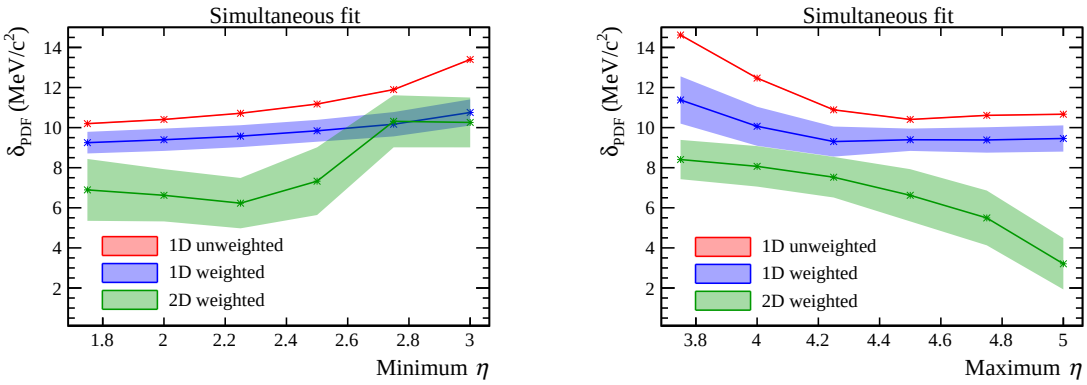

Figure 2.15: PDF uncertainty as a function of the lower (left) and upper (right) η cut used in the simultaneous fit. The bands report the mean and the RMS of the distribution of the PDF uncertainty evaluated for 1000 toy datasets. The p_T is in the range $30 < p_T < 50$ GeV. Left (Right): the upper (lower) η cut set to 4.5 (2). In the two dimensional fits three η bins are used.

of the η distribution, in particular the experimental control of the η dependence of the muon efficiency, easier to control than if more bins are required.

2.6 Summary

A series of preliminary studies suggested that LHCb should perform a measurement of m_W based on a one-dimensional fit to the muon p_T distribution in samples of $W \to \mu\nu$ decays. Thanks to LHCb's unique angular coverage this measurement would complement those performed by ATLAS and CMS, particularly when considering

PDF uncertainties. This chapter reports a detailed study of the PDF uncertainty on the proposed LHCb measurement. It is found that the variations in the PDFs that tend to bias the determination of m_W lead to clear patterns of variation in the shapes of the W kinematic distributions, in particular the rapidity distribution. A particularly interesting observation is that those variations also lead to a measurable change in the shape of the muon η distribution. An analysis performed on a two-dimensional (p_T versus η) plane would reduce the capability of the PDFs to give rise to changes in the p_T distribution that can be misidentified as variations of m_W. Therefore, with large enough data samples, a two-dimensional fit to the p_T versus η distribution, with the application of a PDF replica weighting strategy, would allow the PDF uncertainty to be further constrained. A study with 1000 experiments, assuming the LHCb Run 2 statistics, indicates a typical improvement of around a factor of two, compared to the one-dimensional fit to the p_T spectrum alone, when fitting the W^+ and W^- data simultaneously. The full PDF uncertainty should also include the variation between results from different PDF fitting groups, but this is a very encouraging result. The main study considers events in which the muon satisfies $2 < \eta < 4.5$ and $30 < p_T < 50\,\text{GeV}$, but the dependence on these choices is also studied since there are likely to be many considerations on the optimal fit range for the real measurement.

Although the fit methodology proposed in this study yields to a smaller PDF uncertainty in the measurement of m_W, the analysis performed on LHCb data which will be described in the following chapters does not make use of it for two reasons. First, the PDF uncertainty is found not to be the dominant source of uncertainty in the measurement. One possible reason is that the measurement of m_W that will be described makes use of more recent PDF sets than those that were used for previous measurements. Furthermore, the adopted m_W fit has more freedom in the vector boson p_T modelling (as described in Ref. [58]) than alternative methods used in other measurements of m_W. Additionally, the accurate modelling of a two-dimensional distribution requires a higher level of understanding and control of

the physics and the detector effects than a one-dimensional fit. It is nevertheless important to reconsider the results of this study for future measurements of m_W.

3

The LHCb experiment at the LHC

3.1 The Large Hadron Collider

The European Council for Nuclear Research (CERN) facilities located near Geneva host the largest particle accelarator ever built to date. The Large Hadron Collider (LHC) occupies a 27 km circular tunnel located at a 100 m depth underground across the French and Swiss border. Its proton accelerating system exploits some of the facilities that were already present on site and were used by previous experiments. Figure 3.1 shows the accelerator complex that is used as injection system for the LHC. Protons are extracted from nuclei of hydrogen atoms and are accelerated up to 50 MeV by the LINAC2 linear accelerator. Then, protons reach the first ring (Booster) where they are accelerated up to 1.4 GeV. Their energy increases to 26 and 450 GeV after the injection in the Proton Synchrotron (PS) and the Super Proton Synchrotron (SPS) respectively. Finally, bunches of protons are injected in the LHC, where they travel in opposite directions into separate beam pipes kept at ultra-high vacuum. Proton collisions happen in specific points of the LHC ring, corresponding to the position of the detector. The four biggest ones are ATLAS (A Toroidal LHC ApparatuS), CMS (Compact Muon Solenoid), LHCb (Large Hadron Collider beauty) and ALICE (A Large Ion Collider Experiment).

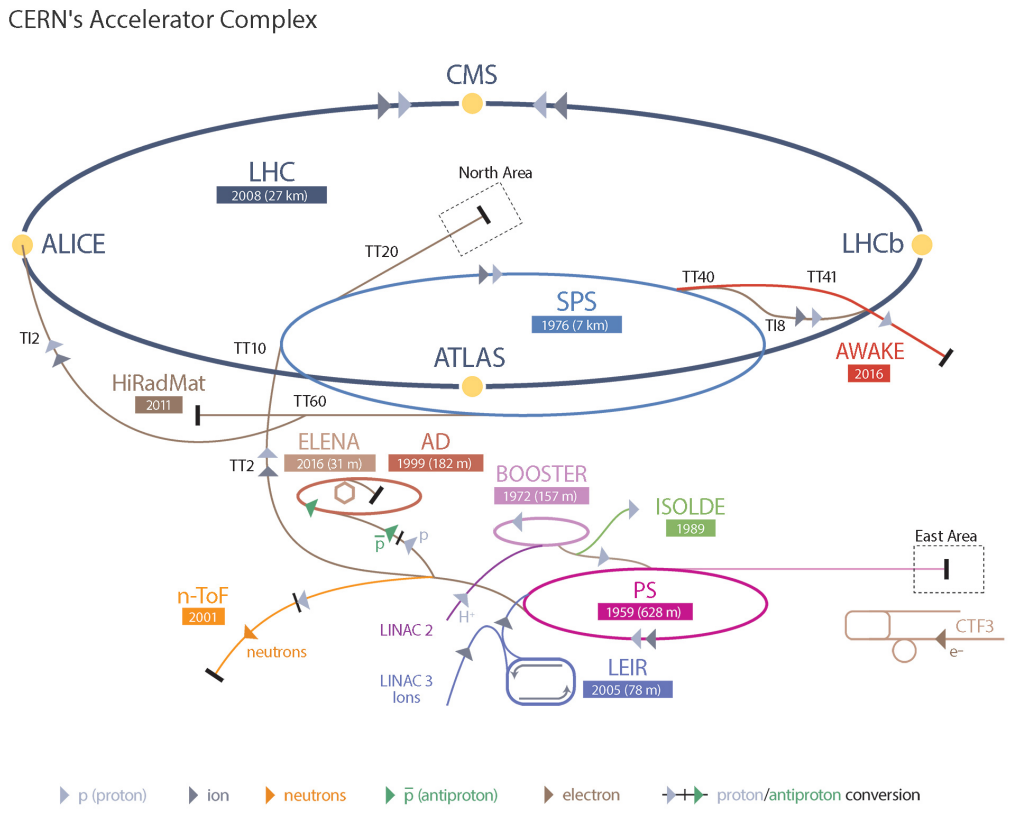

Figure 3.1: CERN accelerator complex used as injection for the LHC.

Proton-proton (pp) collisions started in 2009 at a centre-of-mass energy $\sqrt{s} = 7\,\text{TeV}$, increased to 8 TeV in 2012. The first phase of data taking (denoted as "Run 1") was followed by a 3-years long shutdown. The next phase of data taking ("Run 2") started in 2015 at $\sqrt{s} = 13\,\text{TeV}$ and lasted until the end of 2018. During Run 2, the intensity of collisions reached the nominal instantaneous luminosity (defined as the number of events collected per unit of time with a given interaction cross section) value of $10^{34}\,\text{cm}^{-2}\text{s}^{-1}$ with a bunch crossing rate of up to 40 MHz, corresponding to an interval of 25 ns between two consecutive collisions. The unprecedented capabilities of the LHC of accelerating particles up to the TeV energy scale are the result of a huge progress in the accelerator physics field. A system of dipole superconducting magnets provides the necessary 8 T magnetic field to maintain particles into circular trajectory, while quadrupole and octupole magnets focus the particle bunches to minimise beam losses. Superconducting

magnets operate at 1.9 K temperature, which is achieved thanks to an efficient cooling system based on superfluid helium.

3.2 The LHCb detector

The LHCb detector is a single-arm forward spectrometer covering the pseudorapidity range $2 < \eta < 5$, primarily designed for the study of particles containing beauty or charm quarks. The LHCb geometry is defined according to a right-handed Cartesian system with the origin at the interaction point. The x-axis is oriented horizontally towards the outside of the LHC ring, the y-axis points upwards with respect to the beamline and the z-axis is aligned with the beam direction. A scheme of the layout of the experiment in the $[y, z]$ plane is shown in Fig. 3.2. This layout remained unchanged during the Run 1 and Run 2 of data taking. It is possible to identify three main areas: the track reconstruction system (consisting of the Vertex Locator, the upstream Trigger Tracker and downstream tracking stations with respect to a dipole magnet), the particle identification system (with Ring Imaging Cherenkov detectors, the calorimeters and the muon system) and the trigger. An overview of each sub-detector is given in the following paragraphs.

3.2.1 The Vertex Locator

The VErtex LOcator (VELO) is the closest sub-detector to the collision point. It provides precision measurements of the positions of primary (PV) and secondary interaction vertices. The VELO consists of 42 semi-circular silicon strip detectors placed on the $[x, y]$ plane as shown in Fig. 3.3. Each module provides a measurement of the radial (r) and polar (ϕ) coordinate of a track hit. The two halves of each module are allowed to move far from or close to the beam line depending on the stability of the beam. During the data-taking, the modules are located at a 8 mm distance from the beam. This makes the VELO the closest sub-detector to the beam at the LHC. The support of the modules is retractable so that the separation between the halves can be increased during the LHC beams injection. This feature makes the alignment of the VELO modules very important to ensure

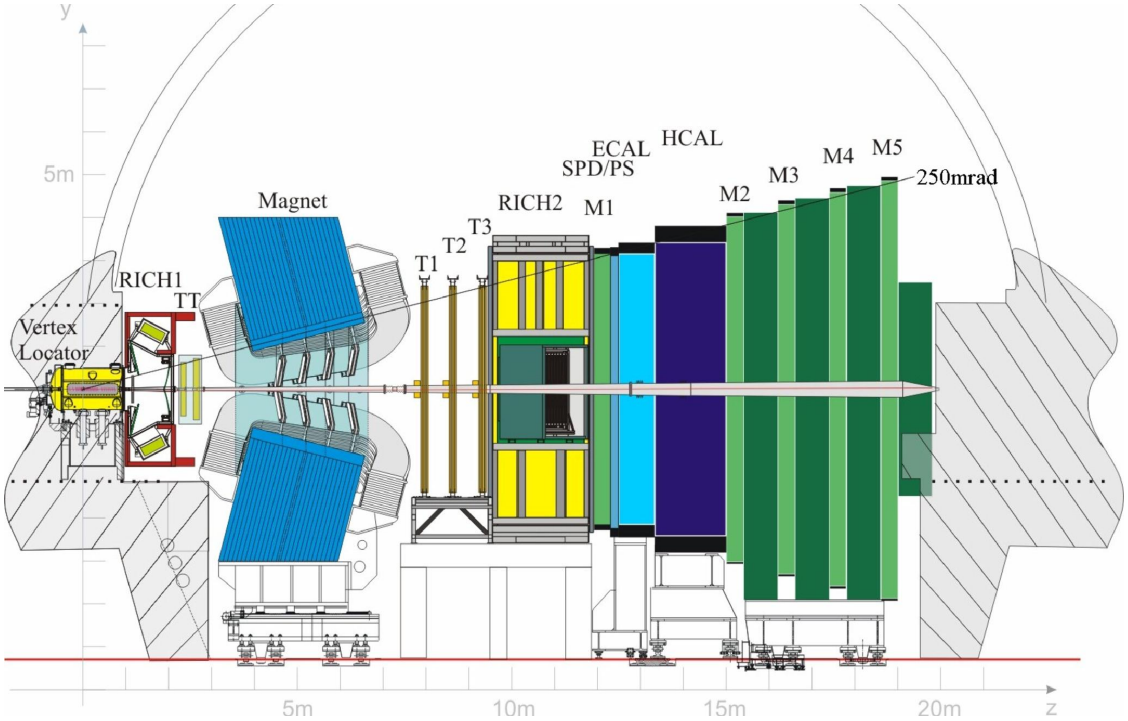

Figure 3.2: Layout of the LHCb detector in the $[y, z]$ plane, where the z axis is aligned with the beam direction. This layout corresponds to Run 1 and Run 2 of data taking [7].

good reconstruction performances. Reconstructed tracks in the VELO are used to construct the PVs. Figure 3.4 shows the PV resolution along x and z for four years of data taking, as a function of the number of tracks associated to the primary vertex. The resolution of the x and y components of the impact parameter (IP, defined as the transverse distance of closest approach between a particle trajectory and a vertex) as a function of the transverse momentum (p_T) is shown in Fig 3.5. The IP resolution approaches 11 μm for very high p_T tracks.

3.2.2 The Magnet and Tracking system

The LHCb tracking system includes also a large-area silicon-strip detector located upstream (TT) of a dipole magnet, and three stations of silicon-strip detectors and straw drift tubes placed downstream of the magnet (T1,T2,T3). A sketch of these elements is shown in Fig. 3.6, left. Two sectors can be identified in the three downstream stations. An inner segment, the Inner Tracker (IT), uses silicon microstrips detectors. The TT exploits the same technology. Together they form

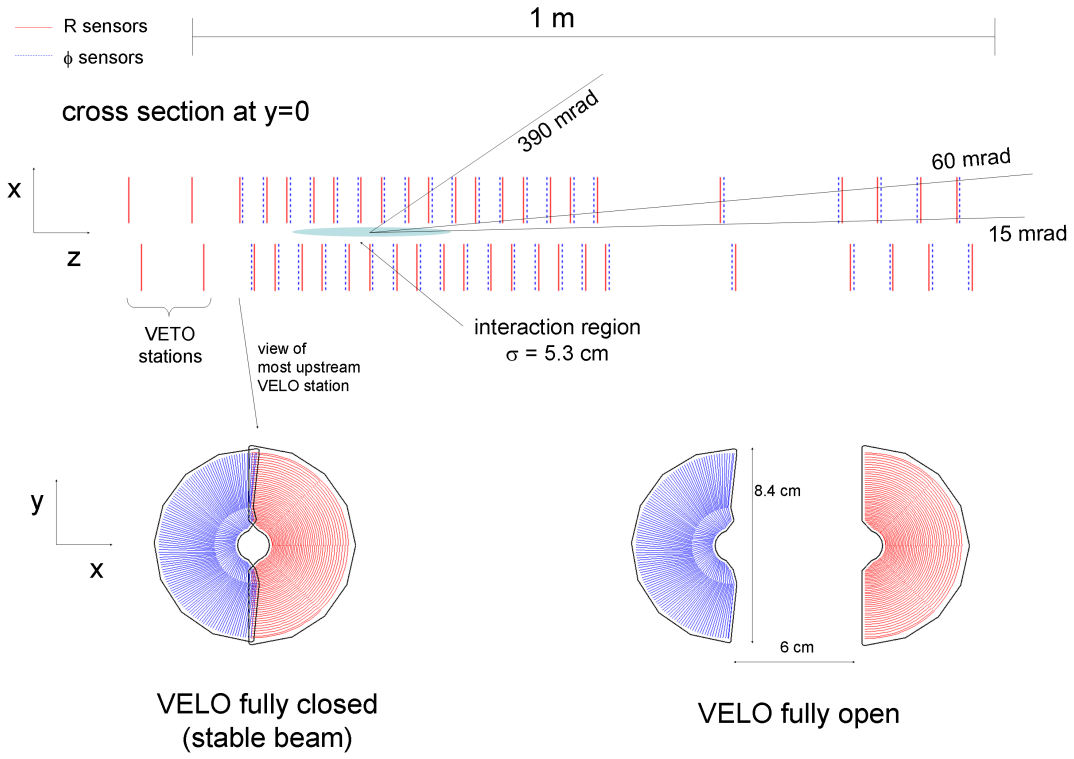

Figure 3.3: A schematic diagram of the Vertex Locator detector used in Run 1 and Run 2 [7].

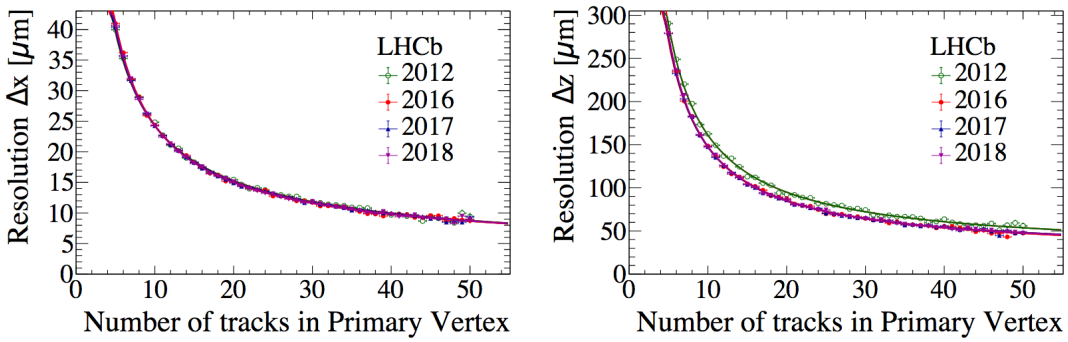

Figure 3.4: The primary vertex resolution along x(left) and z(right) over four years of data taking, as a function of the number of tracks in the PV [59].

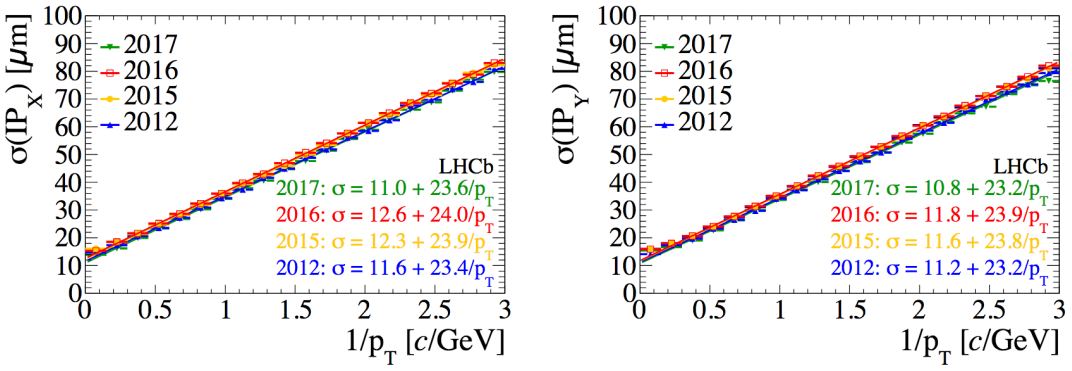

Figure 3.5: The resolution of the x and y components of the impact parameter as a function of the particle transverse momentum (p_T), over four years of data taking [59].

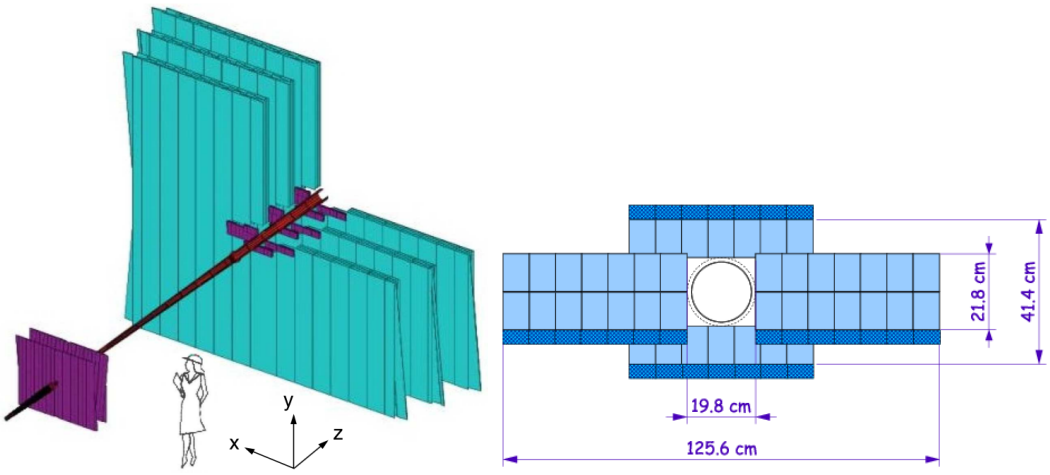

Figure 3.6: Left: the Silicon Tracker system (purple) and the Outer Tracker of the downstream tracking stations (light-blue). Right: details of the Inner Tracker [7].

the LHCb Silicon Tracker (ST), which is shown by the purple regions in Fig. 3.6 (left). The outer segment of the downstream tracking stations, the Outer Tracker (OT), consists of straw drift tubes and it is shown in light-blue in Fig. 3.6 (left). Each station is approximately 4.8 m along x and 5.8 m along y. Each station is split into two halves, retractable on both sides of the beam line. Each half consists of two independently movable units of two half layers, called "C-frames".

Sophisticated pattern reconstruction algorithms allow to reconstruct particle tracks in LHCb. The algorithm searches for hits in the tracking system (VELO, TT, IT and OT) and, by connecting them, determines the particle's trajectory in the tracking stations. A particle may not leave hits in all the tracking stations,

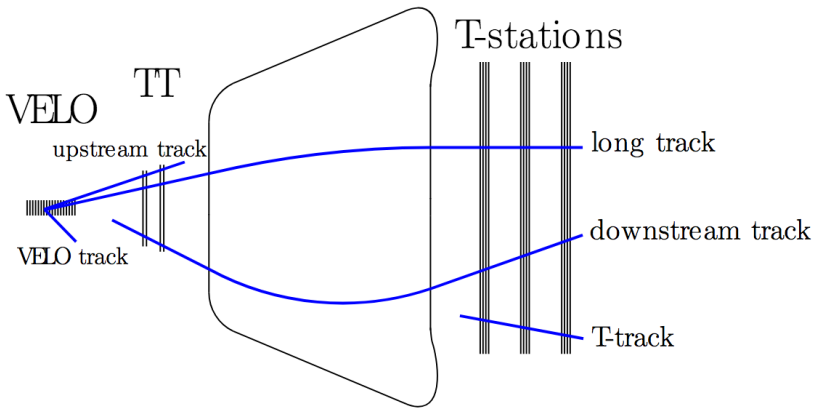

Figure 3.7: Sketch of the different types of tracks within LHCb [59].

but only traverse some of the tracking stations. This could be because the particle does not have enough energy to traverse all the tracking stations, or it could be the decay product of another particle decaying in the tracking stations. The tracking algorithm takes all these factors into account and is optimised to search for all possible tracks that can occur. Figure 3.7 shows the different track types that can be reconstructed. A VELO track contains only hits in the VELO detector. A T track has only hits in the T1-T3 stations. An *upstream* track has hits in the VELO as well as the TT. A *downstream* track has hits in all of the tracking stations except from the VELO. A *long* track has hits in all of the tracking stations.

A dipole magnet placed between the TT and the tracking station T1 provides the magnetic field of the LHCb detector [60]. A sketch of the magnet layout is shown in Fig. 3.8. The magnet has a bending power of 4 T m in the y direction for a 10 m length. It consists of two saddle-shaped aluminium coils, arranged in an iron yoke. The maximum magnetic field strength in the centre of the magnet is 1.1 T, as shown by the right plot in Fig. 3.8. The LHCb dipole magnet is a "warm" magnet that does not require cryogenic cooling. This permits a rapid ramp-up of the field, allowing the polarity to be reversed on a regular (roughly bi-weekly) basis. Similar amounts of data are collected in the so called *magnet-up* (positive y direction) and *magnet-down* (negative y direction) configurations. This procedure allows to evaluate any left-right asymmetry introduced by the detector.

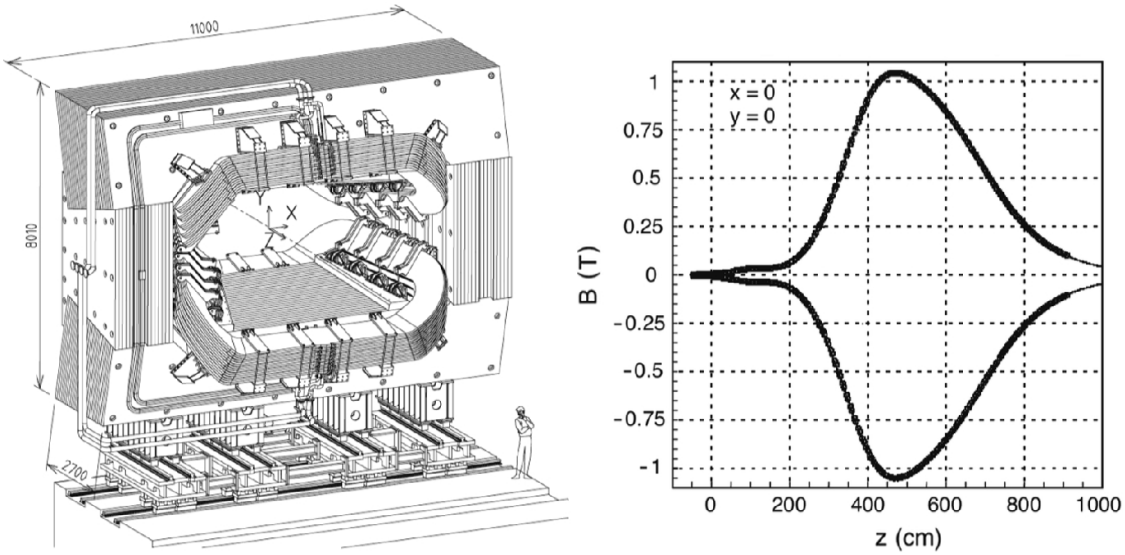

Figure 3.8: Left: view of the LHCb magnet (units in mm). Right: magnetic field along the z axis [7].

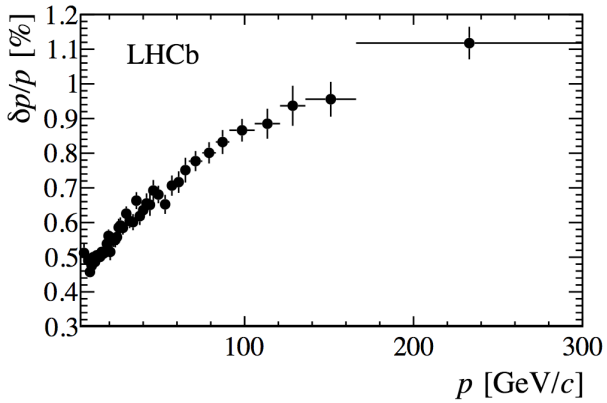

Figure 3.9: Relative momentum resolution versus momentum for long tracks in data obtained using $J/\psi \to \mu^+\mu^-$ decays [40].

The performance of the LHCb tracking system is quantified by the tracking efficiency and the momentum resolution. The tracking efficiency is defined as the probability that the trajectory of a charged particle that has passed through the full tracking system is reconstructed. It has been measured in Run 2 data using $J/\psi \to \mu^+\mu^-$ decays. The tracking efficiency is above 95% [61]. The momentum resolution, $\delta p/p$, varies from 0.5% for low momentum particles (less than 20 GeV), to 1.0% for particles around 200 GeV, and is shown in Fig. 3.9.

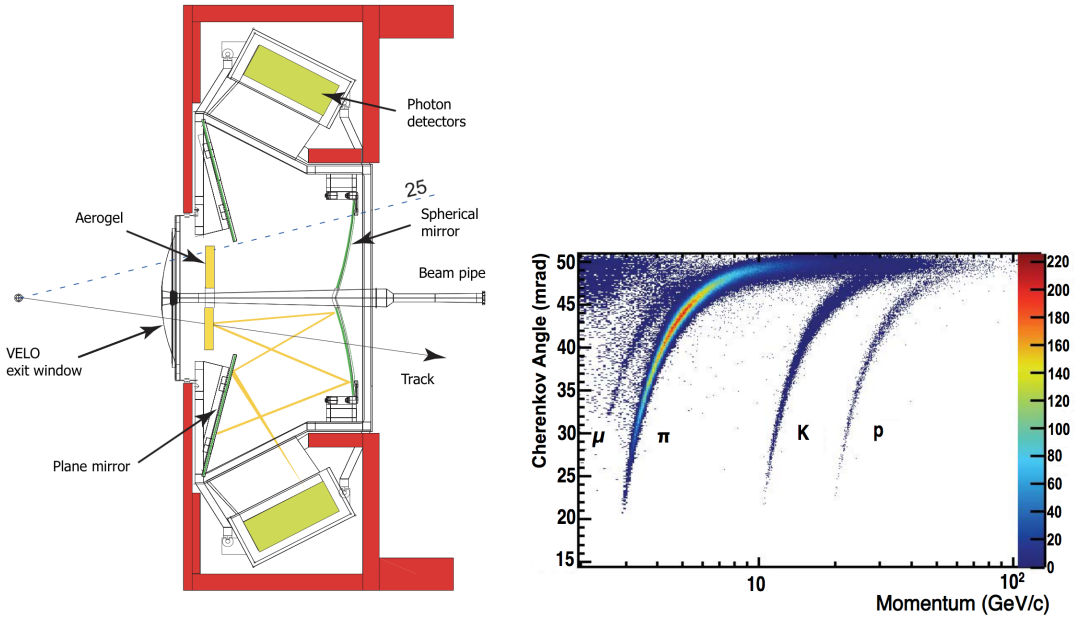

Figure 3.10: Left: optical scheme of the RICH detectors [7]. Right: reconstructed Cherenkov angle as a function of track momentum in RICH1 [40]. The Cherenkov bands for muons, pions, kaons and protons are clearly visible.

3.2.3 The Ring Imaging Cherenkov detectors

The Ring Imaging Cherenkov (RICH) detectors, schematised in Fig. 3.10 (left) exploit the Cherenkov effect to discriminate charged hadrons (pions, protons and kaons) over a broad momentum range. The Cherenkov effect occurs when a charged particle travels in a medium with a velocity v larger than the speed of light $c' = c/n$, where n represents the refraction index of the medium. In this case photons are emitted within a cone along the particle direction of flight, with an opening angle θ that depends on v and n and is given by:

$$\cos\theta = \frac{1}{n\beta} = \frac{c}{nv}, \quad \text{with } \beta = \frac{v}{c}. \tag{3.1}$$

Combining the measurement of a charged particle velocity with its momentum p, which is given by the curvature radius of the particle under the magnetic field effect, it is possible to have information on its mass. Figure 3.10 (right) shows the reconstructed Cherenkov angle as a function of track momentum. The Cherenkov bands for muons, pions, kaons and protons are clearly visible. The LHCb detector includes two RICH sub-detectors, named RICH1 and RICH2, covering different

ranges of momentum in order to efficiently discriminate charged hadrons. The RICH1, located before the magnet, is designed to efficiently identify low momentum tracks, approximately between 1 GeV and 60 GeV. During the Run 1, the RICH1 was filled by two radiators: aerogel ($n = 1.03$) and C_4F_{10} ($n = 1.0014$) while in the Run 2 the aerogel is removed from the gas mixture. The RICH1 covers an angular acceptance of 25-300 mrad and 25-250 mrad in the x and y direction, respectively. The RICH2 is placed after the tracking stations and uses CF_4 (n = 1.0005) as radiator, covering a momentum range between 15 GeV and 100 GeV. RICH2 covers an angular acceptance of about 120 mrad in the vertical plane and about 100 mrad in the horizontal plane. Cherenkov light is focussed onto two photodetector planes by two sets of spherical and plane mirrors. The photodetector planes are separated from the radiator gas by two transparent planes of quartz called *windows*. A detailed overview of the features of the quartz windows, including the requirements on their performance for the LHCb Upgrade I, will be given in Chapter 4.

3.2.4 The calorimeters

Measurements of the energy of charged hadrons, electrons and photons are provided by a calorimeter system consisting of scintillating pad (SPD) and preshower (PS) detectors, an electromagnetic calorimeter (ECAL) and a hadronic calorimeter (HCAL). The interaction of several particle species with different elements of a detector is shown in Fig. 3.11. The signature left by the track in each subdetector allows to discriminate between different particle species. The SPD and the PS are in place to provide information for background rejection in the ECAL. They are scintillating pad detectors, separated by a 15 mm thick lead absorber. The SPD identifies charged particles and is used to discriminate between electrons and photons. The lead layer in the middle of the two detectors is used to initiate electromagnetic showers from electrons and photons via bremsstrahlung radiation and pair production. The charged particles created in the showers are then measured in the PS, which enables the separation of electrons and charged pions.

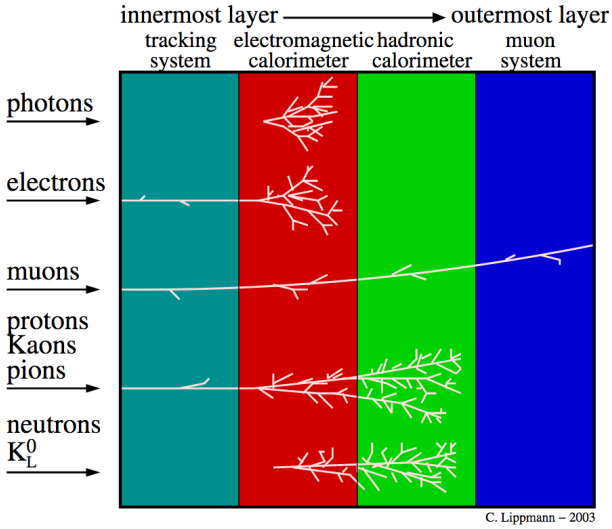

Figure 3.11: Interaction of several particle species with different subdetectors [62].

The ECAL is a sampling calorimeter designed with alternating 2 mm thick lead absorber layers and plastic scintillating material layers of 4 mm thickness. The photons generated in the scintillating layers are transmitted to wavelength-shifting fibres. The ECAL is able to provide information about the energy and the position of the electromagnetic showers produced by photons and electrons. The thickness of the ECAL, designed to expand over 25 radiation lengths, is large enough to fully contain the electromagnetic showers. The clusters of energy deposited in the ECAL are summed to calculate the initial particle energy. The ECAL energy resolution can be parameterised as [63]

$$\frac{\sigma(E)}{E} = \frac{10\%}{\sqrt{E/\text{GeV}}} \oplus 1\%, \tag{3.2}$$

which is the quadrature sum of a stochastic term that represents statistics-related fluctuations and a constant term which accounts for detector non-uniformity and calibration uncertainty. The sampling structure of the HCAL consists of 16 mm thick steel absorber layers alternated to scintillating material layers of 4 mm thickness. The HCAL measures the energy deposited by kaons, pions, protons and neutrons. Its main purpose, however, is to detect high p_T hadrons (a distinctive signature of many analyses of interest) and deliver this information for use in the trigger. The

energy resolution of the HCAL can be parameterised as [64]

$$\frac{\sigma(E)}{E} = \frac{(69 \pm 5)\%}{\sqrt{E/\text{GeV}}} \oplus (9 \pm 2)\%. \tag{3.3}$$

3.2.5 The muon stations

Excellent performance in the reconstruction and identification of muon tracks are crucial for many analyses of the LHCb physics programme, including the measurement of m_W. The muon system consists of five muon stations (M1-M5) and is fundamental for the identification and trigger of particle decays into final states containing high p_T muons. A schematic view of the muon stations is shown in Fig. 3.12. Station M1 is located in front of the calorimeters and is used to improve the transverse momentum measurement in the first level hardware trigger. The M2-M5 stations are separated by 80 cm thick iron absorbers to remove the contribution of remaining non-muonic particles. Each station is divided into four regions (R1-R4), shown in Fig. 3.12 (right), with finer segmentation in the regions closer to the beam pipe, which are subjected to higher track multiplicity. All the regions use the Multi-Wire Proportional Chambers (MWPC) technology except for the innermost (R1) region of the M1 station, where triple Gas Electron Multiplier (GEM) chambers are preferred. This choice is due to the largest particle flux that exceeds the limits of radiation tolerance of the MWPC.

The muon system provides information for the selection of high p_T muons at the trigger level [65] and for the muon identification [66]. Muon identification at LHCb can be obtained by applying the following selection criteria:

- A loose binary selection (`IsMuon`) of muon candidates which provides high efficiency while reducing the mis-identification probability of hadrons to the percent level. Each track is extrapolated from the downstream tracking system into the muon stations and hits are searched withing a cone around the track. The binary selection is defined according to the number of stations where a hit is found. The number of stations required to have a muon signal is a function of track momentum (p), as shown in Table 3.1. Low momentum muons do

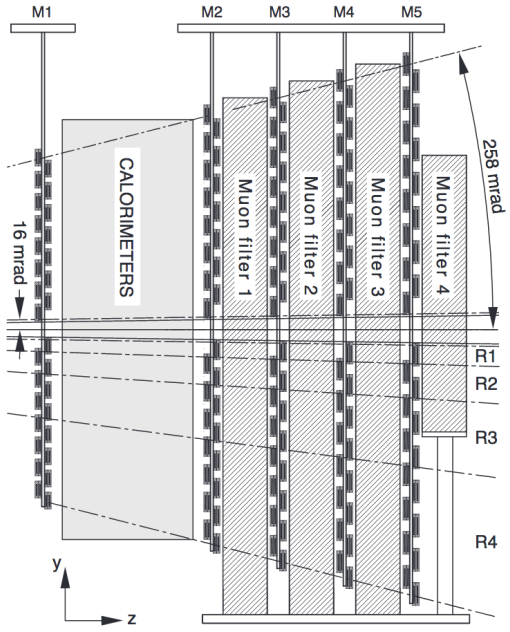

Figure 3.12: Schematic view of the LHCb muon system [7].

Table 3.1: `isMuon` criteria for different muon momentum ranges [66].

Momentum range (GeV)	Muon stations with hits
$3 < p < 6$	M2 and M3
$6 < p < 10$	M2 and M3 and (M4 or M5)
$p > 10$	M2 and M3 and M4 and M5

not traverse the whole muon systems. Muons with $p < 3\,\text{GeV}$ do not traverse the muon systems at all because of the bending power of the magnet.

- The muon identification can be further improved by a selection based on the logarithm of the ratio between the likelihoods for the muon and non-muon hypotheses (`muDLL`). The information from the muon system can be combined with the likelihoods provided by the RICH1, RICH2 and calorimeters to further improve the muon identification performance.

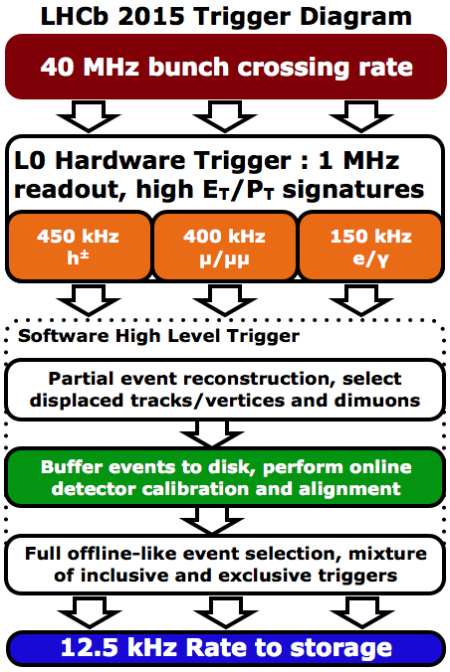

Figure 3.13: Diagram of the workflow of the LHCb trigger during the Run 2 [67].

3.2.6 The trigger system

The LHC bunch crossing is 40 MHz. A typical event size is $\mathcal{O}(100\,\text{kB})$. This means that in order to store all of the events TB of disk space would be necessary, and most events would not contain physics processes of interests in any case. A complex system of fast algorithms is implemented to decide whether an event is of interest and deserves to be stored or not. It is conventional to refer to a single trigger classification algorithm as a *line*, so that a trigger consists of a set of trigger lines. This section describes the LHCb trigger configuration in Run 2.

The LHCb trigger system consists of three stages: a *Level 0* (L0) hardware trigger which performs basic operations using information from the calorimeters and muon systems. L0 is followed by two stages of software trigger called *High Level Trigger* (HLT1 and HLT2) that can be performed on a separate CPU farm and after which full event reconstruction is achieved. The working flow of the LHCb trigger is schematised in Fig. 3.13. At the end of the full trigger chain, the rate at which the events are saved passes from 40 MHz to 12.5 kHz.

Hardware trigger

The hardware trigger (L0) reduces the event rate from the original 40 MHz of bunch crossing down to 1 MHz. This is done using fast detectors that provide the basic information to calculate the p_T of electrons, photons, hadrons and muons, without using time-consuming and complicated algorithms. The L0 trigger has three independent sub-systems running in parallel. These subtriggers are denoted `L0Calorimeter` for the hadrons, `L0Muon` for the muons and `L0Electron` (`L0Photon`) for electrons (photons). The typical allocated bandwidths for the three categories are 450 kHz, 400 kHz and 150 kHz. The `L0Calorimeter` and `L0Muon` are given a larger event processing rate because the predominant decay products from b hadrons at LHCb are muons and other hadrons.

The electromagnetic trigger uses the information provided by the ECAL, the PS and the SPD. Events with at least one cluster with measured transverse energy (E_T) above a certain threshold are selected. A single calorimeter cluster is defined as two-by-two calorimeter cells. The transverse energy of a cluster is defined as:

$$E_T = \sum_{i=1}^{4} E_i \sin\theta_i, \tag{3.4}$$

where E_i is the energy deposit in the $i-th$ cell and θ_i is the angle between the z-axis in the LHCb coordinate systems and the direction formed by the interaction point and the $i-th$ cell's centre.

Along the same lines the hadronic trigger, which uses the HCAL information, selects events with at least one hadronic cluster with E_T greater than a certain threshold. In addition to the total E_T deposit, the SPD multiplicity (defined as the total number of SPD cells with a hit, n_{SPD}) information is also stored. To reduce the complexity of events and, hence, to enable a faster reconstruction in the subsequent software stage, a requirement is placed on the maximum n_{SPD} in most `L0` trigger lines. This multiplicity cut is referred to as a Global Event Cut [7].

The muon trigger uses the information from the muon stations to perform a fast track reconstruction. Muon tracks are reconstructed using the positions where the muons interacted with the five stations, thus determining the muon transverse

momentum. The L0Muon has been optimised so that it is 95% efficient at detecting muons in the LHCb experiment. Two algorithms are used: L0Muon searches for muons with the largest p_T while L0DiMuon searches for the largest p_T from combining pairs of muons. The analysis presented in this thesis makes use of a particular L0MuonEW trigger line, developed for high p_T muons in electroweak processes, that accepts only muon tracks with $p_T > 6\,\text{GeV}$ [59]. A special feature of the L0MuonEW line is that no Global Event Cut is applied in order to avoid systematic uncertainties associated with the determination of the corresponding efficiency.

Software trigger

The High Level Trigger (HLT) is controlled by a software based C++ application, named Moore [68], that performs a fast full reconstruction of candidates. The HLT is split into two stages, HLT1 and HLT2.

HLT1 reduces the event rate from 1 MHz down to 40-80 kHz by performing a *partial* event reconstruction using the information from the VELO, tracking stations and muon stations. HLT1 reconstructs the trajectories of charged *long* tracks, with $p_T > 500\,\text{MeV}$. In addition, a precise reconstruction of the PV is performed. Because of timing constraints in HLT1, most particle identification algorithms cannot be executed except for the muon identification (which is favoured by the clear signature left by the muons in the LHCb detector). After this stage, events are temporarily saved on a buffer disk where the alignment and calibration of the full detector takes place in real-time before reaching HLT2. The detector alignment and calibration consists of several tasks (e.g. alignment of the VELO, tracking stations, MUON, RICH mirrors; calibrations of the global time in the OT and of the RICH detectors gas refractive index, *etc.*). The data to used to complete each subtask is obtained from the output of HLT1. The alignment and calibrations are performed at regular intervals, and the resulting alignment and calibration constants are updated only if they are significantly different from the current values [69].

The second stage of the software trigger (HLT2) is a sophisticated set of algorithms that is used to perform a *full* event reconstruction. This consists of three

main steps: the reconstruction of charged tracks (improving the track reconstruction from HLT1), reconstruction of neutral particles and particle identification (adding the information from the RICH and the calorimeters to the information from the muon stations already available in HLT1). This is a significant improvement with respect to Run 1, where the HLT2 reconstruction was a simplified version of the offline reconstruction, and where the detector alignment and calibration parameters were calculated offline from already triggered data. With the computing strategy adopted in Run 2, the quality of the online reconstruction matches that of the offline reconstruction. This also enables the possibility to perform physics analyses using candidates directly reconstructed in the trigger and bypassing the offline reconstruction. In the so called *Turbo* stream [70] the trigger saves to disk a set of physics objects containing all information necessary for analyses and discard the raw event. This feature is particularly important for analyses characterised by large rates of events of interest but limited by trigger output constraints. Most analyses, including the one presented in this thesis, still require more information in the event reconstruction. Therefore, they continue to use the usual data flow with the offline reconstruction. In the present analysis, the signal trigger for muons coming from W and Z decays needs to efficiently trigger prompt muons and exploits their very high p_T. This is implemented in the `Hlt1SingleMuonHighPT` and `Hlt2SingleMuonHighPT` trigger lines. The first line selects good quality tracks identified as muons with a relatively large transverse momentum of $p_T > 4.8\,\text{GeV}$. The `Hlt2SingleMuonHighPT` line is set up analogously to its HLT1 counterpart. However, the p_T cuts are higher ($p_T > 10\,\text{GeV}$) as the rate budget in HLT2 is much tighter than in HLT1. Furthermore, the HLT2 trigger lines are less generic than those in HLT1 since they are designed to select events for specific physics studies.

The filtering applied at the HLT2 stage reduces the rate of events which are then saved to data disk to 12.5 kHz. Triggered, raw data are reconstructed offline by the Brunel [71] application to transform the detector hits into objects such as tracks and clusters. The objects are stored into an output file in a "Data Summary Tape" (DST) format. Reconstructed events are further filtered through an additional set

of selections by the DaVinci [72] application. This stage is called *stripping*. To save disk space and to speed up access for analysts, the output files are grouped into *streams* which contain similar selections. For example, the events considered in the m_W measurement described in this thesis are selected by the electroweak (EW) stream. The main stripping lines used in the analysis are:

- `WmuLine`: selects events with a single muon with $p_T > 15\,\text{GeV}$;
- `Z02MuMuLine`: select events with two oppositely charged muons with $p_T > 15\,\text{GeV}$ and a combined invariant mass greater than $40\,\text{GeV}$.

DaVinci is also used in the final step of the data flow to produce the ROOT [73] ntuples to be used in physics analyses.

3.2.7 Simulation

Simulated events are used in LHCb to evaluate selection efficiencies, model kinematic distributions and mimic backgrounds. They are processed in a very similar way to the data, so that they can mimic the same inaccuracies of the data flow (which is a key requirement to provide unbiased efficiencies calculations).

Simulated pp collisions are generated using Pythia [49], with parton distribution functions provided by the CT09MCS [48] set. Final-state radiation is modelled using Photos [74]. Decays of hadronic particles are described by EvtGen [75]. The interaction of the generated particles with the detector, and its response, are implemented using Geant4 [76]. The simulated collisions, the hadronisation and decay of the resulting particles, are controlled by the Gauss application [77]. The simulated hits in the virtual detector are converted to signals that mimic the real detector by the Boole [78] application. The output of Boole is designed to closely match the output of the real detector, therefore the simulated events can be injected into the data processing chain described above, starting with the trigger.

4

RICH1 quality assurance measurements for the LHCb Upgrade I

From 2022 LHCb will enter a new phase of data-taking (Run 3) and face new challenges driven by the higher instantaneous luminosity at which the detector will operate. A new detector is currently being commissioned to respond to the more challenging demands of the data-taking conditions. This chapter introduces the main changes in the detector, and will focus on the quality assurance (QA) measurements that have been performed between 2018 and 2019 on the quartz windows to be installed in the upgraded RICH1 detector. This chapter describes in detail the transmission measurements performed by the author. Nevertheless, for completeness, a few examples of other notable measurements which evidenced issues in the quartz performance are also reported.

4.1 The LHCb Upgrade I

During Run 1 and Run 2 LHCb has collected roughly 9 fb^{-1} of integrated luminosity. However, many analyses of interest for the LHCb physics programme are still limited by statistical precision. Since the integrated luminosity doubling time would be prohibitively long, an increase in the instantaneous luminosity is required. For hadronic decays of beauty and charmed mesons, the efficiency of the current detector is already

saturated at the Run 2 luminosity because of the L0 hardware trigger performance. A prerequisite for a luminosity increase is therefore removing the hardware trigger and using a full software trigger running at the full bunch crossing rate.

An upgrade of the LHCb detector (Upgrade I), to be installed during the Long Shutdown 2 (LS2) of the LHC, has been proposed [79]. It is expected that the new LHCb detector will collect up to $50\,\mathrm{fb}^{-1}$ in seven years of data-taking, which corresponds to five times the integrated luminosity of Run 1 and Run 2 combined. To achieve this goal the LHCb detector readout rate will be upgraded from the current 1 MHz to the LHC maximum bunch crossing rate of 40 MHz. The L0 trigger will be removed, and the online selection of events will be uniquely performed by a new software-only trigger that will enable to process signal data in an upgraded CPU farm at an input rate higher than before. In order to sustain the increased luminosity, several sub-detectors will be upgraded with higher granularity and greater radiation hardness. All sub-detectors require new readout electronics, irrespective of whether the sensors are new or not.

For the largest and heaviest LHCb devices, namely the calorimeters and muon stations, the detector elements will remain mostly in place. All the other LHCb detector systems are going to be entirely replaced. A scheme of the upgraded LHCb detector is shown in Fig. 4.1. A brief description of the various subdetector modifications is reported below.

The VELO is one of the key detectors to be upgraded during LS2. The current system based on silicon microstrip modules is replaced by silicon pixel technology, which offers better hit resolution and simpler track reconstruction. The new VELO will also be closer to the beam axis, which poses significant design challenges. The Upstream Tracker (UT) will be used for downstream reconstruction of long lived particles decaying after the VELO. It will also be essential to improve the trigger timing and the momentum resolution. The UT will be composed of four tracking layers based on silicon strip technology. The inner sensors will be closer to the beam pipe with respect to the current tracker, in order to increase the geometrical acceptance.

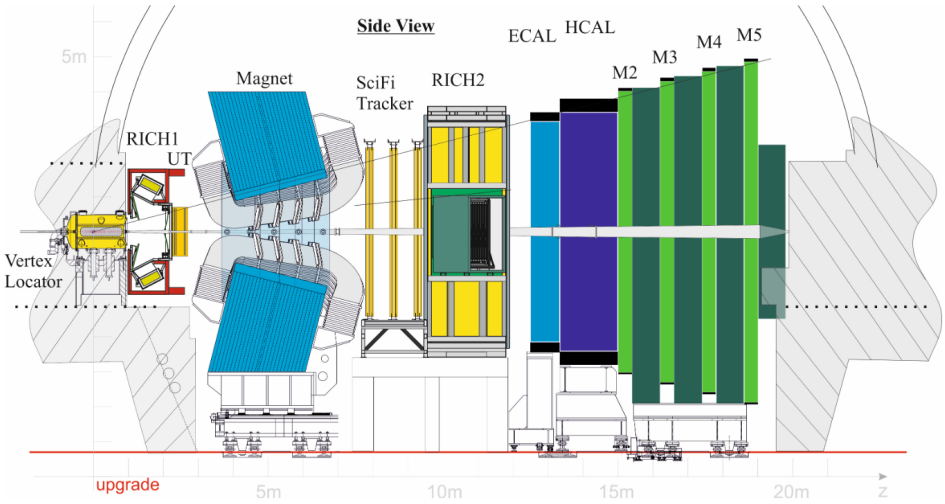

Figure 4.1: Side view of the LHCb detector in the Upgrade I [79].

Downstream of the magnet, a new tracker (SciFi) based on scintillating fibres and read out by silicon photomultiplier (SiPM) arrays, replaces the drift straw detectors and silicon microstrip sensors used by the three tracking stations in Run 1 and Run 2. The SciFi represents a major challenge for the collaboration, not only due to its complexity, but also because the technology has never been used for such a large area in such a harsh radiation environment. The usage of UT hits in the track extrapolation from the VELO to the SciFi detectors will allow to reduce the number of fake tracks reconstructed by the tracking algorithms by a factor 50-70%. Consequently, the trigger timing will be largely improved.

The upgraded RICH will still be composed of the RICH1 and RICH2. The optics of RICH2 is unchanged. However, the mirror system of RICH1, which is required to deflect and focus Cherenkov photons onto photodetector planes, will be replaced to cope with the much increased particle densities of future LHC runs. A larger gas enclosure will also be used to accommodate the required changes. The arrows in Fig. 4.2 highlight the mechanical and optical system modifications of the upgraded RICH1 detector, compared to the current one.

The current RICH employs hybrid photodetectors (HPD), which will be replaced in both RICH detectors by commercial Multi-anode Photo-Multiplier Tubes

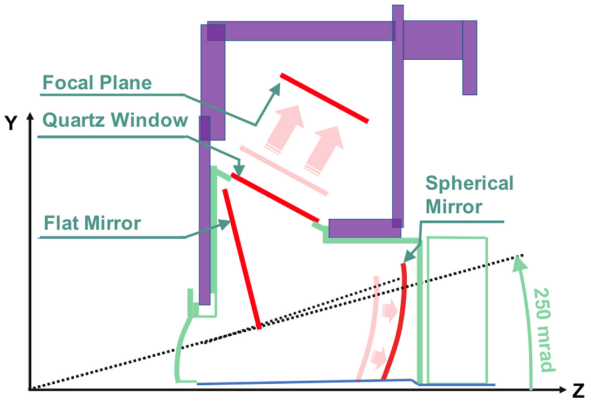

Figure 4.2: Schematic drawing of the mechanical and optical system modifications of the upgraded RICH 1 detector. The arrows indicate the system modifications, compared to the current detector [80].

(MaPMTs) and new front-end electronics [81]. During the upgrade of the RICH1 optical system in the LS2, several Quality Assurance measurements (QA) on each component have been performed. These measurements are necessary to ensure that the subdetector complies with the standards required. The following sections describe the QA measurements on the *quartz windows* installed in the RICH1 subdetector for the LHCb Upgrade I. Their position can be seen in Fig. 4.2.

4.2 The RICH1 quartz windows

The Cherenkov light produced in RICH1 is focussed onto the lower and upper photodetector planes by spherical and planar mirrors. The photodetector planes are separated from the C_4F_{10} radiator gas by two transparent planes of quartz, called *windows*. Each window is divided into three segments of quartz (plates), each with dimension $655.0 \times 475 \times 8\,\text{mm}$. The three plates are assembled and glued together and then mounted and sealed into a pair of aluminium frames which will then be installed into the RICH1 gas enclosure.

The quartz plates are produced from a sample of Spectrosil® 2000, provided by the company Heraeus (Germany). The following requirements were specified:

- transmission of 90% or better for light at normal incidence for wavelengths between 270 nm and 600 nm, and a transmission of around 70% or better for

wavelengths between 220 nm and 270 nm. Spectrosil® 2000 is expected to exceed this performance;

- the large front and back faces should be polished to a surface quality of 60/40 DIG and conform to standard MIL-0-13830 [82]. These standards are described in greater detail in Section 4.5.

In order to check these requirements, nine small representative samples (denoted as *coupons*) of Spectrosil® 2000 with dimension $50 \times 50 \times 8$ mm, taken from the same production batch as the six plates, were shipped to CERN in November 2018. For reference, one of the coupons and one of the large plates are shown on the left and right hand side pictures of Fig. 4.3, respectively. The final acceptance criteria of the six quartz plates are based on quality assurance measurements performed upon delivery at CERN. The measurements were conducted between December 2018 and May 2019 at the CERN Optics Laboratory, and include:

- an estimate of the transmission performance of the quartz samples over a wide range of wavelengths;

- a visual inspection for the assessment of digs and scratches at the sample surfaces.

This chapter will focus in greater detail on the transmission measurements on the quartz coupons, and will briefly describe the key parameters examined in the visual inspection for digs and scratches. A detailed description of the visual inspection on the large quartz plates is reported in Ref [83].

4.3 Transmission measurements

4.3.1 The transmission spectrum

Optical glasses are optimized to provide excellent transmittance throughout the total visible range from 400 to 800 nm. Usually the transmittance range spreads also into the near ultra-violet (UV) and infra-red (IR) regions. The dependence of the transmittance on the wavelength varies as a function of the sample's refractive

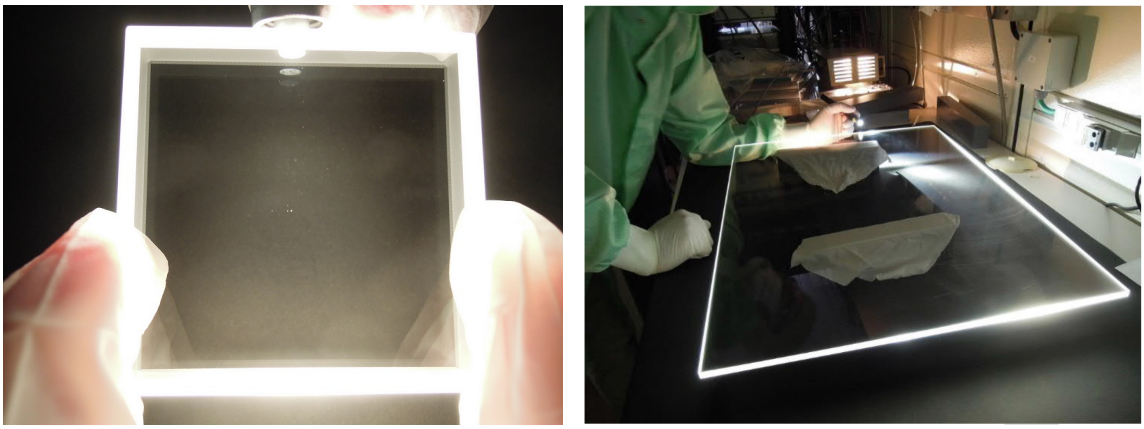

Figure 4.3: Left: one of the nine Spectrosil® 2000 coupons delivered to CERN. Right: one of the six large quartz plates during the visual inspection [83].

index, its thickness, and surface quality. The following paragraphs will provide a brief description of the transmittance properties of optical glass.

A light beam with intensity I_0 falls onto a glass plate with thickness d, as shown in Fig. 4.4. At the entrance surface (denoted as *interface*), part of the beam is reflected. The resulting intensity of the beam will be $I_{i0} = I_0(1-r)$ with r being the reflectivity. Inside the glass, the light beam is attenuated. Its intensity decreases according to an exponential law such that, at the exit surface, the beam intensity is:

$$I_i = I_{i0}e^{-kd}, \tag{4.1}$$

where k is the absorption coefficient of the material. At the exit surface, another reflection occurs. The intensity of the *transmitted* beam is $I = I_i(1-r)$, and it can be expressed as a function of the intensity of the incident beam as

$$I = I_0(1-r)^2e^{-kd}. \tag{4.2}$$

The beam reflected at the exit surface returns to the entrance surface and it is divided into a transmitted and a reflected part. With multiple reflections taken into account, the *transmittance* of the glass plate is

$$\tau = \frac{I}{I_0} = P\tau_i, \tag{4.3}$$

with

$$\tau_i = \frac{I_i}{I_{i0}} \tag{4.4}$$

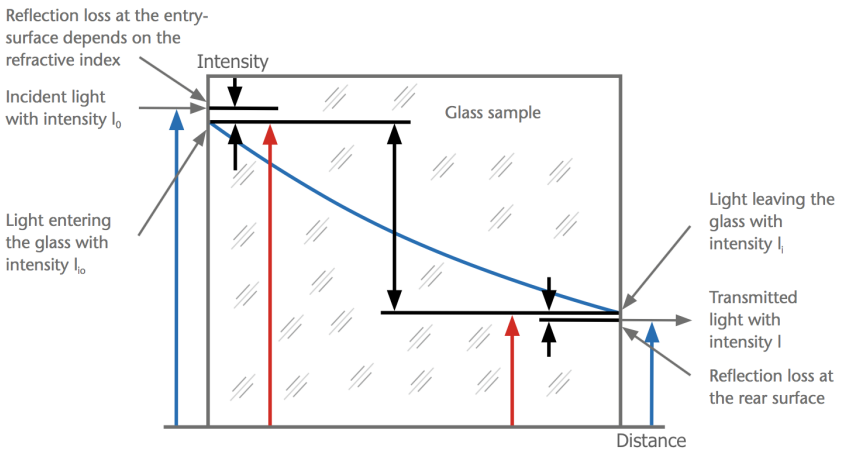

Figure 4.4: Change in the intensity of a light beam passing through a glass plate [84].

denoted as the *internal transmittance* and

$$P \approx \frac{2n}{n^2 + 1} \tag{4.5}$$

is called the *reflection factor* which can be derived from the Fresnel formula that describes the relation between reflectivity (r) and the refractive indices (n) of the material. Taking the refractive index range of optical glass from 1.4 to 2.1, the reflection factor ranges from 0.92 to 0.75 [84].

The transmittance depends on the thickness of the sample, its refractive index, but also on the wavelength of the incident radiation. Figure 4.5 shows the transmission spectrum of a sample of Spectrosil® 2000 of thickness 10 mm, from the documentation provided by Heraeus [85]. Two curves are shown, representing:

- the *internal* transmission spectrum (red), which accounts only for the absorption loss of the material;
- the transmission spectrum obtained including both the absorption loss of the material and the loss of light due to Fresnel reflection at the two glass surfaces (blue).

The latter is the actual spectrum that can be accessed via the quality assurance measurements. Both spectra extend over a wide range of wavelengths, with absorption effects (i.e. when the energy of a photon matches the energy needed to

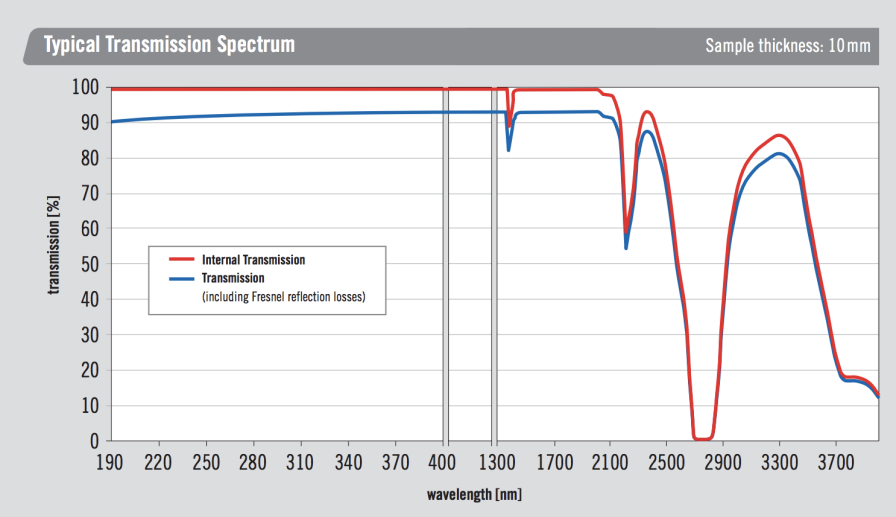

Figure 4.5: Transmission spectrum of a 10 mm-wide sample of Heraeus Spectrosil® 2000 according to the manufacturing company's specifications [85].

excite an electron within the glass to its higher energy state) leading to reduced trasmission above 1600 nm. However, for the purpose of the quality assurance measurements, the focus is on wavelengths spanning the UV and visible regions (i.e. the range 200-700 nm). Transmission should exceed 90% across the full range of interest, thus verifying the requirements listed in Sec. 4.2. A particular feature of the spectrum, denoted as *UV edge*, can be observed at the transition between the UV and the visible range. This point delineates the wavelength after which absorption effects do not dominate anymore and high-transmission can be achieved. The UV transmittance edge does not only depend on the composition of the glass but also on the thickness. A larger thickness shifts the transmittance edge to longer wavelengths.

4.3.2 Direct measurements

The transmission measurements are performed using a Perkin Elmer Lambda 650 UV-VIS spectrometer [86]. An image of the spectrometer is shown in Fig. 4.6 (left), while its setup is illustrated in Fig. 4.6 (right). Measurements can be made in a spectral range from 190 nm to 900 nm, which is covered by two lamps: a deuterium lamp for the ultraviolet (UV) section and a tungsten lamp for the visible (VIS) and near infrared (NIR) spectral regions. The tungsten lamp produces a continuous spectrum from the near UV throughout the rest of the spectral range.

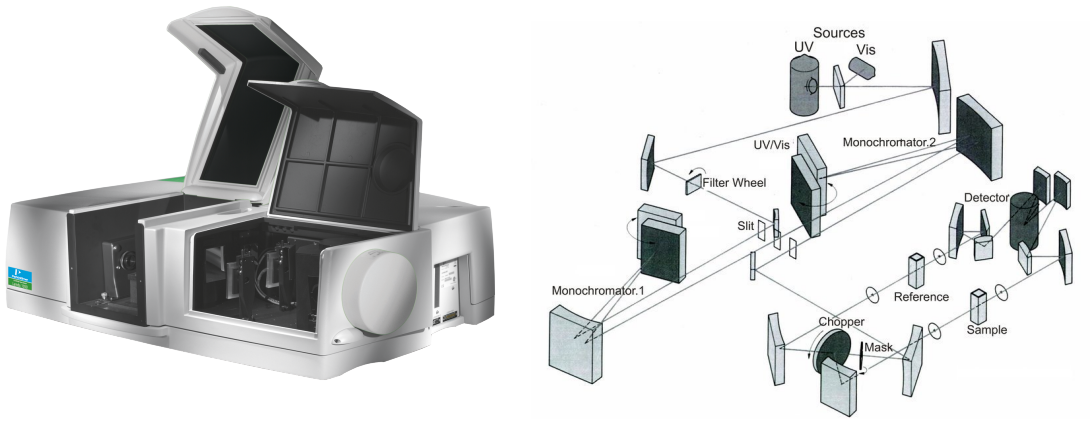

Figure 4.6: Left: Perkin Elmer Lambda 650 UV-VIS spectrometer [86]. Right: inside the spectrometer; the region of the sample holder is enclosed in the left hand side panel of the picture on the left. The region of the detector is enclosed in the other open panel [87].

The deuterium lamp, instead, allows to sample the wavelengths from 160 to 400 nm. For the present studies, the analysed range is restricted to 200-800 nm. The source beam is split by a mirror in order to generate two beams; one is directed through the sample and the other is used as a reference. The light is reflected using mirrors into a monochromator which only allows light of a single wavelength to reach the detector. The detector receives the signals from both the sample beam and the reference beam. Intensity is measured as the percentage of light transmitted by the sample (T) with respect to the reference. For the quality assurance measurements, two different detector setups are used and compared.

Standard Setup

The quartz coupon is placed in one of the spectrometer sample holders, about 50 cm distant from the detector that consists of a photomultiplier. The light beam is incident normally on the sample surface, which means that the detector measures the transmittance at *normal incidence*. Figure 4.7 shows the transmission spectra of four quartz coupons over the examined wavelength range. The transmission exceeds the required 70% threshold in the 220-270 nm range, and converges to a 93% plateau for larger wavelengths, thus satisfying the performance requirements. The small instability in the transmission spectrum that can be observed between 320 and

Figure 4.7: The transmission spectra of four quartz coupons measured using the standard setup of the Perkin Elmer Lambda 650 UV-VIS spectrometer.

380 nm can be attributed to the swap of the light-source lamp used in the sampling. This does not affect the overall conclusions on the samples' transmission performance.

Integration Sphere

The imperfections on a surface lead to light scattering and, in case the scattered light does not reach the detector, this leads to a biased determination of the total transmitted light by the sample. The standard detector setup can be substituted by a 150 mm integration sphere, available in the Perkin Elmer Lambda 650 set. Figure 4.8 shows the basic integration sphere setup. Light entering the sphere is reflected multiple times before it encounters the detector. The signal produced is proportional to the amount of light entering the sphere. Therefore, if the sample is placed at the entrance of the sphere, the *total* amount of light transmitted by the sample can be measured.

The integration sphere is a suitable setup to measure the fraction of diffused light by the sample. Two measurements are performed: in the first one the sample is placed at a 50 cm distance from the detector that was also used in the standard setup, allowing to measure the *direct* transmission (i.e. light that is not scattered, or only slightly scattered with respect to the incidence direction). This configuration can be directly compared with that obtained with the standard setup,

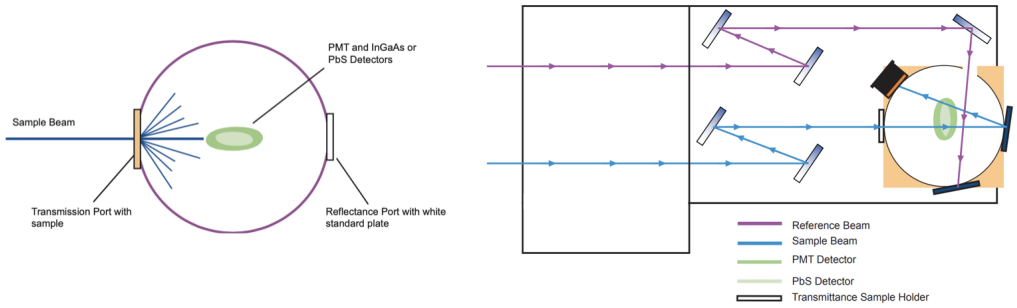

Figure 4.8: Left: light entering the integration sphere. Right: scheme of the integration sphere setup in the Perkin Elmer Lambda 650 UV-VIS spectrometer [86].

since the position of the sample is the same and the only element that changes is the detector. Figure. 4.9 compares the transmission spectra of the same quartz sample using the two approaches. Compatible results are observed from the two methods, as expected. It is important to mention that the wavelength sampling frequency adopted with the integration sphere is smaller than that adopted for the standard setup, and this is clearly visible in Fig. 4.9. Nevertheless, a qualitative comparison between the two setups can be performed. For the second measurement the sample is placed at the entrance of the sphere, and the *total* transmitted light is measured. The fraction of diffused light is defined as the difference between the total and direct transmission, divided by the total transmission. Figure 4.10 shows the diffusion spectra of four quartz coupons. The maximum loss of diffused light measured is 0.2%, which indicates that, within the instrumental error, no significant light scattering is observed.

4.4 Anti-reflecting coating

As light passes from air through an uncoated glass substrate, approximately 4% of the light will be reflected at each interface [88] due to Fresnel reflection (Fig. 4.11, left). This results in a total transmission of only 92% of the incident light, which can be detrimental in many applications. Anti-reflective (AR) coatings are applied to optical surfaces to improve their transmission performance and reduce biases caused by reflection of light that travels backwards through the system. The coatings are

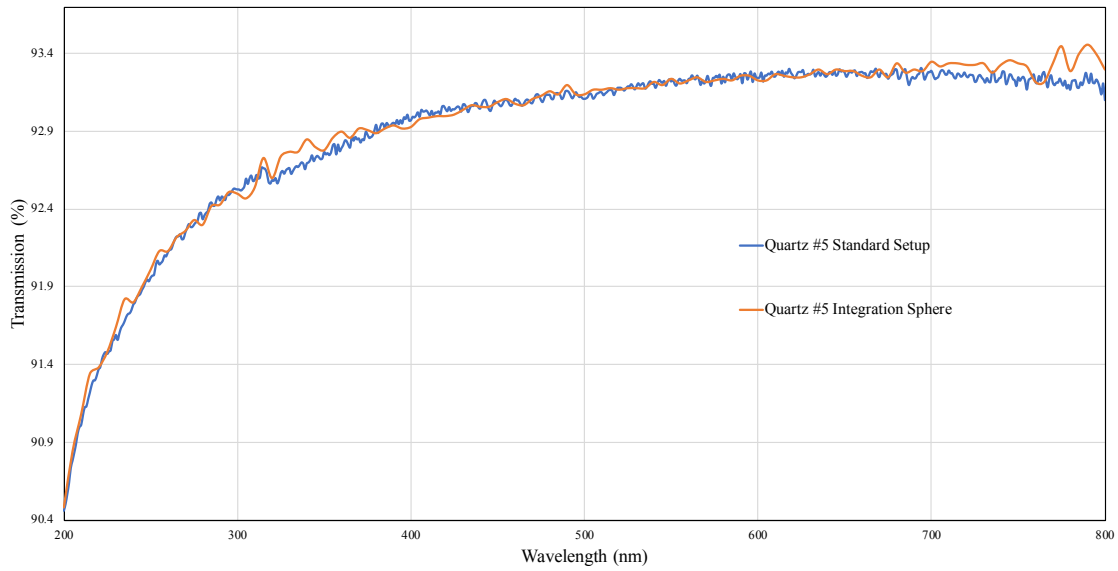

Figure 4.9: Transmission spectrum of one of the quartz coupons obtained with the standard spectrometer setup (blue) and with the integration sphere (orange).

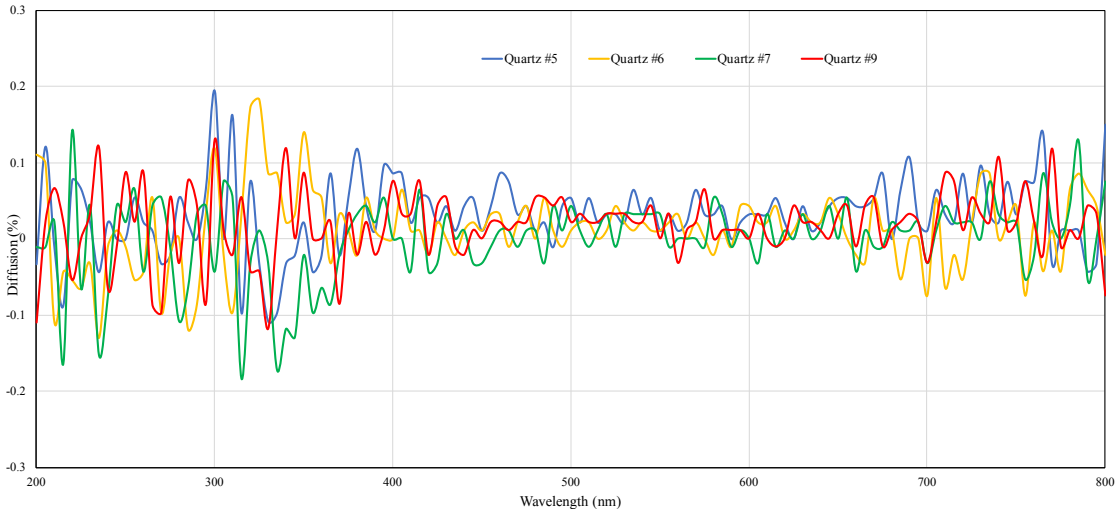

Figure 4.10: Diffusion spectra of the four quartz coupons, calculated from the corresponding transmission spectra obtained with the integration sphere detector setup.

especially important for systems containing multiple transmitting optical elements. Anti-reflective coatings are designed so that the relative phase shift between the beam reflected at the upper and lower boundaries of the thin coating film is 180°. Destructive interference between the two reflected beams then occurs, which cancels out both beams before they exit the surface (Fig. 4.11, right). To achieve the desired path difference of $\lambda/2$ between the reflected beams, the optical thickness of the optical coating must be an odd integer multiple of $\lambda/4$, where λ is the

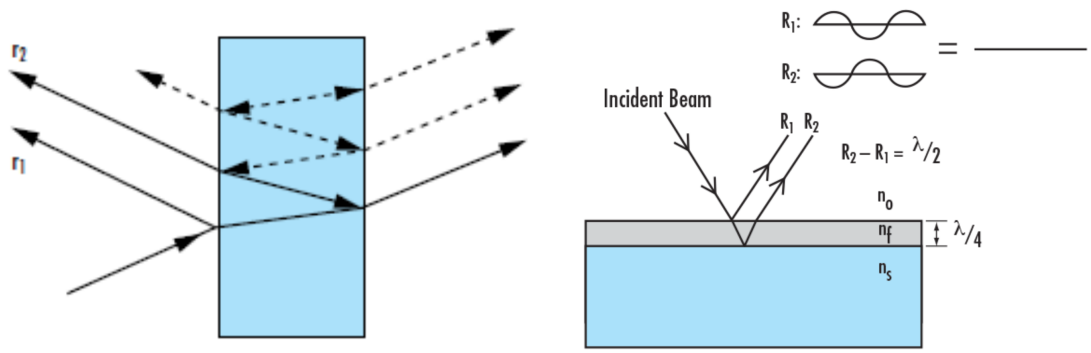

Figure 4.11: Left: multiple Fresnel reflections. Right: change in reflection after anti-reflecting coating of a surface [88].

wavelength being optimized for peak performance. When achieved, it will lead to the cancellation of the beams. The index of refraction of a thin film (n_f) needed for complete cancellation of the reflected beams can be found by using the refractive index of the incident medium (n_0) and the substrate (n_s) [88]:

$$n_f = \sqrt{n_0 n_s}. \tag{4.6}$$

Transmission performance of a quartz optical component after the application of a double sided anti-reflective coating are expected to improve by $\mathcal{O}(1)$ percent.

4.5 Visual inspection for surface imperfections

The surface quality of an optical component is evaluated by assessing the presence of surface imperfections, such as scratches and digs, which may be produced during the manufacturing or handling process. The quartz plates are required to meet a grade of “60-40" of the scratch and dig definition in the U.S. Military Performance Specification MIL-0-13830 [82]. The facilities at CERN do not allow a proper check of the entire quartz plates’ defects according to this standard (mainly because of their size). However, a careful observation of the optical components could already give indication if the single parts do not meet the required standards. The “60-40" is a typical grade for commercial quality. The first number (60) represents the scratch grade. The scratch grade is one of the following arbitrary numbers: 10, 20, 40, 60, or 80, where the brightness of scratches increases from 10 to 80. This number

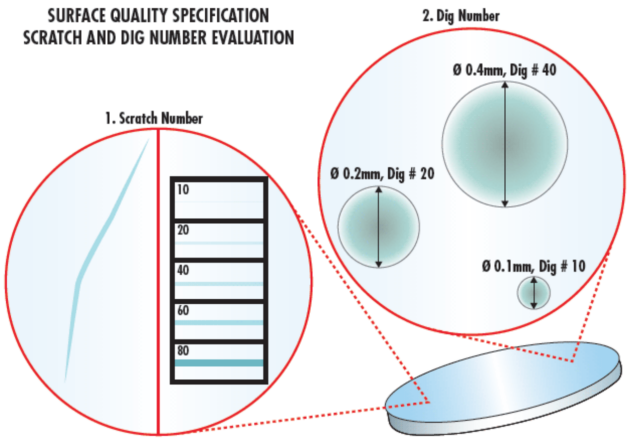

Figure 4.12: Assessment of digs and scratches according to the MIL-0-13830 standard [89].

is not an exact measurement, only an indication of the best match of component scratch brightness with respect to calibrated brightness. The inspection occurs under specified darkfield illumination conditions, but because it is a subjective visual inspection, the results can vary from inspector to inspector. The combined length of the scratches cannot exceed 1/4 of the diameter of the optical component.

The second number (40) corresponds to the dig size (a dig is defined as a pit or small crater on the surface of the glass). This is a measurable quantity and represents the diameter of the largest component dig, given in 1/100 of millimeters. The maximum diameter for any dig is 0.4 mm, corresponding to a dig number of 40. One dig per area with 20 mm diameter is still acceptable. For more digs, the sum of their diameters should not exceed 0.8 mm per area with 20 mm diameter.

Figure 4.12 demonstrates how digs and scratches are identified in a sample, and shows how the comparison with the calibrated standard MIL-0-13830 is performed.

A simple visual inspection on the quartz small coupons and a detailed examination with the microscope has evidenced the good quality of the small coupons, with very little or total absence of scratches. Even though a similar detailed inspection could not be performed on the large plates, evidence of large scratches was reported on some of them, as shown in Fig. 4.13 for plate number 2 (each of the large plates has been numbered in view of the inspection). To ensure a better visualisation of the surface defects, the plate was placed horizontally above a black matte background.

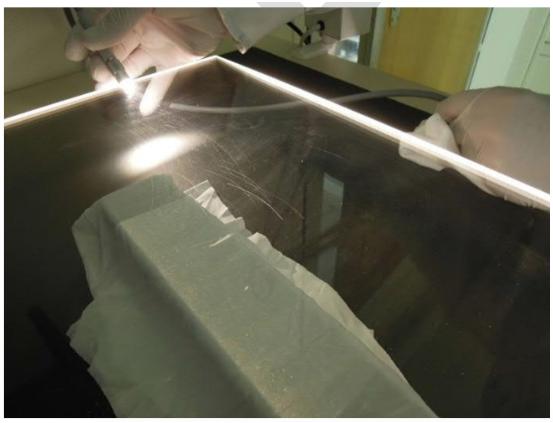

Figure 4.13: Large scratches in quartz plate number 2, observed during the visual inspection at the CERN Optics Laboratory [83].

By illuminating the plate through its side using a light source, light diffuses from the surface and internal imperfections, making the largest defects directly visible by eye. The largest scratches have a width of 10-15 μm and they are probably due to inadequacies in the polishing procedure. Extra polishing on the plate surfaces to remove such scratches would cause a thinning of about 0.3 mm per-side. It was decided that plate 2 could not be accepted.

Concerning the dig grade in the small quartz coupons, no digs or single isolated digs across large portions of surface have been observed. Fig. 4.14 shows the largest dig found (diameter of around 30 μm) within an area of 1.8 mm × 1.3 mm (2.34 mm^2). A 20× zoom of the area is used to better visualise the dig and measure its size. While the majority of the large plates have passed the standard requirements in terms of the dig grade, the visual inspection evidenced further issues in plate number 6. Figure 4.15 (left) represents a portion of the plate, with an area of the same size as that examined for the small quartz coupons shown in Fig. 4.14. A zoom on this area highlights the presence of five large digs with typical diameter of about 20 μm and ten smaller digs, with diameter of about 10 μm. The summed diameters of the digs is $d_{tot} = 0.2$ mm. Assuming the same dig distribution in a circular area with diameter 20 mm (314 mm^2), the sum of the dig components would be $d_{tot} \times (314/2.34) \simeq 27$ mm, which is much larger than the tolerance

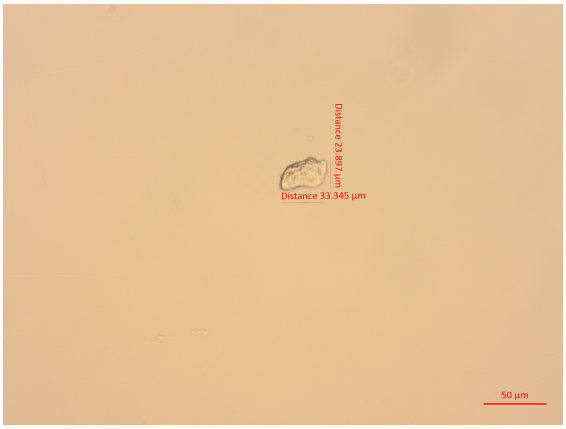

Figure 4.14: Single dig in one of the quartz coupons, visualised at the microscope with a magnification of 20×.

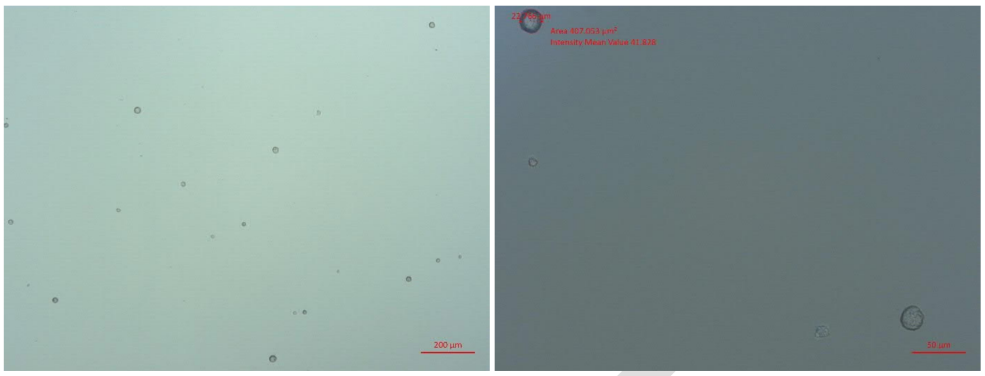

Figure 4.15: Digs in large plate number 6. The examined area is compatible with that shown in Fig. 4.14 for one of the small coupons. Left: digs visualised at the microscope with magnification 5×. Right: digs with magnification 20× [83].

required from the MIL-0-13830 standards. It was therefore decided that plate number 6 could not be accepted.

4.6 Summary

The quality assurance measurements performed on the upgraded RICH1 quartz windows are essential to ensure excellent performance of the detector over the next decade of data-taking. Measurements on the small quartz coupons from the same production batch of the large windows demonstrate that the chosen material, Spectrosil® 2000 from the German company Heraeus, complies with the requirements and actually exceeds the performance expectations. However, a visual inspection on the six large plates which will form the two windows has highlighted the presence

of digs and scratches at the samples' surface, due to inadequacies in the polishing procedure. While these defects are relatively few and isolated in most of the plates and are not expected to alter the performance of the windows, two plates had to be rejected for poorer quality with respect to the others and new ones have been commissioned by Heraeus at the beginning of 2019. As per schedule, the upper quartz window was then installed on the gas enclosure. However, after 24 hours it broke in the region of the central plate. The reasons behind the mechanical failure were investigated but no clear cause was found[1]. It was decided, in consultation with Heraeus, that the window was likely to be unusable since the breaking could result in gas leak (the window separates the photodetector region from the RICH1 radiatior gas). Following the breaking, a new production batch (3 new plates) has been commissioned and new large plates arrived at CERN in between the end of 2019 and 2020, together with new small coupons. The transmission performance of the new coupons has been tested using the methodology described above, and very similar performance was observed.

At the time of writing, the commissioning of the upgraded LHCb detector has entered its final stages. Discussions with the other experiments have confirmed the closure of the LHC caverns in February 2022 in order to be ready for data taking [90]. This timescale is particularly tight for LHCb because of the large scale of the modifications made to the detector, and the impact of Covid19 pandemic-induced restrictions on personnel travelling to CERN for the final installation and commissioning activities.

[1]Same windows with similar mechanics have been used in RICH1 in the first 11 years of detector activity without any issue.

5

Strategy of the W mass measurement

Measurements of the W boson mass are notoriously time consuming and difficult. For example, the CMS experiment is yet to report a measurement of m_W after more than ten years of LHC running. The most important aspect of the measurement is the accurate modelling of the data in simulated events. This requires an excellent control of the detector response and of the muon reconstruction efficiencies, as well as all the understanding of the theoretical predictions of vector bosons production and decay. Concerning the last points, there has been an increasing effort in the theory community over the past years to provide the tools needed to achieve the desired precision, and much improvement is expected for the coming years. Measurements of m_W are often performed with *blinded* analyses, i.e. without looking at the value of m_W until the very final step of the process, called *unblinding*. The blinding procedure, which is completely agnostic to the values of m_W, avoids biases in the choices and strategies adopted in the analysis. For the measurement presented in this thesis, a random generator with a single seed is set to perform the blinding. The blinded m_W value has an offset that is drawn from a uniform random number in the range ± 0.5 GeV. The sign of the shift is also randomised independently. The procedure is carefully set up so that the fit used to extract m_W has access only to the blinded value. Most of the cross-checks and consistency tests of this analysis can be performed before unblinding. Once the analysis procedure is validated, the

value of m_W is unblinded. Given that the models of vector boson production are expected to improve, and a truly blind analysis can only be performed once on a given dataset, it is claimed that it would be unwise to analyse the full LHCb Run 2 dataset at this stage. Instead, a *proof-of-principle* measurement with data collected in the year 2016 is presented. This yields a statistical uncertainty of about 20 MeV. The future measurement with the full Run 2 dataset will benefit from the improvements and the discussions with the particle physics community to try to reduce the overall systematic uncertainty.

5.1 Overview of the analysis

As mention in Chapter 1 hadron-collider experiments like CDF, D0, ATLAS and CMS have access to several m_W-sensitive observables. Since LHCb does not possess the hermetic calorimeter coverage necessary to reconstruct p_T^{miss}, this observable and m_T cannot be used to measure m_W. The measurement relies only on a template fit of the charged lepton p_T distribution. Furthermore, since the LHCb calorimeters are designed for the detection of particles originating from heavy flavour decays, the cells measure transverse energy (E_T) accurately only up to about 10 GeV. As a result, a typical electron from the decay of a W or Z boson will saturate the cell and lead to a wrong energy estimate. Fortunately, LHCb has excellent performance in reconstructing muons, therefore the measurement of m_W will rely only on the muon p_T distribution. Using simulated W decays in LHCb, Fig. 5.1 illustrates how the shape of the muon q/p_T distribution, with q being the muon charge, is influenced by a 300 MeV shift in m_W, which corresponds to roughly ten times the target precision of the present analysis. Unlike previous analyses that were based on the charged lepton p_T, the present work uses the q/p_T distribution because. This provides an simple way to simultaneously analyse the two W charges, and it is graphically convenient since it allows to show the entire high p_T tail in the fit projections, though the fit only includes a restricted window around $p_T \sim m_W/2$, which is the region of the p_T spectrum more sensitive to m_W.

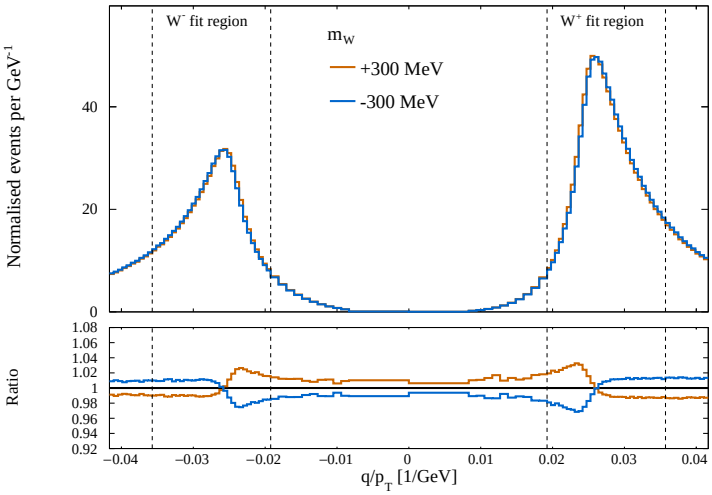

Figure 5.1: Illustration (with LHCb simulated events) of how m_W can be determined from the shape of the muon q/p_T distribution.

The measurement is performed on the 2016 dataset, with the fit model based on fully simulated events. The analysis requires a series of steps which are listed below but will be described in greater detail in the following sections and chapters.

1. Apply a re-alignment to the data, by refitting the reconstructed tracks of the event of interest.

2. Apply LHC fill-dependent momentum scale corrections, to account for drifts in the standard mass resonances used for momentum calibration observed in 2016. The procedure is described in Chapter 7.

3. Apply finer analysis-level curvature bias corrections using the *pseudomass* method. A detailed description will be given in Chapters 6 and 7.

4. Determine momentum smearing (including momentum scale, curvature bias and resolution corrections) parameters within a simplified model and apply the resulting smearing to all of the simulated samples (described in Chapter 7).

5. Determine and apply similar smearing corrections to the track χ^2 (χ^2_{trk}) and impact parameter χ^2 (χ^2_{IP}) distributions so that the efficiencies of the cuts on these variables are better modelled.

6. Determine weight-based corrections for the muon tracking, identification and trigger efficiency.

7. Determine weight-based corrections for the isolation, χ^2 and χ^2_{IP} cut efficiencies.

8. Perform a simultaneous fit to the muon q/p_T distribution of selected $W \to \mu\nu$ candidates and of the ϕ^* distribution in $Z \to \mu\mu$ candidates, as described in Chapter 8.

9. Produce a set of postfit plots of variables that are not used in the fit, to ensure that the modelling of the data in simulated events is correctly implemented.

10. Perform a series of cross-checks to ensure the reliability of the final result. These are particularly important in the pre-unblinding phase of the analysis.

11. Assess the various sources of systematic uncertainty.

The final steps of the analysis such as the fit strategy, the assessment of the systematic uncertainties, the validity checks and the final results are described in Chapter 8.

5.2 Dataset and selection

The analysis primarily relies on seven selections. The first four correspond to $W \to \mu\nu$, $Z \to \mu\mu$, $\Upsilon(1S) \to \mu\mu$ and $J/\psi \to \mu\mu$, which require that decay products are identified as muons. Unless specified, the notation $W \to \mu\nu$ already implies charge conjugation. There are two additional selections for $Z \to \mu\mu$ that are used to study the muon tracking, trigger and identification efficiencies. The final selection mimics the $W \to \mu\nu$ but makes no muon identification requirement: this is primarily used to train and validate the hadron decay background model. Different cuts are applied for each of these selections. Tables 5.1 and 5.2 report those for the W and Z selections. After these requirements, roughly 2.5×10^6 $W \to \mu\nu$ candidates and 2×10^5 $Z \to \mu\mu$ candidates are included in the m_W fit.

Table 5.1: The W selection cuts used in the analysis.

Description	Cut
Z veto	second muon with $2.0 < \eta < 4.5$, p_T $< 25\,\text{GeV}$
Momentum error	$\sigma(P)/P < 0.06$
Sanity check	$P < 2000\,\text{GeV}$
Trigger	Passes `L0MuonEW`, `HLT1` and `HLT2`
Pseudorapidity	$2.2 < \eta < 4.4$
Hits in TT	TTClusters>0
Impact Parameter quality	$\chi^2_{\text{IP}}/\text{ndf}$ <9
Track quality	$\chi^2_{\text{trk}}/\text{ndf} < 1.8$
Energy deposit in HCAL	$E_T^{\text{HCAL}}/\text{GeV}$<5
Isolation	$\mathcal{I}^{\text{PF},0.4}/\text{GeV}$<4

Table 5.2: The Z selection cuts used in the analysis.

Description	Cut
Mass	$91 - 14 < M/\text{GeV} < 91 + 14$
Transverse momentum	Both muons with $p_T > 20\,\text{GeV}$
Sanity check	Both muons with $P < 2000\,\text{GeV}$
Trigger	Either muon passes `L0MuonEW`, `HLT1` and `HLT2`
Pseudorapidity	Both muons with $1.7 < \eta < 5$
Isolation	Both muons with $\mathcal{I}^{\text{PF},0.4}/\text{GeV}$<10
Energy deposit in HCAL	Both muons with $E_T^{\text{HCAL}}/\text{GeV}$<10
Impact Parameter quality	Both muons with $\chi^2_{\text{IP}} < 100$
Track quality	Both muons with $\chi^2_{\text{trk}}/\text{ndf} < 3$

The motives for the most important cuts on the $W \to \mu\nu$ sample are explained below. The isolation (denoted as $\mathcal{I}^{PF,0.4}$) is defined as the sum of the transverse momenta of all of the particles detected in a cone around the identified muon track with aperture given by $\Delta\eta^2 + \Delta\phi^2 = 0.4^2$, where $\Delta\eta$ and $\Delta\phi$ denote the separation in pseudorapidity (η) and azimuthal angle around the beam direction (ϕ), respectively. In order to suppress the hadron decay background, a tight cut of 4 GeV on the isolation is applied. A relatively tight window on the muon η avoids the edges of the detector where the isolation cone is not completely instrumented.

The alignment and the detector response model are also less reliable at the edges of the detector. It is anticipated that the analysis with the full Run 2 dataset aims at increasing this pseudorapidity window. A veto on events with a second muon with $p_T > 25\,\text{GeV}$ is included. A maximum impact parameter significance requirement suppresses $W \to \tau\nu$ (with subsequent $\tau \to \mu\nu$ decay) and heavy flavour decays, for which the muon originates from secondary vertices rather than the primary vertex.

The $Z \to \mu\mu$ candidates are selected with looser cuts, though in the m_W fit (detailed later) there is a requirement that at least one muon satisfies all of the requirements from the W selection. This is done to better constrain the background fractions in the $W \to \mu\nu$ fit model, which are determined with respect to the $Z \to \mu\mu$ yield. The selection criteria for $\Upsilon(1S)$ and J/ψ, which are used to determine the momentum smearing parameters and trigger efficiencies, are typical of many LHCb analyses. These are reported in Appendix A.

5.3 Signal modelling

The adopted approach consists of setting up a fit model based on parton shower Monte Carlo events with a detailed, GEANT4 [76] based, detector simulation. However, the Monte Carlo events need to be corrected for simulation inaccuracies in the detector response and in the physics modelling. The modelling of the W boson transverse momentum (p_T^W) in particular, which strongly affects that of the muon p_T, is one of the most challenging aspects of the m_W measurement. One possible approach is to study the Z boson transverse momentum and use its measurement to constrain and deduce p_T^W. As explained in Chapter 1, at leading order (LO) approximation, Z bosons in Drell Yan events are produced without transverse momentum ($p_T^Z = 0$). However, Z bosons are found to have $p_T^Z \neq 0$. The low p_T^Z region is governed by the intrinsic transverse momentum of the partons within the proton rest frame (k_T^{intr}), and the emission of radiation of quarks and gluons from the initial-state partons. For this effect, large logarithmic terms must be resummed to achieve an accurate prediction. This can be done by either using analytic resummation techniques [91, 92] or using parton-shower algorithms. As will

be shown in the following section, the measured p_T^Z distributions can be compared to several theoretical predictions provided by Monte Carlo generators. The generators contain "tuning parameters" which are not constrained by the theory but can be varied to match the measured distributions. A very debated question within the theory and experimental community is whether the parameters that "tune" the p_T^Z distribution are also reliable in describing the measured p_T^W distribution. The analysis presented in this thesis provides separate tunes of W and Z production. In fact, Ref. [58] shows that it possible to simultaneously fit m_W and determine QCD-related nuisance parameters that mostly affect p_T^W, such as the parton shower α_s and the intrinsic transverse momentum of the partons contributing in the process (k_T^{intr}). Figure 5.2 shows variations of the W^+ transverse momentum spectrum in simulated events, corresponding to arbitrary variations of the generator's (in this case Pythia) α_s (left) and k_T^{intr} (right) nuisance parameters. Variations of α_s affect the bulk of the p_T^W spectrum, whereas variations of k_T^{intr} mainly affect the low-p_T^W region.

Focusing on the *decay* part of the Drell-Yan cross section, the angular coefficients for Z production have been computed to $\mathcal{O}(\alpha_s^3)$ [93] but there are no such predictions for W production. Furthermore, the $\mathcal{O}(\alpha_s^3)$ are not yet usable but there are several $\mathcal{O}(\alpha_s^2)$ predictions with public tools, such as DYTurbo [94].

No single program is able to adequately describe all five degrees of freedom in the Drell Yan cross section, as described by Eq. 1.17. However, its factorisation into unpolarised cross section and angular coefficients can be exploited to use different Monte Carlo generators to better predict the two independent factors. The model in this analysis uses the program POWHEGBoxV2 [47] interfaced to Pythia [49] (here abbreviated as POWHEGPythia) for the unpolarised cross section, and DYTurbo at $\mathcal{O}(\alpha_s^2)$ for the angular coefficients. Many different fit model variations are being tested and considered in the evalutation of the systematic uncertainties. It is important to remember that all of these predictions depend on the choice of the Parton Distribution Functions. The baseline model uses the `NNPDF31_nlo_as_0118` PDF set, where the PDFs are calculated assuming $\alpha_s = 0.118$. Variations of the

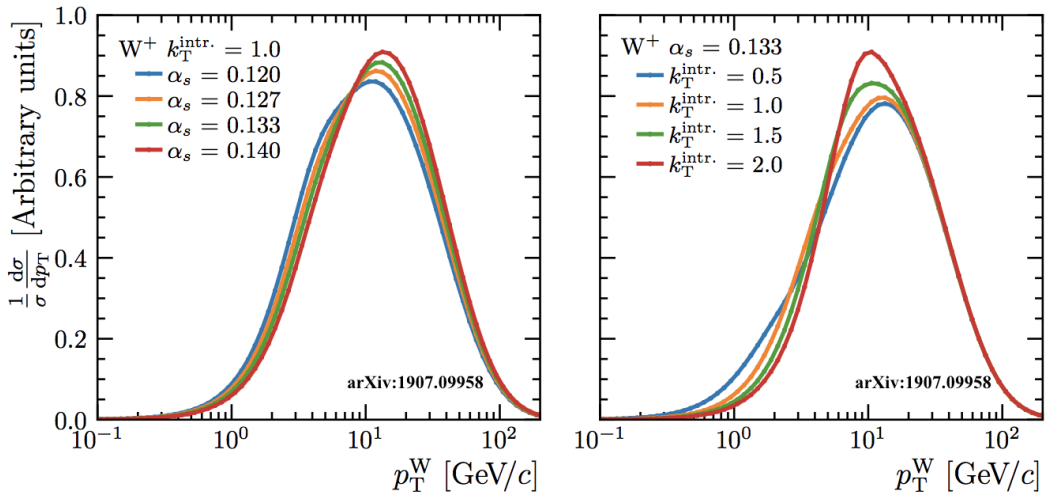

Figure 5.2: Variations of the W^+ transverse momentum spectrum in simulated events, corresponding to arbitrary variations of the generator's (PYTHIA) α_s (left) and k_T^{intr} (right) nuisance parameters.

PDF set and of the values of α_s are considered in the systematic uncertainties and will be described in Chapter 8.

5.3.1 Physics modelling

In order to adjust the fit model, each generated event is assigned the product of a series of weights.

Mass weight The W resonance is assumed to follow a relativistic Breit-Wigner function with a mass-dependent width ($f(M)$), as shown by Eq. 2.1. A different W mass hypothesis (m_W^{hypot}) can be emulated by assigning a weight to each event,

$$w_{\text{mass}}(M, m_W^{\text{hypot}}) = \frac{f(M, m_W^{\text{hypot}}, \Gamma_W^{\text{Pythia}})}{f(M, m_W^{\text{Pythia}}, \Gamma_W^{\text{Pythia}})} \tag{5.1}$$

where $m_W^{\text{Pythia}} = 80.385$ GeV and $\Gamma_W^{\text{Pythia}} = 2.085$ GeV are the W mass and width, respectively, used as default by PYTHIA in event generation in the LHCb simulation.

Unpolarised cross section weight Three-dimensional histograms of the mass (M), rapidity (y) and p_T of the vector boson intermediate state are populated

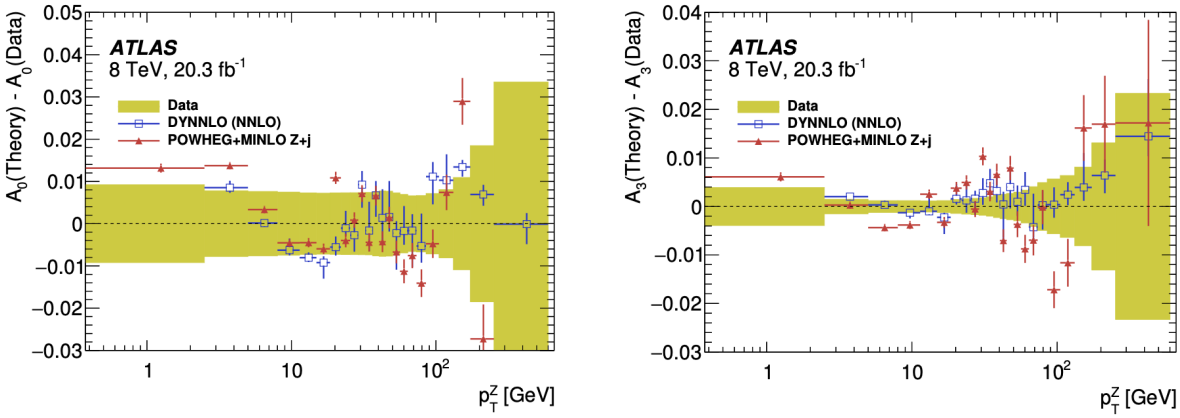

Figure 5.3: The difference between the angular coefficients A_0 (left) and A_3 (right) measured as a function of p_T^Z by the ATLAS collaboration and their predictions from DYNNLO [95] and POWHEGMiNLO [97].

with events simulated with different α_s and k_T^{intr} values. The ratio of the target $d^3\sigma/dydMdp_T$ to the LHCb Pythia tune defines the value of w_{xsec}:

$$w_{\text{xsec}} = \frac{\frac{1}{\sigma_{\text{target}}}\frac{d^3\sigma}{dMdp_Tdy}(\alpha_s, k_T)\Big|_{\text{target}}}{\frac{1}{\sigma_{\text{Pythia}}}\frac{d^3\sigma}{dMdp_Tdy}\Big|_{\text{PythiaLHCb}}} \tag{5.2}$$

Angular weight The ATLAS collaboration has reported an extensive measurement of the Drell-Yan angular coefficients in $pp \to Z \to \mu\mu$ at $\sqrt{s} = 8$ TeV [95]. Their data are reasonably well described by $\mathcal{O}(\alpha_s^2)$ predictions from the DYNNLO [96] program, on which DYTurbo is based. Figure 5.3 shows the difference between the angular coefficients A_0 (left) and A_3 (right) measured as a function of p_T^Z by the ATLAS collaboration and their predictions from DYNNLO. Data and prediction tend to agree within a fraction of percent across the entire p_T^Z range, except for A_3 in the highest momentum region, where the agreement is within a few percent. It is worth noting that, at the time of writing, no measurement of the Drell-Yan angular coefficients has been published by the LHCb experiment.

During the development of the analysis presented in this thesis, it was concluded that DYTurbo is the only program that predicts the angular coefficients with sufficient reliability. With a procedure similar to that of the unpolarised cross section, the angular weight is obtained with the ratio between the DYTurbo

predictions and the LHCb PYTHIA tune, following Eq. 1.17:

$$w_{\text{ang}} = \frac{1 + \cos^2\theta^* + \frac{1}{2}A_0^{\text{DYTurbo}}(1 - 3\cos^2\theta^*) + ... + A_4^{\text{DYTurbo}}\cos\theta^*}{1 + \cos^2\theta^* + \frac{1}{2}A_0^{\text{PythiaLHCb}}(1 - 3\cos^2\theta^*) + ... + A_4^{\text{PythiaLHCb}}\cos\theta^*}. \quad (5.3)$$

The DYTURBO predictions for the angular coefficients are given at several factorisation and renormalisation *scales*. Several variations in these scales are considered following the prescriptions of Ref. [93], and the scale uncertainty on the angular coefficients is taken as the envelope of the resulting shifts in m_W. In the development of this analysis it was observed that the scale uncertainty in the angular coefficient was a limiting factor (roughly 20-30 MeV of systematic uncertainty). However, the fit χ^2 is also sensitive to such scale variations. Figure 5.4 shows the variation in the muon q/p_T distribution of $W \to \mu\nu$ events when a 3% scale factor is applied to the first five angular coefficients. It should be noted that the relative uncertainty on the angular coefficients is at the 10% level, so the variation illustrated in the plot is sensible. The plot shows that the largest variation in the p_T shape, and thus the largest sensitivity of m_W to the scale choices, is primarily via the A_3 coefficient. This can be explained by the fact that the shape of the muon p_T distribution can be approximately described by

$$p_T \approx \frac{m_W}{2}\sin\theta^* + p_T^W\cos\phi^*, \quad (5.4)$$

which follows the same angular dependency of the A_3 term in Eq. 1.17. It should be also noted that, by definition of the Collins Soper frame, for the μ^+ the two angular terms are coherent in sign, while for the μ^- they have opposite sign. This explains the large difference between the A_3 scale variation for the two muon charges in Fig. 5.4. In order to account to the large sensitivity of m_W to the A_3 scaling, the reweighting procedure contains an additional parameter, which can be included in the minimisation in the fitter, that scales the A_3 coefficient independently of the vector boson p_T, y and M. With a single (shared between W^+ and W^-) scaling parameter there is only a small degradation in the statistical uncertainty on m_W but the width of the envelope of m_W values corresponding to the various DYTURBO scale choices is reduced by more than a factor of two. With

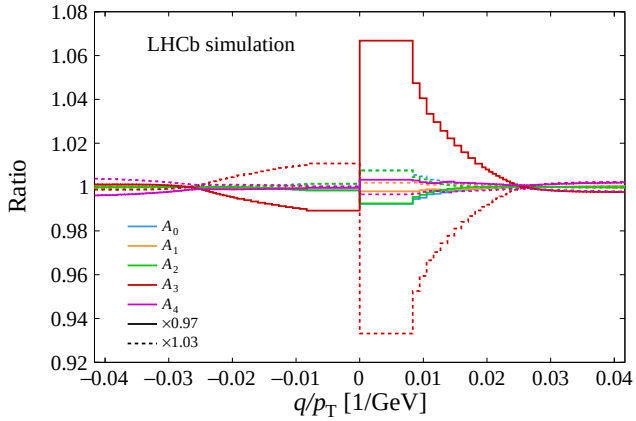

Figure 5.4: The variation in the muon q/p_T distribution of simulated $W \to \mu\nu$ events when a 3% scale factor is applied to the first five angular coefficients. The coefficients from A_5 to A_7 are zero up to $\mathcal{O}(\alpha_s^2)$ and therefore are not included.

this treatment the modelling relies on DYTurbo for the *kinematic dependence* of A_3 but not on its scale dependence. For the other angular coefficients the modelling relies entirely on the program's predictions.

A simplified version of the mass fit used to extract m_W, which will be discussed later, is used to evaluate the accuracy of several Monte Carlo generators in predicting the vector boson p_T^Z distribution, assuming the angular coefficients description given by DYTurbo. The simplified fit takes only Z events, with no simulated background. The starting parameters of the fit are set to the defaults of the models considered (e.g. $\alpha_s = 0.118$ for POWHEGPythia), rather than values that are closer to preference of the data. In this way, what is denoted as the *prefit* scenario coincides with the out-of-the-box prediction of the program.

The upper plots in Fig. 5.5 show the results of the fit to p_T^Z for several Monte Carlo generators. The fit region extends up to $p_T^Z < 30\,\text{GeV}$. The lower plots show the corresponding ratios with respect to the prediction from POWHEGPythia. Several other programs of the same type (i.e. programs that predict the hard process at NLO in perturbative QCD and are interfaced with a parton shower generator) have been studied. These programs consistently predict a p_T^Z distribution that is too soft. The best agreement with the data is obtained with POWHEGPythia, with a preferred α_s value of around 0.124 (right hand side plot of Fig. 5.5). DYTurbo

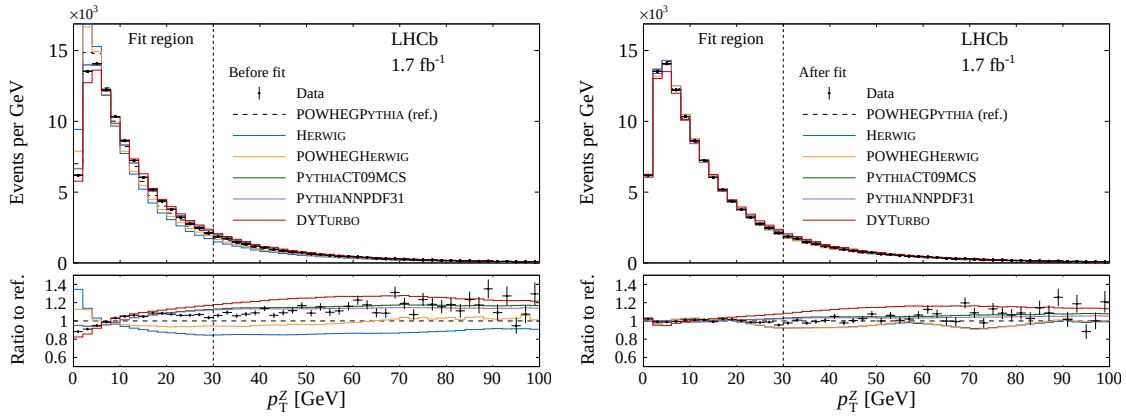

Figure 5.5: The p_T^Z distribution compared before (left) and after (right) the fit for different candidate models of the unpolarised cross-sections. The fit only considers the region $p_T^Z < 30\,\text{GeV}$ which is indicated by the dashed vertical line. In the lower panels the ratios are with respect to the POWHEGPYTHIA model.

predicts the region $p_T^Z < 30\,\text{GeV}$ reasonably well, but its prediction of the high p_T region is too hard. The following alternatives are considered for the systematic uncertainty in the shape of the vector boson p_T distribution:

1. PYTHIA with the `CT09MCS` PDF set.
2. PYTHIA with the `NNPDF31` PDF set.
3. HERWIGNLO with the `NNPDF31` PDF set.
4. POWHEGHERWIG with the `NNPDF31` PDF set.

Figure 5.5 shows that POWHEGPYTHIA describes the p_T^Z data better than other programs. However, it is important to verify if the proposed fit strategy can reliably determine m_W if the production of W and Z bosons is better described by one of the other models. For this purpose, a set of *challenge* toy datasets have been prepared using events simulated with the LHCb PYTHIA tune without detector simulation and reweighted to the default POWHEGPYTHIA and DYTURBO model. The simulated events that serve as "data" in the challenges are reweighted to match an alternative model. No background contribution is included in the modelling. The results of these toy data challenges show that the fit method is able to absorb the differences between the various models in the QCD nuisance

parameters, while the value of m_W extracted from each challenge dataset differs from the default model by no more than 10 MeV.

5.3.2 QED Final state radiation

The reweighting procedure used in the modelling described so far is based on the kinematics of the leptons at the Born level to account for differences in the production model between different generators. This procedure does not take into account differences in the description of QED final state radiation, which is applied to the Born level muons to produce what are referred to as *Bare* muons. In order to investigate the effect of the description of the final state radiation models, a separate study is performed by reweighting the difference in energy between the dilepton system before and after the implementation of final state radiation, at the Born and Bare levels respectively, to match different models. These studies are described in more details in [98], and include PYTHIA, HERWIG [99], PHOTOS [74], DIRE [100] and VINCIA [101]. The generators differ in the choice of how the parton shower, and its evolution, is modelled. Of all the generators studied, DIRE and VINCIA are not currently widely used for FSR studies in precision electroweak measurements. Since no generator among PYTHIA, HERWIG and PHOTOS is preferred, a weight taken as the average of the results with the three generators is applied to the simulated sample. The maximum difference between the three generators and the central value is taken to be the systematic uncertainty due to the final state radiation modelling.

5.3.3 Muon reconstruction efficiencies

In order to reduce backgrounds coming from spurious tracks and real muons from hadron decays, a series of requirements is imposed on quantities related to the reconstruction of the signal muon(s). These include requiring that the muons are reconstructed as long tracks, have positive muon identification and pass typical trigger requirements for high p_T muons. Since simulated signal samples are used to fit the muon p_T spectrum in data, it is crucial that any mis-modelling of these quantities in the LHCb simulation is taken into account. Any residual mis-modelling

of data in simulated events will lead to a poor fit quality and an erroneous extraction of m_W. The total muon reconstruction efficiency is factorised into trigger, tracking and muon identification efficiencies.

In this analysis, muon reconstruction efficiencies in data and MC are calculated using a *tag-and-probe* method on $Z \to \mu\mu$ and $\Upsilon(1S) \to \mu\mu$ candidates. For the trigger efficiency, for example, one *tag* muon is required to pass the trigger selection while the other muon can be used as a *probe* of the trigger efficiency. A matching event is found depending on whether the probe muon is matched to a positive trigger decision in the event data record. The efficiencies are then calculated by simply counting the matched and unmatched events with invariant masses within ± 15 MeV of the nominal Z mass. In order to accurately determine corrections for the low p_T portion of the m_W fit range, a $\Upsilon(1S) \to \mu\mu$ tag-and-probe sample is used. Trigger efficiencies in data and simulation (ϵ^{D} and ϵ^{MC}, respectively) are determined as a function of the muon η, ϕ and p_T. A parametric fit to $\epsilon^{\mathrm{D}}/\epsilon^{\mathrm{MC}}$ and ϵ^{MC} as a function of $1/p_T$ in bins of the muon η and ϕ is performed. Different choices of binning and parameterisation are evaluated in the assessment of the systematic uncertainties. The muon identification efficiency is treated similarly to the trigger efficiency except that $\Upsilon(1S) \to \mu\mu$ events are not used. The tracking efficiency is measured using $Z \to \mu\mu$ candidates in which the probe muon is reconstructed by combining hits from the muon stations and the Trigger Tracker (TT) upstream of the magnet. Since the probe track is reconstructed without using hits in the VELO and the three tracking stations downstream of the magnet, this method allows to probe the reconstruction performance for these sub-detectors. The fraction of probes with a matching track in the LHCb tracking algorithm determines the efficiency. Trigger, identification and tracking scale factors are derived and applied as weights to each event in the signal templates based on its muon's kinematics, correcting the overall shape of the templates for any muon reconstruction mis-modelling. It is important to mention that these efficiencies are derived *after* the detector alignment corrections to the data and the muon momentum calibration in the simulation. This order of operation reduces the size of the *residual* corrections to

be applied to the simulation via the efficiencies determination. These steps will be described in greater detail in Chapter 7.

5.3.4 Isolation, impact parameter and track quality cut efficiency modelling

During the development of this analysis, it was observed that the tight isolation requirement applied to the $W \to \mu\nu$ candidates leads to larger inefficiencies than the other applied cuts. Therefore, it has to be accurately modelled in the simulation. The efficiency of the isolation cut is measured with a simple counting method in data and simulation. Two-dimensional maps of the efficiency ratio in data and MC in bins of the muon kinematics are generated and used to derive a *weight* that is assigned to each simulated event in the template fit to extract m_W. The modelling of the impact parameter and track fit χ^2 variables in simulation is performed using $Z \to \mu\mu$ events and consists of two stages. First, the three-dimensional impact parameter is decomposed into its individual components which are smeared to match the data according to a normal distribution in six bins in η and seven bins in ϕ. In each bin the mean and width of this smearing function are determined by a minimisation procedure [102].

A similar procedure is used to improve the modelling of the track fit χ^2 distribution. Smaller (a few permille of unity) weight-based corrections are then applied to account for the efficiencies of the impact parameter and track χ^2 requirements.

5.3.5 Polarity weighting

In addition to the weights that correct for physics and detector differences one further weight factor, which has not yet been described, is included in all template events. This is to reweight all components to have the same ratio of events in the two magnet polarities as in the real data.

5.4 Background modelling

Contributions to the background arise from $W \to \tau\nu$ decays with the τ decaying into a muon and a neutrino, $Z \to \mu\mu$ decays where only one of the two muons is reconstructed, and $Z \to \tau\tau$ decays. Other contributions include heavy flavour decays ($c\bar{c}$, $b\bar{b}$), $q\bar{q}\,(g\bar{g}) \to t\bar{t}$ and single-top production (tW). All these components are modelled using LHCb fully simulated events.

An additional contribution arising from in-flight decays of pions and kaons into muons is present in the sample of W boson candidates. A data-driven approach is used to model this source of background in the fit. A sample of events is obtained by applying the W boson selection requirements listed in Table 5.1, but with the muon identification requirement being inverted. This selection, denoted as `NoMuID`[1] is characterised by candidates with $p_T > 15\,\text{GeV}$, $p > 8\,\text{GeV}$ and $\chi^2_{\text{trk}}/\text{ndf} < 4$. Further cuts are applied to the event sample to minimise the contamination of potential signal candidates. Alternative selections have been studied and evaluated in the assessment of the systematic uncertainties to the background model. The p_T spectrum of the selected candidates is parameterised with the Hagedorn function [103], with an exponential component for ghost tracks (i.e. reconstructed tracks that are not associated with any particle or physics process). Since the QCD background candidates in the signal sample are predominantly composed by muons from decays-in-flight, the candidates are weighted according to the probability of an unstable hadron of mass m, lifetime τ, and momentum p to decay within a detector of length d:

$$1 - \exp\left\{ -\frac{md}{\tau p} \right\} \approx \frac{md}{\tau p}. \tag{5.5}$$

Events are split in different regions of χ^2_{IP} and isolation in order to study the variation of the p_T spectrum for candidates from different background sources. Particles with lower χ^2_{IP} and $\mathcal{I}^{\text{PF},0.4}$ are more representative of the QCD background affecting the $W \to \mu\nu$ fit component, since they correspond to isolated hadrons from prompt decays. The parameterisation obtained from this fit is used to

[1]It should be noted that this selection is available in the LHCb *stripping* only from 2017 onwards. However, the data taking conditions were similar between 2016 and 2017, therefore the present analysis uses the 2017 sample.

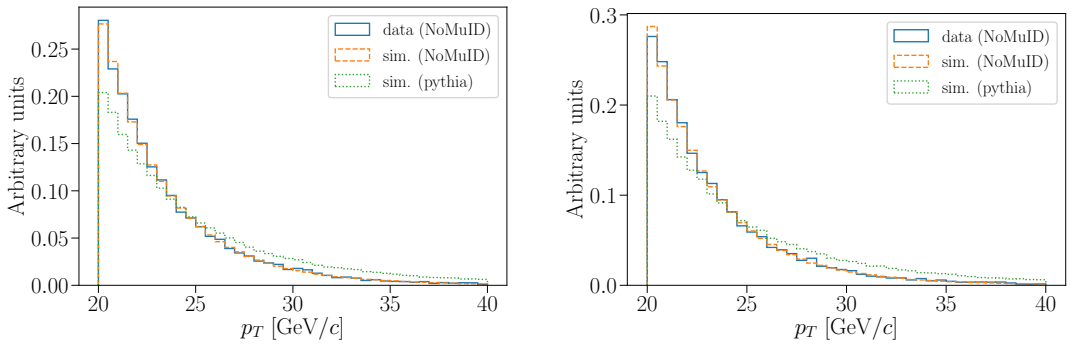

Figure 5.6: The p_T distribution for (blue) data candidates, (dashed orange) candidates simulated from the Hagedorn [103] parametric model and (dotted green) Pythia simulated candidates for (left) positive and (right) negative charges. The disagreement observed between data and Pythia simulated candidates suggests the use of a data-driven approach to parametrise the QCD background.

generate a background template sufficiently large (around 10^9 events) for the measurement of m_W. Positively and negatively charged candidates are generated following the W production charge asymmetry at the LHC, and the same number of candidates are generated for both magnet polarities. Figure 5.6 shows the p_T distribution for (blue) data candidates, (dashed orange) candidates simulated from the derived parametric model and (dotted green) Pythia simulated candidates for (left) positive and (right) negative charges. The disagreement observed between data and Pythia simulated candidates motivates the use of a data-driven approach to parametrise the QCD background.

5.5 Summary

This chapter has introduced the methodologies implemented to build the template fit used to extract m_W. The fit strategy and the results will be described in Chapter 8. Particular attention has been given to the theoretical aspects of the modelling of the muon q/p_T distribution. The experimental challenges of the modelling, i.e. the control of the detector alignment and the muon momentum calibration in the simulation, will be described in greater detail in the following two chapters.

6

Determine curvature biases with the "pseudomass method"

6.1 Motivations

If poorly modelled, detector mis-alignment effects can alter the measurement of muon momenta, and bias the determination of m_W and other electroweak observables such as the weak mixing angle ($\sin^2\theta^{\rm eff}_{\rm lept}$). The focus of this chapter will be the determination of curvature biases of the type

$$\frac{q}{p} \to \frac{q}{p} + \delta, \tag{6.1}$$

affecting particles of charge q and momentum p. In the LHCb geometry this would correspond to a displacement along the bending direction (x) of the detector before the magnet with respect to the detector after the magnet.

It is desirable to identify and eliminate these biases (δ) from both the real and simulated data, so that the simulation can be tuned and validated with better reliability. Ref. [104] introduces a method to determine curvature biases that relies on the fact that the mean $1/p_T$ of the μ^+ and μ^- should follow the expectation of simulation, where p_T is the momentum of the muon transverse to the beam axis. The reliance on simulation arises because the p_T distributions are sensitive to both mis-alignment *and* physics effects (including intrinsic differences between

the μ^+ and μ^- kinematic distributions in Z decays, as will be explained in the following sections). Nevertheless, that method has been successfully applied in measurements of $\sin^2\theta^{\rm eff}_{\rm lept}$ by CDF [105] and CMS [106].

This chapter proposes an alternative data-driven approach to determine curvature bias corrections using $Z \to \mu\mu$ decays which is less sensitive to physics effects than other methods present in literature. The method is validated with the example of the LHCb experiment using a simplified model of the detector geometry and mis-alignment configurations. The author's work presented in this chapter has been published in Ref. [107].

6.2 The simulated event sample

A sample of 10^8 $pp \to Z \to \mu\mu$ events, at a centre-of-mass-energy of 13 TeV, is generated with POWHEGBox[47, 108]. These events are subsequently processed with Pythia [49] to simulate a QCD parton shower. Other types of momentum reconstruction bias will not be considered in this study, which is focused instead on systematic curvature biases, but will be evaluated in the measurement of m_W with real data in Chapter 7. Since this work is conducted in the context of precision measurements of electroweak observables with LHCb, events are selected with both muons in the pseudorapidity interval $1.7 < \eta < 5$. It is also required that both muons have $p_T > 15\,\text{GeV}$ and that at least one of the two muons has $p_T > 25\,\text{GeV}$. This selection roughly mimics the selection of Z candidates applied to the real data analysis described in Chapter 5. The coordinates system is defined consistently with that of the LHCb detector, described in Chapter 3. Charged particles are deflected along the x axis by $p^{-1} \times 3$ GeV m, which roughly corresponds to the bending power of the LHCb spectrometer [7]. A curvature bias (δ) can be interpreted as a systematic translation of the measurement plane after the LHCb dipole magnet along the x axis [7]:

$$\Delta x = \delta \times 3\,\text{GeV m}, \tag{6.2}$$

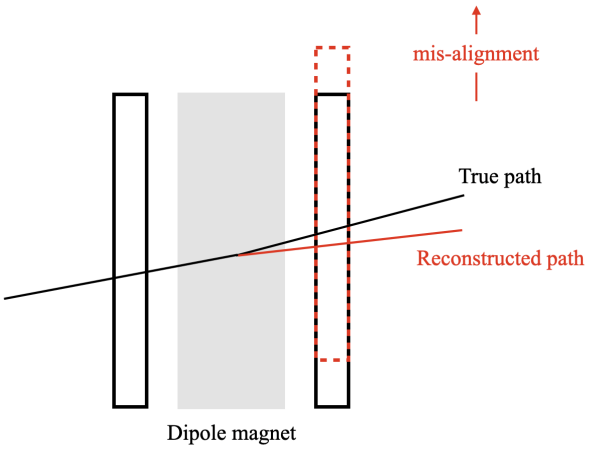

Figure 6.1: A global mis-alignment along x in a simplified configuration of the LHCb detector, with only one measurement plane after the dipole magnet. The effect of the mis-alignment on the reconstructed tracks is shown.

and the effect of such translation on the reconstructed tracks is shown in Fig. 6.1. It should be noted that this study considers a simplified geometry of the LHCb detector, with only one measurement plane after the dipole magnet. In Section 6.6 it is estimated that a Δx value of 5 µm leads to a bias of $\mathcal{O}(50)$ MeV in the determination of m_W for a single charge. It should be noted that the bias in the measurement of m_W for a single charge is strongly (but not fully) anti-correlated to the corresponding bias in m_W for the opposite charge, leading to partial cancellations when the combination of the two charges is considered. Nevertheless, the precision of the measurement is potentially affected by such biases. Given that the LHCb Run 2 dataset allows to measure m_W with an $\mathcal{O}(10)$ MeV statistical precision [44] a simple and reliable method to control this source of bias is necessary.

6.3 The pseudomass method

The proposed method relies on an approximation of the invariant mass of $Z \to \mu\mu$ decays using the momentum of one muon and only the *direction* of the other. In the context of a measurement of the differential cross section for $p\bar{p} \to Z \to \mu\mu$ with the D0 experiment [109], the *pseudomass*[1] variable ($M^{\pm}$) for each muon

[1]The definition of "pseudomass" in D0 is given in terms of leading/sub-leading muons (e.g. muons with the highest/lowest p_T), not positively/negatively charged muons. Furthermore, the

charge was introduced as:

$$M^{\pm} = \sqrt{2p^{\pm}p_T^{\pm}\frac{p^{\mp}}{p_T^{\mp}}(1-\cos\theta)}, \tag{6.3}$$

where $p^{\pm}$ and $p_T^{\pm}$ are the momenta and transverse momenta of the $\mu^{\pm}$ and θ is the opening angle between the two muons. Figure 6.2 shows how these angles are defined in the transverse plane to the beam direction. The pseudomass is an estimate of the dimuon mass under the assumption that the dimuon system has zero momentum transverse to the bisector of the two lepton transverse momenta. Figure 6.2 refers to this axis as $a_{\perp}$. This assumption is reinforced by the fact that most of the $Z \to \mu\mu$ events at hadron colliders are in the region $p_T^Z < m_Z$. A subset of events with smaller p_T^Z values can be selected, independently of the muon momenta, using the ϕ^* variable [110], defined as:

$$\phi^* \equiv \tan\phi_{\text{acop}}/2 \sin\theta_{\eta}^* \approx \frac{p_T^Z}{m_Z}, \tag{6.4}$$

where $\phi_{\text{acop}} = (\pi - \Delta\phi)$ and $\Delta\phi$ is the azimuthal opening angle between the two leptons and $\cos\theta_{\eta}^* \equiv \tanh\left(\frac{\eta^- - \eta^+}{2}\right)$, and where η^- and η^+ are the pseudorapidities of the negatively and positively charged leptons, respectively. It should be noted that the ϕ^* variable defined here is different from the one used in Chapter 1 to define the Collins Soper frame. The chosen requirement of $\phi^* < 0.05$ corresponds to selecting roughly half of the available events. Figure 6.3 (left) shows how this requirement selects events with smaller p_T^Z on average, while Fig. 6.3 (right) shows that the pseudomass distribution of these events has a narrow width of $\mathcal{O}(5)$ GeV.

pseudomass was used for different purposes, and not for addressing curvature biases.

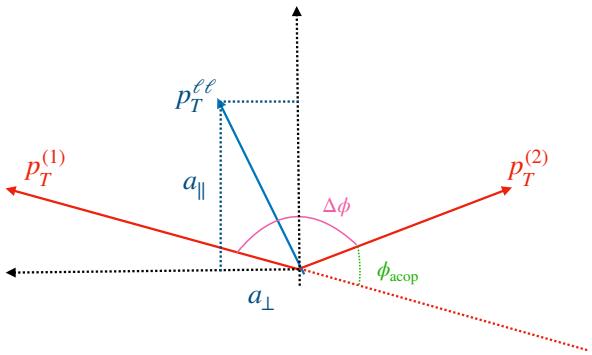

Figure 6.2: The representation of the angles between the two muon momenta in the transverse plane to the beam direction. These angles define the variable ϕ^*.

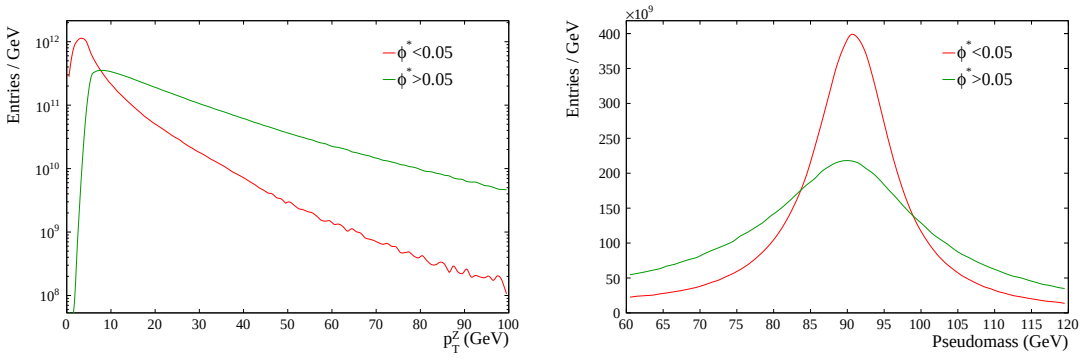

Figure 6.3: The distribution of p_T^Z (left) and the pseudomass (right) for events passing and failing the $\phi^* < 0.05$ cut.

Figure 6.4 shows that the peaks of the M^+ and M^- distributions are displaced by around 2 GeV when $\Delta x = 50\,\mu\text{m}$ is assumed in the simulation. This sensitivity can be exploited to determine the δ in Eq. 6.1 through a simultaneous likelihood fit of the M^+ and M^- distributions. Both distributions are modelled by a double Crystal Ball (CB) function [111], with an exponential function for the non-peaking component of the Z/γ^* line-shape. The mean of the CB function for the $M^\pm$ distribution is defined as $\bar{M}(1 \pm A)$, where $\bar{M}$ and the asymmetry A are 2 of the 16 floating parameters of the fit. The other floating parameters are the width of the first CB function and the relative width of the second CB (for both M^+ and M^-); the α, n parameters describing the tail of the CB; the slope of the exponential component, and the normalisation constants of the three shape functions. The

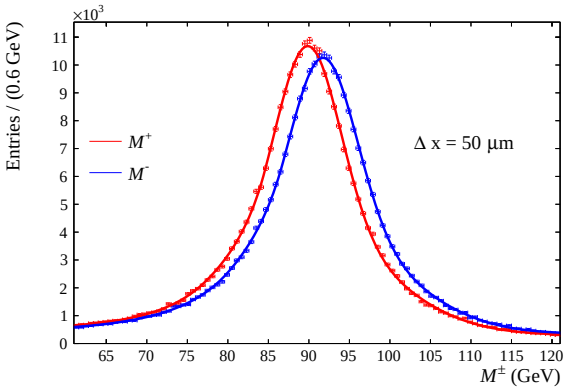

Figure 6.4: The parametric fit of the M^+ and M^- pseudomass distributions, in the presence of a $\Delta x = 50\,\mu\text{m}$. The signal is modelled with a double Crystal Ball function, while the non-peaking component of the Z/γ^* line-shape is modelled with an exponential.

curvature bias can be determined via

$$\delta \approx A\frac{< \frac{1}{p^+} > + < \frac{1}{p^-} >}{2}. \tag{6.5}$$

Since this approach decouples the effect of curvature biases on the momenta of the μ^+ and μ^-, it is possible to determine the values of δ in an arbitrary number of bins of the muon η and ϕ. Unless otherwise specified a binning scheme with 8 (12) η (ϕ) bins is used, with the curvature biases being determined independently in each bin.

It is anticipated that the determination of the δ values with Eq. 6.5 will be slightly biased by the forward-backward asymmetry (A_{FB}) in the $Z \to \mu\mu$ process, which implies a small difference in the kinematic distributions of the μ^+ and μ^-. However, Eq. 6.5 relies on the asymmetry between the pseudomass peak positions and A_{FB} is minimal for dimuon masses close to the peak of the Z resonance. The effect of this bias is nevertheless evaluated and addressed in the following section.

6.4 Validation of the method

The pseudomass method is validated with 30 toy experiments using statistically independent subsets of the $Z \to \mu\mu$ event sample described in Section 6.2. If no mis-alignment is simulated the method should return Δx values that are statistically compatible with zero.

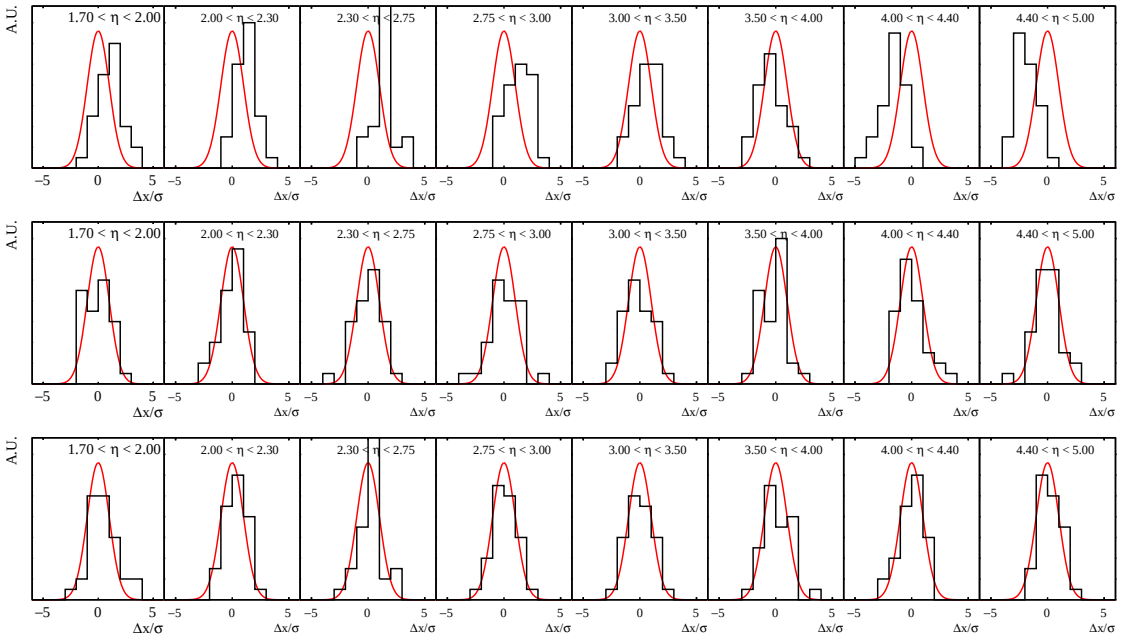

Figure 6.5: The distribution (black) of the difference between the measured Δx values calculated with the pseudomass method and the expectation ($\Delta x = 0\,\mu\text{m}$) divided by the uncertainty of the measured parameter in bins of η for 30 toy experiments. The expected statistical behaviour, represented by a Gaussian centered around zero, is drawn in red. The upper two rows correspond to Eq. 6.5. In the central row the muon charges have been randomised. In the lower row Eq. 6.6 is used. For reference, Table 6.1 reports the means and widths of a Gaussian fit performed on each of the pull distributions shown here.

Figure 6.5 (upper row) shows the distribution over the 30 toys of the *pull*, i.e. the difference between the correction derived using the proposed method and the expectation ($\Delta x = 0\,\mu\text{m}$), divided by the statistical uncertainty of the measured parameter in each of the η bins. Since the most interesting patterns are observed along η, an integration over ϕ bins is performed. The expected statistical behaviour, represented by a Gaussian centered around zero, is drawn in red. It can be observed that the pull distributions have means that are systematically shifted from zero, by up to three standard deviations, with a strong dependence on η. This is an effect of the forward-backward asymmetry in $Z \to \mu\mu$ decays that drives differences between the kinematic distributions of μ^+ and μ^-. Figure 6.5 (central row) shows that this bias is eliminated when the charges of the Z boson decay products are randomised, so that the number of μ^+ and μ^- falling in each $[\eta, \phi]$ bin is the same (i.e. effectively "switching off" the forward-backward asymmetry). The small bias

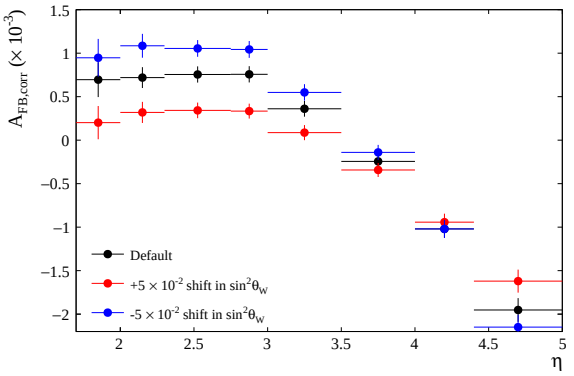

Figure 6.6: The pseudomass asymmetry in bins of the muon pseudorapidity. The asymmetry is shown for three different values of $\sin^2\theta^{\text{eff}}_{\text{lept}}$, including two extreme variations (red and blue) around the nominal value (black).

can be corrected using simulation but, given that the aim of this method is its application to measurements of m_W and $\sin^2\theta^{\text{eff}}_{\text{lept}}$, careful attention is required for the dependence of this bias on the value of $\sin^2\theta^{\text{eff}}_{\text{lept}}$ assumed in the simulation. A sample of around 10^7 events (with a larger number of events than in the 30 toy experiments) is used to determine this correction with high statistical precision. Figure 6.6 shows the resulting pseudomass asymmetry values in bins of η for the nominal value of $\sin^2\theta^{\text{eff}}_{\text{lept}}$ (black points) and $\pm 5 \times 10^{-2}$ variations (red and blue points). The pseudomass asymmetry shifts by at most 5×10^{-4} for these extreme variations, corresponding to roughly ± 300 times the uncertainty on the current world average value of $\sin^2\theta^{\text{eff}}_{\text{lept}}$ [6]. Ref. [107] shows that the same variations in $\sin^2\theta^{\text{eff}}_{\text{lept}}$ lead to far greater changes in the profile of the mean $1/p_T$ asymmetry versus η. The pseudomass asymmetry therefore appears to be better suited than the $1/p_T$ asymmetry for the determination of curvature biases with $Z \to \mu\mu$ events. A small correction for this bias can now be included in Eq. 6.5, as follows:

$$\delta \approx (A - A_{FB,\text{corr}}) \frac{< \frac{1}{p^+} > + < \frac{1}{p^-} >}{2}, \tag{6.6}$$

where $A_{FB,\text{corr}}$ corresponds to the black points in Fig. 6.6. Figure 6.5 (lower row) shows that using Eq. 6.6 the curvature biases can be determined without bias, since the pull distributions of the Δx values are consistent with standard normal distributions in all the bins considered. For reference, Table 6.1 reports

Table 6.1: The means and widths of the Gaussian fit performed on each of the pull distributions shown in Fig. 6.5.

	$1.75 < \eta < 2$		$2 < \eta < 2.3$		$2.3 < \eta < 2.75$		$2.75 < \eta < 3$		$3 < \eta < 3.5$		$3.5 < \eta < 4$		$4 < \eta < 4.4$		$4.4 < \eta < 5$	
	$\bar{x}$	σ	$\bar{x}$	σ	$\bar{x}$	σ	$\bar{x}$	σ	$\bar{x}$	σ	$\bar{x}$	σ	$\bar{x}$	σ	$\bar{x}$	σ
No A_{FB} bias correction	1.04	1.19	1.20	0.96	1.41	0.50	1.17	1.19	0.67	1.27	-0.51	1.37	-1.51	1.15	-1.86	1.04
A_{FB} "switched off"	-0.39	1.52	0.11	1.2	-0.10	1.34	0.40	1.47	-0.23	1.34	-0.23	1.17	-0.49	1.52	-0.15	1.18
With A_{FB} bias correction	0.39	1.19	0.32	1.02	0.28	0.60	0.08	1.13	-0.02	1.19	0.33	1.47	0.19	1.31	0.19	1.06

the means and widths of a Gaussian fit performed on each of the pull distributions shown in Fig. 6.5.

6.5 Application of the method

The pseudomass method is tested on a subset of 3×10^6 events from the sample described in Section 6.2. The muon momenta are re-calculated to mimic the effects of five mis-alignment scenarios that could be present in a LHCb-like geometry. These include *coherent* translations or rotations of the entire measurement plane and *incoherent* translations, which instead depend on the track coordinate and are parameterised in bins of η and ϕ. In all cases the *additional* deflection (Δx) of a track along x due to the introduced mis-alignment is calculated, and the corresponding variation in the momentum is derived from Eq. 6.2. The five mis-alignment scenarios are configured as follows.

1. Coherent translation along x ($\Delta x = 50\,\mu\text{m}$).

2. Coherent translation along z ($\Delta z = 100\,\mu\text{m}$): the corresponding deflection along x is
$$\Delta x = \Delta z \frac{\cos\phi}{\sinh\eta}. \tag{6.7}$$

3. Coherent rotation in the $x - y$ plane ($R_z = 0.2\,\text{mrad}$): the corresponding deflection along x is
$$\Delta x = \frac{\cos(\phi + R_z) - \cos\phi}{\cos\phi} \frac{\text{m}}{p/\text{GeV}}. \tag{6.8}$$

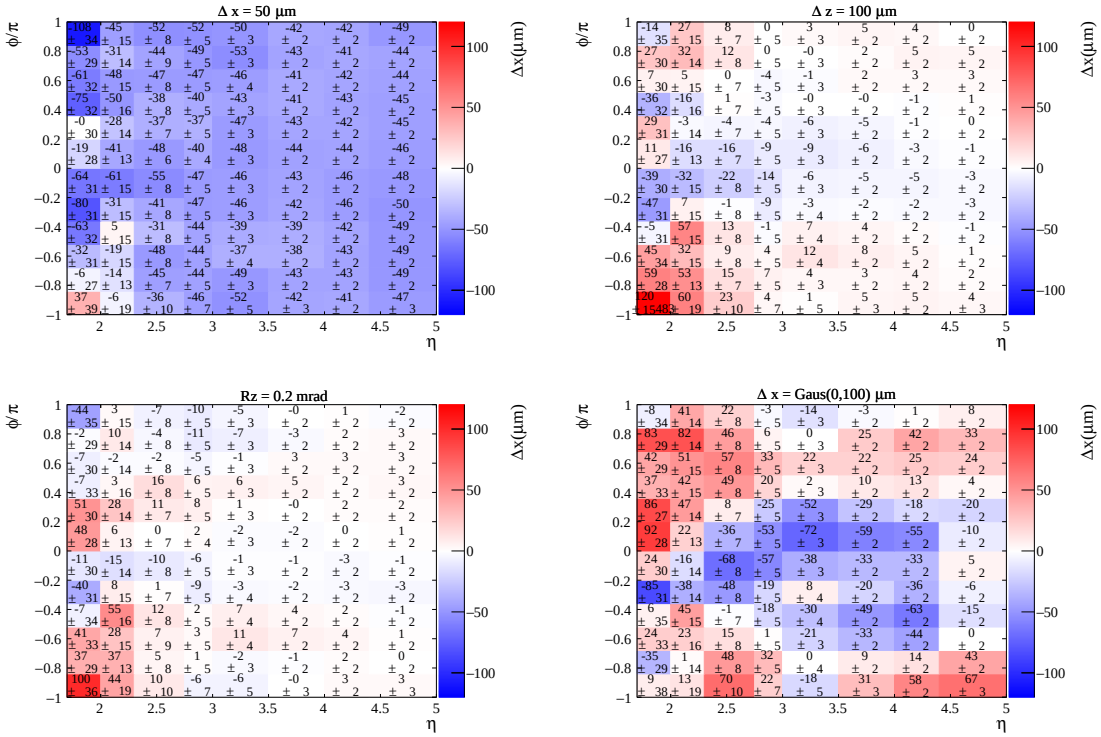

Figure 6.7: The pseudomass correction in bins of $[\eta, \phi]$ for (clockwise from upper left) a coherent $\Delta x = 50\,\mu\text{m}$, coherent $\Delta z = 100\,\mu\text{m}$, coherent $R_z = 0.2\,\text{mrad}$, incoherent $\Delta x = \text{Gaus}(0, 100)\,\mu\text{m}$.

4. Incoherent translation along x, with the Δx values randomly sampled from a symmetric Gaussian distribution with a width of 100 μm in each of the η and ϕ bins corresponding to the same binning scheme as the pseudomass corrections.

5. Incoherent translation along x with five η bins instead of eight, so that the binning scheme is slightly different to that used in the pseudomass corrections.

Maps of the curvature bias corrections in the η and ϕ bins are determined for each mis-alignment scenario, and are presented in Fig. 6.7. An iterative procedure is required because Eq. 6.5 is only accurate to leading order. The *residual* corrections of each iterations are added to the map of corrections from the previous iteration. Iterations stop when the size of the residual corrections are zero within their statistical errors in most $[\eta, \phi]$ bins. With the analysed dataset, this happens with around two iterations. It is now interesting to study

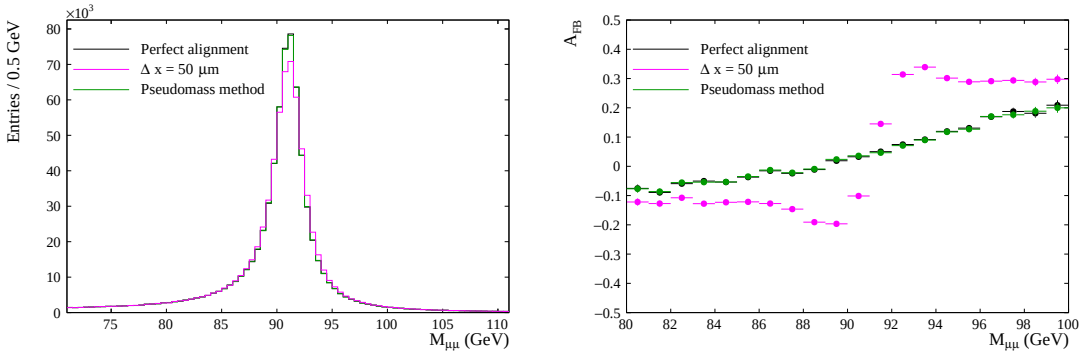

Figure 6.8: The dimuon invariant mass distribution (left) and the forward backward asymmetry in bins of the dimuon invariant mass (right), for simulated events with a coherent $\Delta x = 50\,\mu\text{m}$ (magenta), after applying the pseudomass corrections (green), and the unbiased distribution, with no mis-alignment applied (black).

the effect of the pseudomass corrections on the applied mis-alignments for several curvature-bias sensitive observables. Figure 6.8 shows the dimuon invariant mass ($M_{\mu\mu}$) distribution and the forward backward asymmetry in bins of $M_{\mu\mu}$ in the simulation. The black histogram and points correspond to the simulated events before mis-alignment, while the magenta (green) versions correspond to the mis-aligned (coherent $\Delta x = 50\,\mu\text{m}$ scenario) simulation before (after) the pseudomass corrections. The mis-alignment degrades the $M_{\mu\mu}$ resolution by around 10% and biases the A_{FB} values by up to 30% in some mass bins. However, the pseudomass method successfully restores the original mass resolution and A_{FB} profile.

Figure 6.9 shows the profiles of the mean $M_{\mu\mu}$ in bins of the ϕ of the μ^+ and μ^- and as a function of the angle between the decay plane normal and the magnetic field direction (ϕ_d). In the simulated LHCb-like geometry ϕ_d distinguishes tracks with opposite-sign curvature in the $x - z$ plane (i.e. tracks that point inwards or outwards with respect to the beam line). The lower row of Fig. 6.9 shows the values of A_{FB} as a function of $M_{\mu\mu}$. The left (right) columns correspond to before (after) applying the pseudomass corrections. The black points correspond to the simulation before mis-alignment while the other three colours correspond to the three coherent mis-alignment scenarios described above. It can be seen that the profile of A_{FB} versus $M_{\mu\mu}$ is particularly sensitive to the Δx translation, while the

$\phi_\pm$ and ϕ_d profiles are sensitive to the Δz translation. Figure 6.9 shows that the pseudomass corrections reliably resolve both of these pathologies.

Figure 6.10 shows the same four alignment-sensitive profiles as in Fig. 6.9 but considering incoherent mis-alignments along the x axis. By construction, the size of the local mis-alignment depends on random numbers. Therefore, it is appropriate to repeat the study for multiple toy data sets, generated by sampling the mis-alignments from different random seeds. The bands in Fig. 6.10 are centered on the mean value across 10 toys, and their width is given by their RMS. The red (blue) bands correspond to the values before (after) applying the pseudomass corrections to the mis-aligned events. For most points the blue bands are at least a factor of two narrower than the red bands. The reduction in the width of the band is particularly evident for the mass dependence of A_{FB}. Similar results are obtained for the fifth mis-alignment scenario, corresponding to a different binning scheme in η and ϕ.

It is now interesting to evaluate the sensitivity of measurements of electroweak observables to each of the studied mis-alignment scenarios. The values of m_W and $\sin^2\theta^{\rm eff}_{\rm lept}$ are extracted from the same sample of generator events, using a simple single-parameter χ^2 fit described in greater detail in Section 6.6. Assuming the signal yields for LHCb Run 2 calculated in Ref. [9], the statistical uncertainties on m_{W^+}, m_{W^-}, and $\sin^2\theta^{\rm eff}_{\rm lept}$ are 9 MeV, 11 MeV and 43×10^{-5}, respectively. Table 6.2 lists, for each of the three parameters of interest, the shift in the measured value and the $\Delta\chi^2$ that is induced by the first four mis-alignment scenarios. The overall bias for m_W is obtained from the weighted average of the biases for m_{W^+} and m_{W^-}, and is reported in a separate column in Table 6.2. The largest biases in all three parameters are caused by the (coherent and incoherent) mis-alignments along the x direction. Rotations around, or translations along, the z axis lead to smaller biases. The next obvious step is to understand whether the pseudomass method is able to correct for such biases.

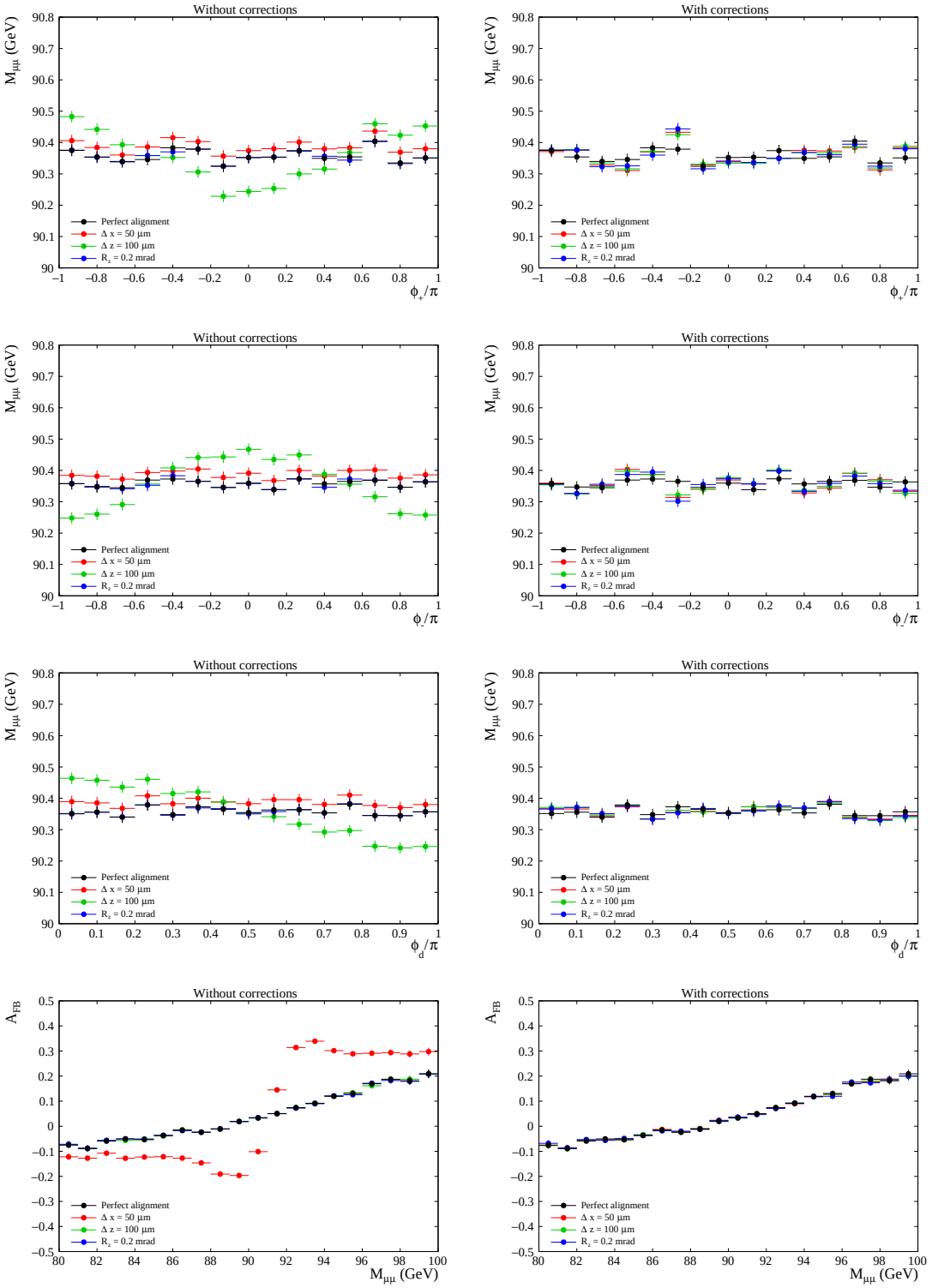

Figure 6.9: The first three rows show the profiles of the mean dimuon invariant mass in bins of ϕ_+, ϕ_- and ϕ_d. The lower row shows the A_{FB} values in bins of mass. The black points correspond to the simulation with no mis-alignment while the other colours correspond to the first three mis-alignment scenarios. The left and right columns correspond to the simulation before and after application of the pseudomass corrections, respectively.

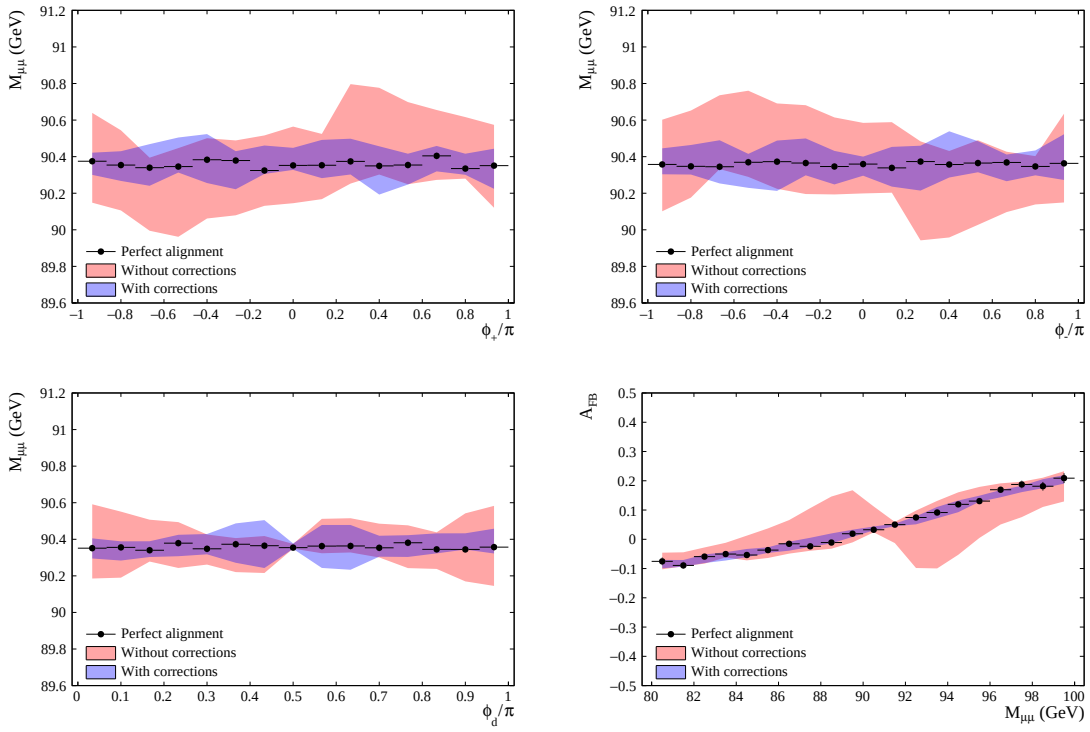

Figure 6.10: Profiles of the mean dimuon invariant mass in bins of ϕ_+, ϕ_- and ϕ_d, and the A_{FB} values in bins of mass. The black points correspond to the simulation before any mis-alignment. The red (blue) band represents the variations over ten toy experiments with the 100 µm incoherent mis-alignment scenario before (after) application of the pseudomass method. The centre (width) of each band corresponds to the mean (RMS) of the ten toys.

Table 6.2: The biases in the values of m_{W^+}, m_{W^-} and $\sin^2\theta^{\text{eff}}_{\text{lept}}$, and the corresponding shifts in the minimum χ^2 values, that are caused by the first four mis-alignment scenarios in an example toy measurement. The overall bias in m_W, given by the weighted average of the biases for m_{W^+} and m_{W^-}, is also reported.

	m_{W^+}		m_{W^-}		m_W	$\sin^2\theta^{\text{eff}}_{\text{lept}}$	
	Bias (MeV)	$\Delta\chi^2$	Bias (MeV)	$\Delta\chi^2$	Bias (MeV)	Bias ($\times 10^{-5}$)	$\Delta\chi^2$
Coh. $\Delta x = 50\,\mu\text{m}$	-574	268	+590	92	-50	+211	960
Coh. $\Delta z = 100\,\mu\text{m}$	-1.2	2	-5	5	-2.9	-0.6	0.1
Coh. $R_z = 0.2\,\text{mrad}$	-0.4	0.2	-0.1	1.6	-0.3	-4	3
$\Delta x = \text{Gaus}(0, 100)\,\mu\text{m}$	-101	52	+98	79	-11	-65	28

6.6 Impact of the pseudomass method on the measurement of electroweak observables

The sample of $Z \to \mu\mu$ events described in Section 6.2 is complemented by samples of 2×10^7 $W^+ \to \mu^+\nu_\mu$ decays and 2×10^7 $W^- \to \mu^-\bar{\nu}_\mu$ decays to perform simplified measurements of $m_{W^\pm}$. Events are selected with muons in the region $2 < |\eta| < 5$, reducing both samples to around 10^7 events. For each of the three parameters of interest (m_{W^+}, m_{W^-} and $\sin^2\theta^{\text{eff}}_{\text{lept}}$) 90 toy measurements are conducted.

The measurements of m_W are based on template fits to the muon p_T distribution of $W \to \mu\nu$ events, while the measurements of $\sin^2\theta^{\text{eff}}_{\text{lept}}$ are based on template fits to A_{FB} in bins of the dimuon mass in $Z \to \mu\mu$ events. The data histograms are compared to templates where events are reweighted to emulate different m_W and $\sin^2\theta^{\text{eff}}_{\text{lept}}$ hypotheses. The toy experiments are configured differently for measurements of m_W and $\sin^2\theta^{\text{eff}}_{\text{lept}}$. For m_W, toy data histograms are generated by randomly fluctuating the bins around the nominal muon p_T distribution 90 times, assuming the expected LHCb Run 2 yields [9] and Poisson statistics. The same procedure can not be used for the A_{FB} templates, since the $Z \to \mu\mu$ events used for the $\sin^2\theta^{\text{eff}}_{\text{lept}}$ determination are also used to determine the pseudomass alignment corrections. The re-use of events could in principle cause biases in the determination of $\sin^2\theta^{\text{eff}}_{\text{lept}}$. Therefore, 90 statistically independent samples are selected from the original simulated data set.

For each data histogram a single-parameter fit determines the m_W or $\sin^2\theta^{\text{eff}}_{\text{lept}}$ value that minimises the χ^2 between the data and the templates. The 68% C.L. statistical uncertainty corresponds to a variation of $\Delta\chi^2 = 1$ with respect to the parabola minimum.

The pull distributions for the extracted values of m_{W^+} and $\sin^2\theta^{\text{eff}}_{\text{lept}}$ in 90 toys are shown in Fig. 6.11. Qualitatively consistent results are seen for the W^-, so the figure is omitted for brevity. What is denoted as "ref" value in the pull distributions is the nominal m_W or $\sin^2\theta^{\text{eff}}_{\text{lept}}$ value, which is aligned with the central template hypothesis. A Gaussian distribution with zero mean and unit width is drawn in magenta: this is the expected distribution over the 90 toys assuming that the

statistical uncertainties on the extracted values of m_W and $\sin^2\theta^{\text{eff}}_{\text{lept}}$ have the correct coverage. Even before applying any mis-alignment to the simulated events, the impact of the pseudomass method on the measurements of m_W and $\sin^2\theta^{\text{eff}}_{\text{lept}}$ can be evaluated. Four scenarios are considered:

1. The pseudomass correction are *not* included in either the toy data or template events.

2. The pseudomass corrections are derived from the Z sample and then applied to W and Z events when generating the data and template histograms. The curvature biases are determined with Eq. 6.5, i.e. without the small correction for the decay-asymmetry bias. This scenario is not shown in Fig. 6.11, but is discussed below.

3. Same as scenario 2, but with the decay-asymmetry bias corrections (Eq. 6.6) applied to *only* template events.

4. Same as scenario 3, but with the decay-asymmetry bias corrections applied to *both* toy data and template events.

Figure 6.11 shows that in the first scenario the pull distributions for m_W and $\sin^2\theta^{\text{eff}}_{\text{lept}}$ are consistent with the ideal Gaussian functions. Instead, a small bias is observed in the $\sin^2\theta^{\text{eff}}_{\text{lept}}$ pulls when the pseudomass corrections are applied without including the decay-asymmetry bias correction in the templates (red curve), thus introducing a discrepancy in the way the alignment corrections are applied to data and templates. However, the unbiased behaviour is restored after including the additional decay-asymmetry corrections. For clarity of the plot, the second scenario of the list above (no decay-asymmetry bias corrections in data and model) is not included in the plots, but an unbiased result is observed also in that case.

Finally, it is interesting to check what happens to the four scenarios described above when a detector mis-alignment is included. Figure 6.12 shows the shift in the extracted m_{W^+} and $\sin^2\theta^{\text{eff}}_{\text{lept}}$ values with respect to the reference value for the same 90 toys. The distributions drawn with blue lines are obtained from unbiased data.

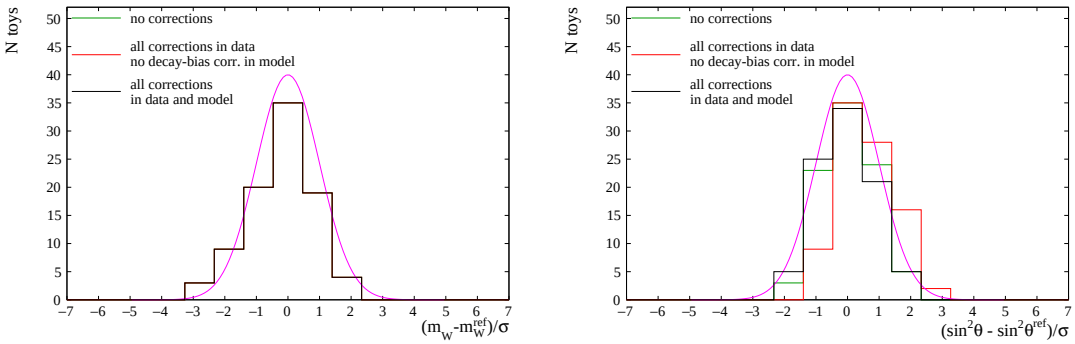

Figure 6.11: The pull distributions for 90 toy measurements of (left) m_{W^+} and (right) $\sin^2\theta^{\text{eff}}_{\text{lept}}$. Three different scenarios are represented: 1) the pseudomass and decay-asymmetry bias corrections are not included in the toy data and template events (green); 2) the pseudomass corrections are applied to toy data and templates, but the decay-asymmetry bias corrections are not included in the the templates (red); 3) the pseudomass and decay-asymmetry corrections are applied to *both* toy data and templates (black). Note that, in the case of m_W, the three distributions overlap. The expected statistical behaviour, represented by a unit Gaussian, is drawn in magenta.

Table 6.3: The mean values of the distributions shown in red in Fig. 6.12 (where a 5 µm mis-alignment along x is applied to the toy data), before and after applying the pseudomass corrections. The biases on m_W are reported in MeV.

Bias in m_{W^+} (MeV)		Bias in m_{W^-} (MeV)		Bias in $\sin^2\theta^{\text{eff}}_{\text{lept}}$ ($\times 10^{-5}$)	
Before (After) corr.	$\sigma_{\text{stat.}}$ on m_{W^+}	Before (After) corr.	$\sigma_{\text{stat.}}$ on m_{W^-}	Before (After) corr.	$\sigma_{\text{stat.}}$ on $\sin^2\theta^{\text{eff}}_{\text{lept}}$
-62 (-1)	9	+56 (0.7)	11	+26 (9)	43

Those with red lines are obtained from data with a coherent 5 µm mis-alignment along x. The upper (lower) row shows the results before (after) applying the pseudomass corrections. In order to estimate the size of the bias on m_W and $\sin^2\theta^{\text{eff}}_{\text{lept}}$ driven by the introduced mis-alignment, the distributions in red are fitted with a Gaussian, and the corresponding means, before and after corrections, are reported in Table. 6.3. A 60 MeV bias in the extraction of m_{W^+} is estimated. Although the corresponding plot is not shown, an opposite-sign bias of similar size is observed for m_{W^-}. This confirms the sensitivity of the m_W measurement to small mis-alignment effects. The same size mis-alignment has a smaller effect on the extraction of $\sin^2\theta^{\text{eff}}_{\text{lept}}$, where the observed bias is within the statistical uncertainty of the measurement. However, the corrections have an impact on the best fit χ^2 values extracted from each toy, as shown in the upper panel of each set of plots.

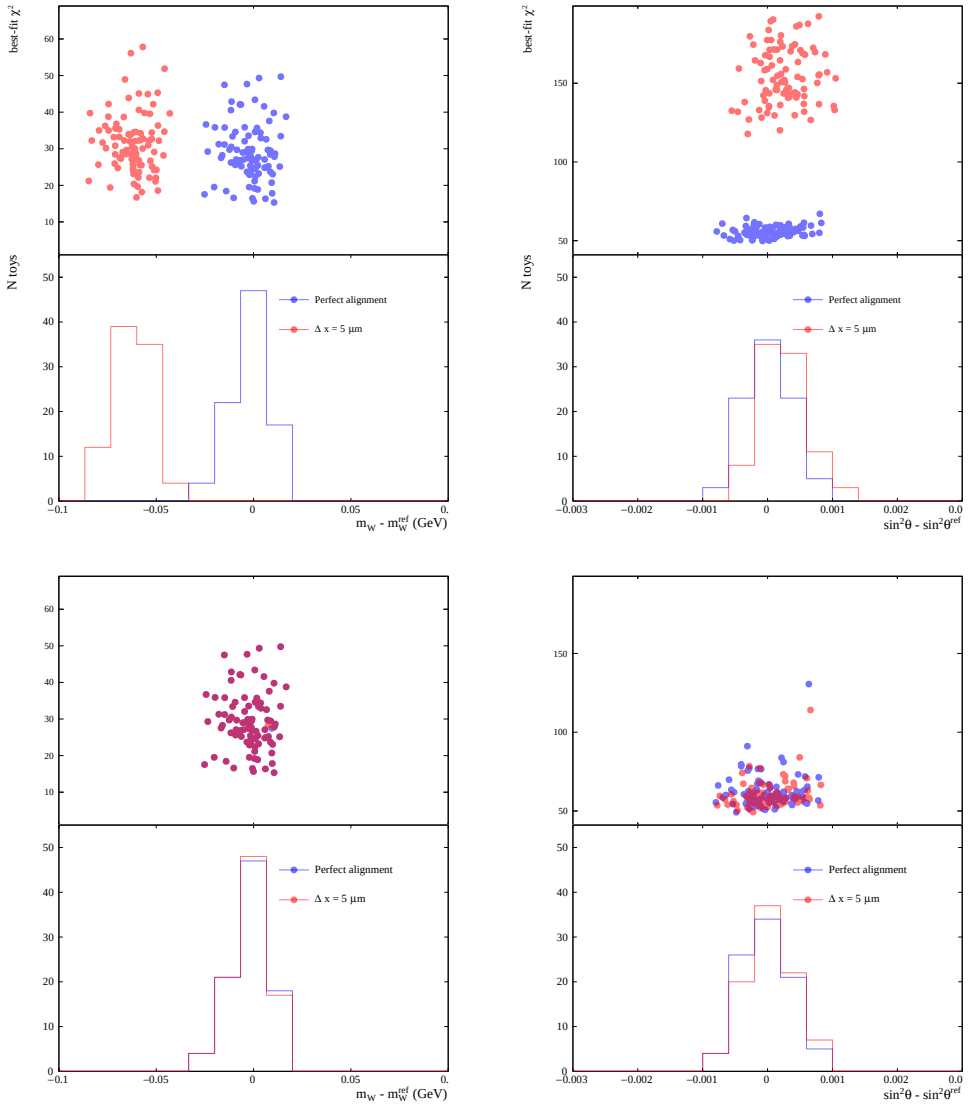

Figure 6.12: The shift in the extracted (left) m_{W^+} and (right) $\sin^2\theta^{\text{eff}}_{\text{lept}}$ values with respect to the reference value, in 90 toys. The upper (lower) row corresponds to the simulation before (after) application of the pseudomass method. The distributions drawn with blue lines are obtained from unbiased data. Those with red lines are obtained from toy data with a coherent 5 μm mis-alignment along x. The first (last) row of plots show the distributions before (after) applying the pseudomass corrections. The upper panel of each plot shows the best-fit χ^2 corresponding to the extraction of m_W and $\sin^2\theta^{\text{eff}}_{\text{lept}}$ for the 90 toys.

6.7 Summary

This chapter introduced the *pseudomass method* as a way to determine charge-dependent curvature biases using $Z \to \mu\mu$ decays. Such biases can potentially affects precision measurements of electroweak observables such as m_W and $\sin^2\theta^{\text{eff}}_{\text{lept}}$. The method is validated using simulated $pp \to Z \to \mu\mu$ events with the LHC Run 2 centre-of-mass energy of 13 TeV. A simplified model of a detector with a similar geometry to the LHCb experiment is used. The approach introduced by the pseudomass method has the advantage of being less dependent on assumptions about the kinematics of the Z boson decays than other methods present in the literature. The method is tested against several simplified mis-alignment configurations. Its applicability to measurements of m_W and $\sin^2\theta^{\text{eff}}_{\text{lept}}$ in the presence of these simplified mis-alignments has been tested with pseudo-experiments. Chapter 7 will describe how the application of the pseudomass method to the extraction of m_W with real data is crucial to improve the measurement of muon momenta and reduce its associated systematic uncertainty.

7

Muon momentum measurement

The single most important experimental aspect of the m_W fit model is the muon momentum measurement. Tracking performance studies on Monte Carlo events show that a momentum resolution of a few permille can be achieved for tracks that traverse the entire LHCb detector [40]. In order to achieve this momentum resolution, and a good mass resolution, the positions of the detectors need to be determined with real data with an accuracy well below the hit resolution for a given detector. High momentum muons from $W \to \mu\nu$ and $Z \to \mu\mu$ decays are particularly sensitive to mis-alignment effects, as the track curvature in the dipole magnet is very small. As discussed in Chapter 6, a global shift of $\mathcal{O}(10)\,\mu$m of the tracking stations can yield a bias in the measurement of m_W of around 30 MeV. The sensitivity to such levels of mis-alignments makes the momentum scale the dominant source of experimental systematic uncertainty in the m_W measurement.

The ultimate requirement for a measurement of m_W is that the Monte Carlo (MC), on which the fit model is based, accurately mimics the characteristics of the momentum measurement in the real data. These characteristics include the curvature bias, momentum scale, and curvature resolution. In the analysis, the MC is accurately shifted and smeared to match the data. This is done by simultaneously fitting $J/\psi, \Upsilon(1S)$ and Z data and simulation to derive the corrections to be applied to the Monte Carlo. In order to reduce the size of the corrections needed, it is

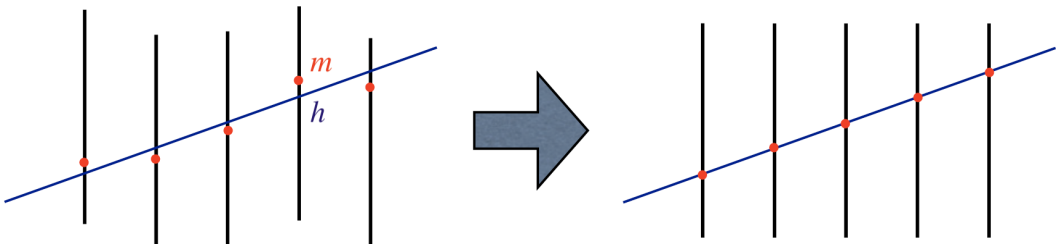

Figure 7.1: Track hits in the detector layers before (left) and after (right) the alignment.

important to first correct the data as much as possible for mis-alignment effects. This step will not be necessary in the presence of a perfect modelling of the detector response, which will be able to mimic the data mis-alignments itself. However, given the complexity expected by the model, the followed approach seems more reasonable.

7.1 Detector module level alignment

As mentioned in Chapter 3, the alignment procedure for the LHCb detector in Run 2 was performed for each fill in real-time [112]. The alignment is based on the χ^2 minimization of the *residuals* evaluated with a Kalman filter fit that takes into account multiple scattering and energy loss corrections [113]. A residual is the difference between the point where a track is expected to hit the detector and where it actually hits it, as illustrated schematically in Fig. 7.1. Mathematically, it can be defined as

$$r_i = m_i - h_i(\vec{x}, \vec{\alpha}), \tag{7.1}$$

where m_i and h_i are, respectively, the *measured* and *expected* position of the track hit on the i^{th} detector layer, $\vec{x}$ represents the track parameters and $\vec{\alpha}$ represents a set of alignment parameters. The latter are varied to minimize the track χ^2, defined as

$$\chi^2 = r^T V^{-1} r, \tag{7.2}$$

where V is the track covariance matrix. This method offers the possibility to apply mass and vertex constraints to the reconstructed tracks [114]. The sample used in the real-time alignment of the LHCb detector in Run 2 was collected in few minutes at the beginning of each fill. It consists of a *minimum bias* sample

(i.e. a sample that is selected with very loose trigger selections) applying a vertex constraint for the alignment of the VELO and a sample of D^0 mesons decaying into two charged particles with a mass constraint applied to the D^0 candidates for the tracking stations. In 2017, an alignment was performed *offline* using a sample of $Z \to \mu\mu$ events collected during 2016 with a mass constraint applied to the Z candidates. The results obtained with higher momentum tracks result in a more precise alignment. This alignment was used as input to the real-time alignment procedure since end of June 2018. Most of the analyses in the LHCb physics programme are not sensitive to the level of mis-alignments probed by the Z decays. However, because of the high-p_T nature of the tracks involved, the electroweak physics programme is particularly susceptible to the problem. The application of the Z custom alignment to the analysed data set consists of a refit of the tracks associated to the event of interest, correcting the coordinates of the track hits in each tracking modules with the aligned ones. The corrected kinematic quantities (e.g. the corrected muon momenta) are then extracted from the refitted tracks. Since this represents only the first correction applied in the alignment procedure, the Z custom alignment will be identified as *detector-level* alignment. Further corrections are needed to reach the level of precision required by the measurement.

The impact of the detector-level alignment on the analysed dataset is shown in Fig. 7.2 (left). The reconstructed dimuon invariant mass distribution in a sample of 2016 $Z \to \mu\mu$ data is plotted before (black) and after (red) the application of the Z alignment. An estimate of the improvement in the mass resolution is obtained by fitting each distribution with the theoretical $Z/\gamma^* \to \mu\mu$ lineshape, convoluted with a Gaussian resolution function, and comparing the widths of the two Gaussians. A 35% improvement in the mass resolution is observed. For reference, the dimuon invariant mass distribution in simulated events is shown in green. The results of the application of the detector-level alignment, optimised on 2016 data, to the full Run 2 dataset can be observed in Fig. 7.2 (right). The average trend of an alignment-sensitive quantity, here the muon track χ^2, is shown through Run 2, expressed in LHC fill numbers. The χ^2 gives an indication of how well a track

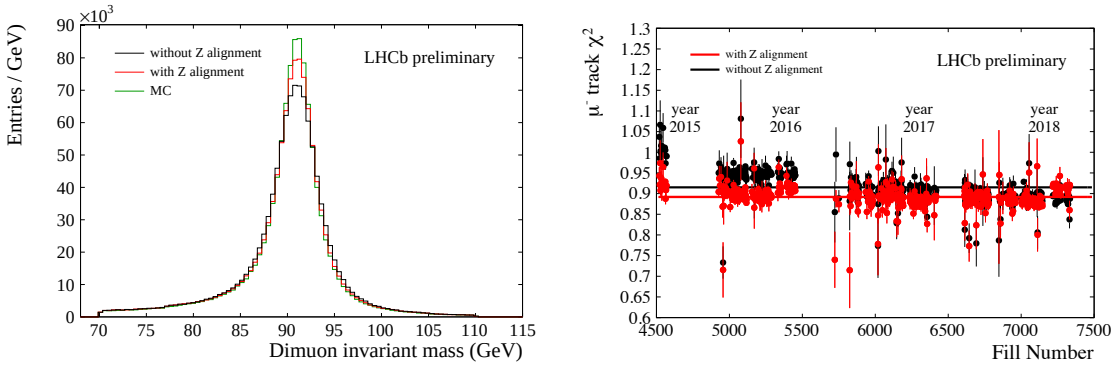

Figure 7.2: Left: dimuon invariant mass of the 2016 $Z \to \mu\mu$ sample for data with and without custom alignment applied (red and black respectively), and comparison with simulated events in green. Right: mean muon track χ^2 for events in the Run 2 fills. The red (black) points correspond to data with (without) Z custom alignment applied.

can be constrained to the predicted origin vertex, and the quality of the track fit naturally improves for a better aligned detector. The plot shows a clear separation between different years of data taking (four blocks for 2015, 2016, 2017 and 2018 respectively). The empty regions correspond to time intervals where no relevant data taking took place (e.g. due to short periods of technical shutdowns, or machine development, or lead-lead collisions). The application of the detector-level alignment greatly improves the data quality in general, except for the last fills of 2018; as mentioned above, for that data taking period the Z-optimised alignment is used as default in the LHCb online detector calibration. Therefore, that period will require further investigation, but it is outside of the scope of this thesis.

7.2 Fill dependent momentum scale calibration

The calibration of the momentum scale in a particle physics detector can be performed using large samples of two-body decays of *standard candle* resonances (e.g. $J/\psi \to \mu\mu$), by comparing the invariant mass of the reconstructed tracks to known values. However, it has been observed by many LHCb analyses that the masses of such resonances drifted for various LHC fills of the year 2016. After the application of the Z custom alignment described earlier, a correction is derived using $\Upsilon(1S) \to \mu\mu$ events in bins of fill number. The $\Upsilon(1S)$ candidates are

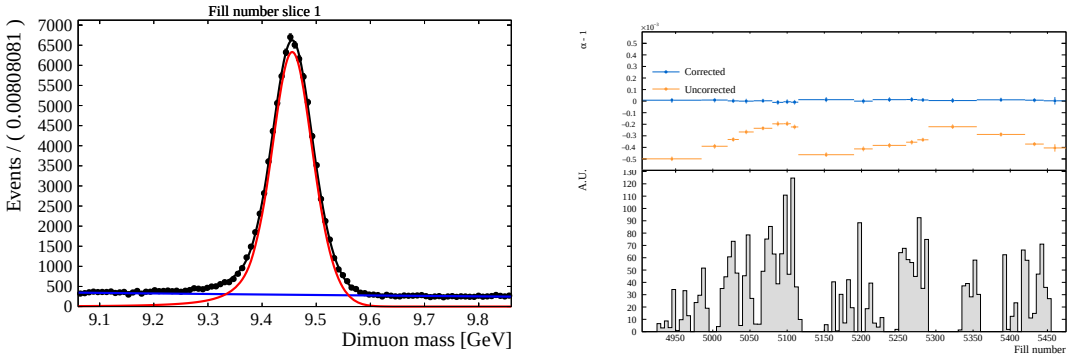

Figure 7.3: Left: an example fit of the $\Upsilon(1S) \to \mu\mu$ lineshape for the first fill number slice. The double Crystall Ball and the exponential component are indicated in red and blue, respectively. Right: the fill number distribution and the momentum scale corrections (orange) in coarse bins of fill number. The residual corrections after applying the scale corrections are shown in light blue.

selected with both muons in the $2.2 < \eta < 4.4$ region used for the selection of $W \to \mu\nu$ candidates. The signal lineshape is described by the sum of two Crystal Ball functions with shared α_{CB}, n_{CB} and mean (m_{CB}) parameters, but with independent width parameters. The background is described by an exponential function. Figure 7.3 (left) shows an example of fit to the $\Upsilon(1S)$ lineshape for the first fill number slice. The momentum scale correction is approximated by $\alpha = M_{\mathrm{PDG}}/m_{\mathrm{CB}}$, where $M_{\mathrm{PDG}} = 9460.30 \pm 0.26$ MeV is the 2020 PDG value of the $\Upsilon(1S)$ mass [6]. Figure 7.3 (right) shows the resulting α values in the fill number bins relative to the year 2016. The average $1 - \alpha$ value is around 3×10^{-4}, with a systematic variation at the level of $\mathcal{O}(10^{-4})$. These values are applied as momentum scale corrections to all muons in the data. Figure 7.3 (right) also shows the $1 - \alpha$ values that would be obtained *after* applying the fill dependent scale corrections and the pseudomass curvature corrections. These values are found to be flat as a function of fill number, and close to zero, which serves as a closure test of the procedure. The fill-dependent scale corrections are followed by the pseudomass-based curvature corrections described in Sec. 7.3.

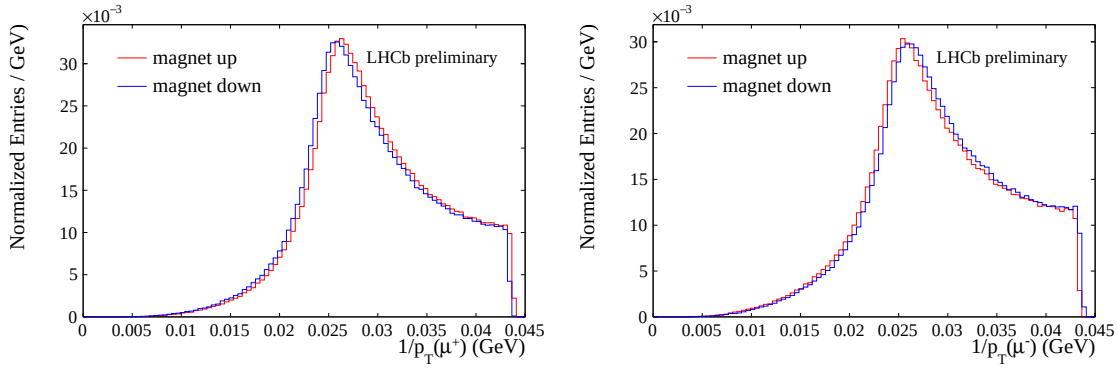

Figure 7.4: The muon $1/p_T$ distributions in magnet-up (down) configuration in red (blue) after the Z custom alignment. Positively and negatively charged muons are shown in the left- and right-hand side plots respectively.

7.3 Higher-level curvature corrections: the pseudomass method

Despite the significant improvements from the Z custom alignment described in Sec. 7.1, the residual mis-alignments are still too large to be absorbed by the simplified MC smearing model at this stage. For example, Fig. 7.4 shows large differences between the muon $1/p_T$ distributions for $W \to \mu\nu$ data divided into the two polarity configurations of the dipole. Similar differences have been observed in muons of the 13 TeV $Z \to \mu\mu$ sample. The polarity bias is observed when the fit is performed separately for the two polarity configurations, as a consistency check. It is expected that the resulting m_W values are consistent within the experimental errors. A difference of 725 ± 48 MeV between the extracted m_W values was first observed in October 2019 in a fit on 40% of the full 13 TeV dataset. This polarity difference can be attributed to a residual mis-alignment. This important finding inspired the development of the pseudomass method described in Chapter 6. In the m_W measurement presented here, the method is used to derive the residual alignment corrections on top of the detector-level alignment. The pseudomass corrections are derived independently for fourteen bins of the muon ϕ and eight bins of η. Separate corrections are given depending on whether tracks have hits in the inner silicon strip region of the tracking stations downstream the magnet (the Inner Tracker). The corrections are determined separately for magnet polarities.

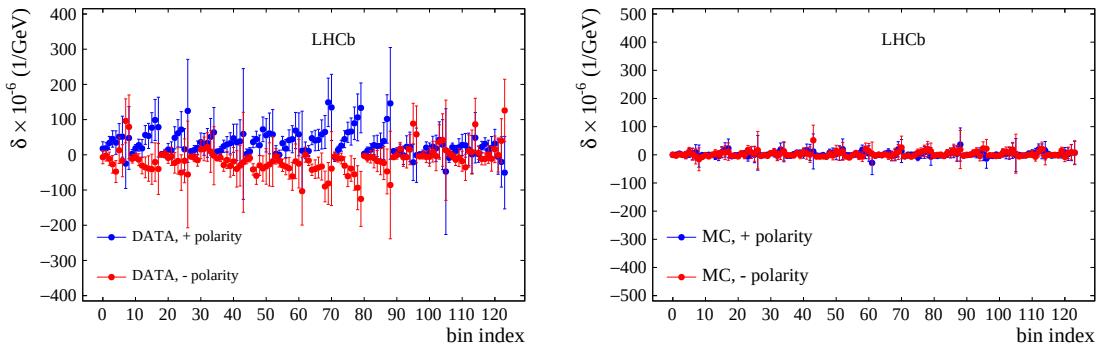

Figure 7.5: The pseudomass corrections applied to data (left) and simulation (right) for magnet-up (blue) and magnet-down (red) events, as a function of the bin index of the $[\eta, \phi]$ grid.

An iterative procedure is required because Eq. 6.5 is only accurate to leading order. The *residual* corrections of each iteration are added to the corrections map of the previous iteration. Iterations stop when the size of the residual corrections are zero within their statistical errors in most $[\eta, \phi]$ bins. With the analysed dataset, this happens with around five iterations.

Figure 7.5 (left) shows the size of the corrections applied to magnet-up and down data as a function of the bin index in the $[\eta, \phi]$ grid. In principle, the simulated events might be subject to biases in the way tracks are reconstructed. Therefore, to ensure that data and MC are treated as equally as possible (which is essential for the reliability of the template fit), the pseudomass corrections are derived and applied to both data and simulated events. As shown by Fig. 7.5 (right), the size of the corrections applied to the MC is much smaller than the corrections to the data.

The impact of the pseudomass corrections is studied on several alignment diagnostics plots. Figure 7.6 shows the dimuon invariant mass distribution in data before and after applying the pseudomass corrections. The three plots in Fig. 7.7 show the dependencies of the mean dimuon invariant mass on three alignment-sensitive quantities: the muon momentum asymmetry (A_P), and the azimuthal angle (ϕ) of the positively and negatively charged muons. Three different configurations are compared: data with only detector-level alignment (magenta), data with pseudomass alignment (green) and the Monte Carlo prediction for these

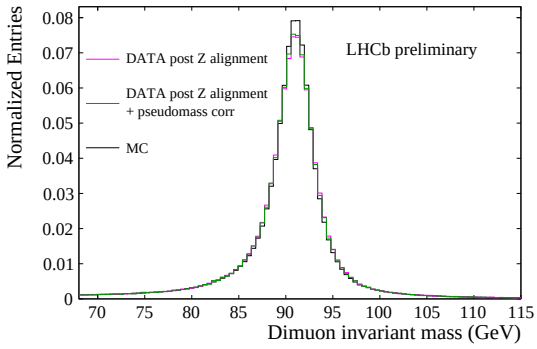

Figure 7.6: The dimuon invariant mass distribution before and after applying the pseudomass corrections. Data with detector level (pseudomass) alignment are shown in magenta (green), together with the simulation predictions in black.

trends (black). It is reassuring that the newly implemented corrections greatly reduce the residual mis-alignment trends in the data.

The next step is to check what is the effect of the pseudomass alignment in the m_W fit. Figure 7.8 shows that the new corrections greatly reduce the differences between the muon $1/p_T$ distributions in $W \to \mu\nu$ data for magnet-up and magnet-down polarity configurations. The same improvement is observed in muons from Z decays. It is anticipated that the measurements of m_W performed separately for magnet-up and magnet-down data agree within 1.5 standard deviations. This is a fundamental improvement, which is mainly driven by the application of the pseudomass corrections. More details are discussed in Chapter 8.

7.4 Calibration of the muon momentum in the simulation

Having discussed how to improve the momentum resolution in data, it is important to also make the simulation more representative of data. One of the crucial aspects of the measurement of m_W is the accurate modelling of the muon momentum measurement in simulated events. In the present analysis, this is achieved by applying a series of corrections to the muon momenta. Because the resolution in data is worse than MC, this analysis only considers the case where smearing corrections are applied to the *simulated* muon momenta. The corrections are

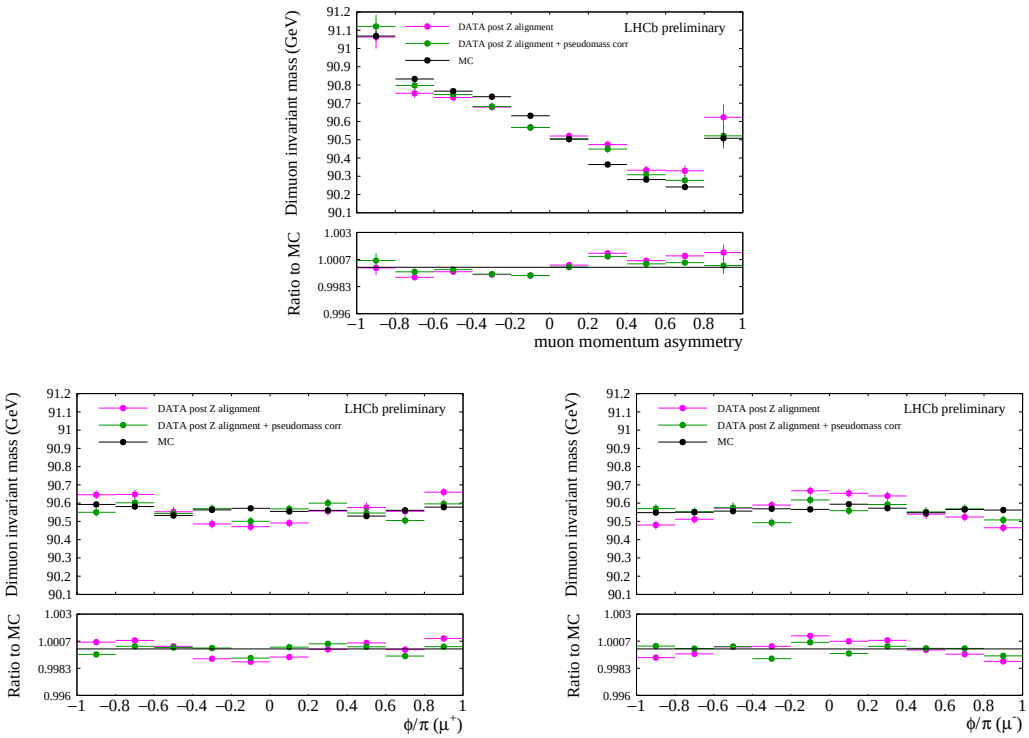

Figure 7.7: The dependence of the mean dimuon invariant mass on the muon momentum asymmetry (A_P) (top), and the azimuthal angle (ϕ) of the positively and negatively charged muons (bottom). Data with detector level (pseudomass) alignment are shown in magenta (green), together with the simulation predictions in black. The lower panel of each plot shows the ratio between data and simulation, for the two alignment configurations considered.

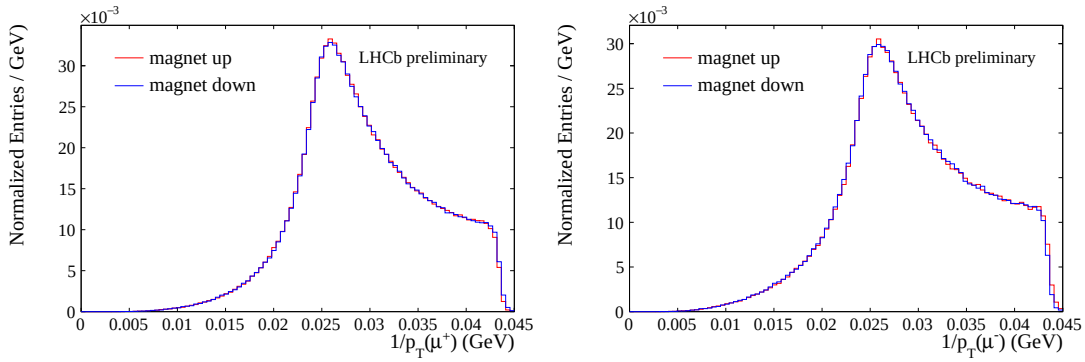

Figure 7.8: The muon $1/p_T$ distributions in magnet-up (down) configuration in red (blue) after the pseudomass corrections. Positively and negatively charged muons are shown in the left- and right-hand side plots respectively.

determined from a simultaneous fit of data and simulated events that are already corrected for residual mis-alignment effects, as described in the previous section. By applying the alignment corrections to the data first, it is expected that the size of the additional corrections that are determined from the following procedure will be smaller. A stochastic smearing is applied to the simulated muon momenta (p), using the following smearing function:

$$\frac{q}{p} \to \frac{q}{p \cdot \mathcal{N}(1+\alpha, \sigma_{\mathrm{MS}})} + \mathcal{N}\left(\delta, \frac{\sigma_\delta}{\cosh\eta}\right), \tag{7.3}$$

The function consists of four discrete transformations:

1. a *curvature bias* correction[1]: $\frac{q}{p} \to \frac{q}{p} + \delta$;

2. a momentum *scale* correction: $p \to (1+\alpha)p$;

3. a momentum-independent *smearing* which accounts for multiple scattering effects when the particle traverses the detector. The smearing factor is a random number distributed like a Gaussian ($\mathcal{N}$) of unit mean and floating width: $p \to p \cdot \mathcal{N}(1, \sigma_{\mathrm{MS}})$, where σ_{MS} is scaled by a factor of 1.5 for muons with $\eta > 3.3$. The extra scaling accounts for the larger amount of radiation length seen by the higher-η tracks up to the LHCb magnet [115];

4. a curvature resolution, momentum-dependent *smearing*: $p \to p \cdot \mathcal{N}\left(1, \frac{\sigma_\delta}{\cosh\eta}\right)$. The $1/\cosh\eta$ is found to improve the agreement between data and simulation.

A simultaneous fit of $J/\psi \to \mu\mu$ and $\Upsilon(1S) \to \mu\mu$ and $Z \to \mu\mu$ data and simulated events is performed to determine the values of δ, α, σ and σ_p that provide the best agreement between data and model. The model includes six parameters in total. There are two momentum scale (α) parameters corresponding to the range $2.2 < \eta < 4.4$ (which coincides with the selection cut of W candidates), and $\eta < 2.2$ regions. A single δ parameter covers the region $2.2 < \delta < 4.4$, while the value of δ is fixed to zero in the region $\eta < 2.2$. There are two σ_δ parameters

[1]This is a *residual* curvature bias correction, and is applied in addition to the pseudomass corrections described in Section 7.3

Table 7.1: Categorisation of the dimuon mass distributions in bins of η used in the fit.

	$1.8 < \eta^+ < 2.2$	$2.2 < \eta^+ < 3.3$	$\eta^+ > 3.3$
$1.8 < \eta^- < 2.2$	1	2	3
$2.2 < \eta^- < 3.3$	2	4	5
$\eta^- > 3.3$	3	5	6

corresponding to the $2.2 < \eta < 4.4$ and $\eta < 2.2$ regions, while a single σ_{MS} parameter is found to adequately cover all η values. All the parameters are shared between magnet polarities. This approach allows to float a limited number of parameters (thus gaining stability in the fit) while keeping the sensitivity to the most important elements of the momentum smearing model. The observable used in the fit is the invariant mass distribution of the Z and *quarkonia* ($\Upsilon(1S)$ and J/ψ) decay products, plotted into six fiducial categories, which are labeled as shown in Table 7.1. The quarkonia are only used to constrain the scale parameters in the m_W fit fiducial region ($2.2 < \eta < 4.4$), therefore categories 1, 2 and 3 are not included in the fit. These categories are still included for the Z mass distributions, since the control of the momentum scale in the lower η region is needed for the Z component of the m_W fit, where it is required that *at least* one muon satisfies the W-like η selection requirement.

The invariant mass distribution for the Z sample in categories 4, 5 and 6 is further split into three bins of the muon momentum asymmetry (A_P), to enhance the sensitivity to curvature biases in the m_W fit fiducial region. Finally, each dimuon mass distribution is split by magnet polarity. The division into categories ensures larger sensitivity to the effects of the smearing parameters on the simulated events. The fit minimises the sum of 36 χ^2 terms (i.e. the dimuon mass categories described above). The finite statistical precision of the simulated sample is handled with the Beeston-Barlow lite [116] prescription. The smearing function also includes floating exponential background components for the quarkonia samples. No background fraction is included for the Z sample, as it is expected to be very low. It was observed that adding a floating exponential component for the Z background

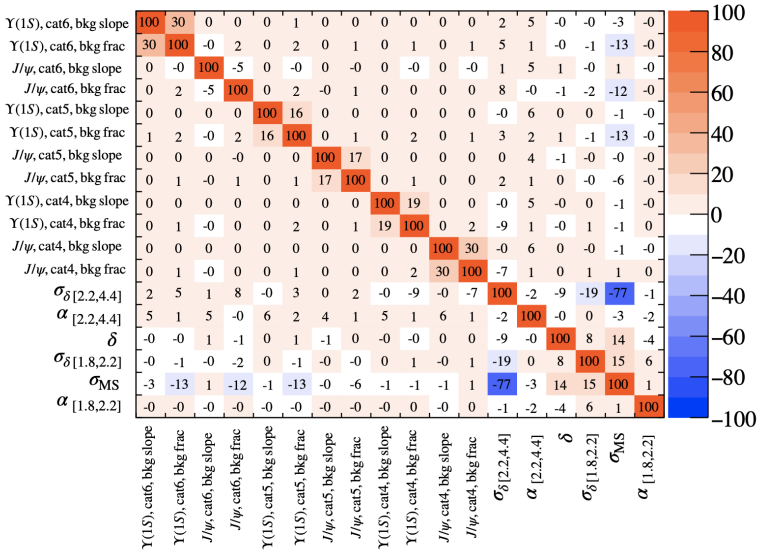

Figure 7.9: Correlations between the parameters of the momentum scale fit.

changes the value of m_W by fractions of MeV and, therefore, it is neglected. The total χ^2 from the fit is 1862 for 2082 degrees of freedom. The postfit parameters of the smearing model and their statistical errors are shown in Tab.7.2. Table 7.9 shows the correlations between the fit parameters. No strong correlations are observed. Figure 7.10 shows the dimuon mass distributions for the Z, J/ψ and $\Upsilon(1S)$ after combining all categories with both muons in the $2.2 < \eta < 4.4$ range. The data are reasonably well described by the postfit model. Particularly for the Z, it is very interesting to note how the application of the Z alignment and the pseudomass corrections improves the resolution in the data, such that very little residual smearing needs to be applied to the simulated events.

Table 7.2: Postfit values of the six parameters in the momentum smearing model.

Parameter	Postfit value
α $(\eta < 2.2)$	$(0.58 \pm 0.10) \times 10^{-3}$
α $(2.2 < \eta < 4.4)$	$(-0.0054 \pm 0.0025) \times 10^{-3}$
δ	$(-0.48 \pm 0.37) \times 10^{-6}$ GeV^{-1}
σ_δ $(\eta < 2.2)$	(17.7 ± 1.2) keV^{-1}
σ_δ $(2.2 < \eta < 4.4)$	(14.9 ± 0.9) keV^{-1}
σ_{MS}	$(2.015 \pm 0.019) \times 10^{-3}$

7.4.1 Test of the statistical coverage of the fit

Since the fit is performed on binned histograms, a change of the smearing parameter can cause an event to shift from one bin to another. A smoothing term is included in the χ^2 metric to mitigate for this effect. Nevertheless, it is important to check the statistical coverage of the fit. This can be done by running simple toy studies. A simple and fast event generator is used to generate Z, $\Upsilon(1S)$ and J/ψ events. A subset of these events is used to mimic data, while the complementary subset is used as model (MC). The statistics of each toy study mimics the one actually used in the real data analysis, which is summarised in Table 7.3. A 10% fraction of background events is simulated for the quarkonia samples, assuming a uniform mass distribution. A reconstruction bias in included in the event generation using a two-level approach:

1. a detector resolution smearing ($\Delta p/p$ vs p) with reference values taken from

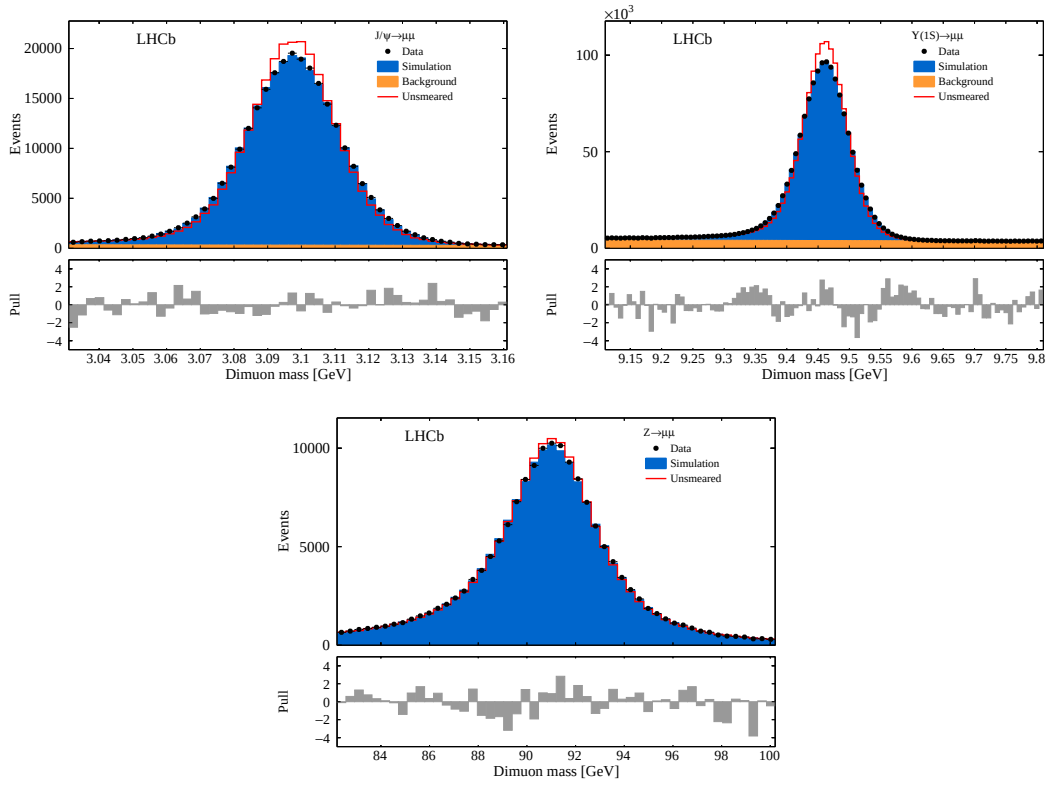

Figure 7.10: The dimuon mass distributions for selected J/ψ, $\Upsilon(1S)$ and Z candidates. All fit categories with both muons within the $2 < \eta < 4.4$ region are combined. The data are compared with the postfit model of simulation plus (for the quarkonia models) background.

Table 7.3: Statistics for a single toy in the statistical coverage study.

	Z events	J/ψ events	$\Upsilon(1S)$ events
DATA	2.1 $\times 10^5$	4.7 $\times 10^5$	4.1 $\times 10^6$
MC	1.3 $\times 10^6$	2.4 $\times 10^5$	2.1 $\times 10^6$

RapidSim [117] is applied to both data and simulation;

2. momentum-dependent and momentum-independent Gaussian smearings are subsequently applied *only to the data*, to mimic worse resolution in data than MC. The size of the smearing is chosen to roughly mimic the smearing size in the real data analysis.

The fit runs on 200 toys, using the same fitting machinery which is used in the analysis of the real data. Figure 7.11 reports the results of the fit on one of the 200 toys. For brevity, only the three most populated categories (one for each Z, $\Upsilon(1S)$ and J/ψ sample) are shown. The fraction of background events in the quarkonia samples returned by the fit is compatible with that introduced in the event generation, thus confirming the correct behaviour of the fit.

For each parameter of the detector response model (x), the distribution of the *pulls*, i.e. the difference between the output value from the fit to a single toy with respect to the average across all the toys ($\bar{x}$), divided by the statistical error on x, is reported in Fig. 7.12 (black curve). In the case of perfect statistical coverage, the expected distribution would be a Gaussian with mean equal to zero and unit width (as shown by the red curve in Fig. 7.12). This behaviour can be observed in the pull distributions for the momentum scale and curvature bias corrections, except for the scale parameter for $\eta < 2.2$. An undercoverage effect can be observed, instead, for the smearing parameters. The lack of Monte Carlo statistics in the quarkonia samples, as shown in Table 7.3, could drive this undercoverage. In order to test this hypothesis, a new set of events is generated, assuming eight times more quarkonia MC events in each toy. The corresponding pull distributions are shown

by the blue curves in Fig. 7.12. The increase in the MC sample yield restores the correct statistical coverage also for the smearing parameters.

During the development of this analysis it was observed that the uncertainty on m_W from the parameters determination is mainly driven by the momentum scale and curvature bias parameters in the region $\eta > 2.2$. The undercoverage effects observed for the smearing parameters vary the overall systematic uncertainty on the momentum smearing model by only 1%, and are therefore neglected.

7.5 Uncertainty on the muon momentum measurement model

The statistical uncertainty on the smearing model parameters is calculated from a multivariate Gaussian resampling of the model parameters from the fit covariance matrix. A new set of smearing parameters ($\bar{x}_{\text{new}}$) can be determined from the

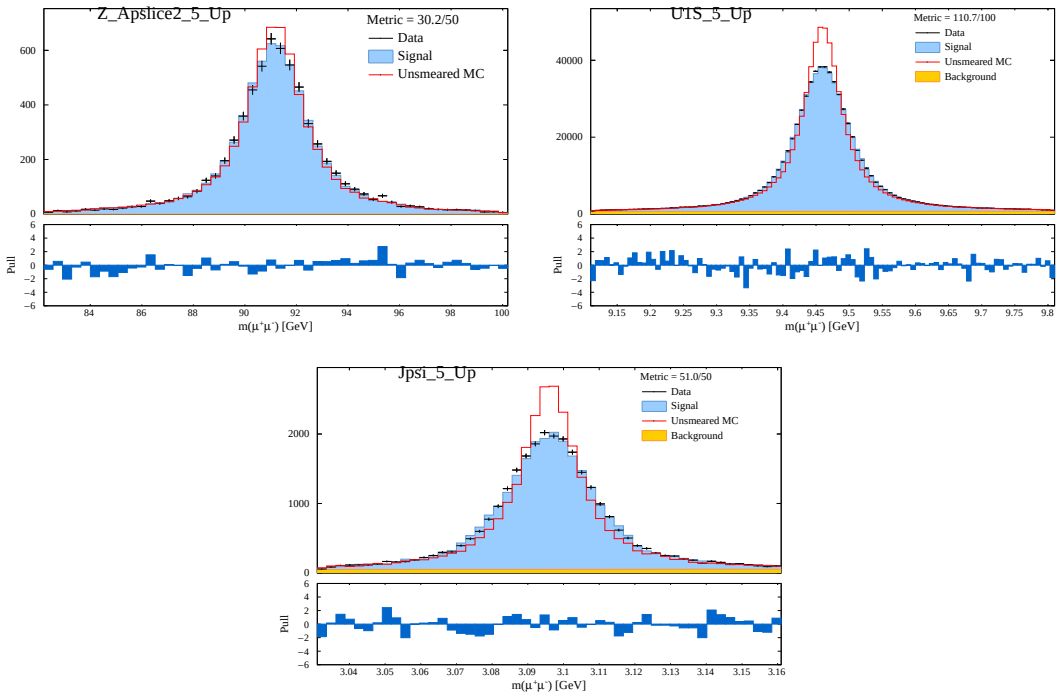

Figure 7.11: Results of the coverage test for one of the 200 toys: the dimuon invariant mass distributions for Z and quarkonia samples in the three most pupulated categories for data (in black), unsmeared simulated events (red) and smeared simulated events using the best-fit corrections (light blue template, with the background component shown in orange).

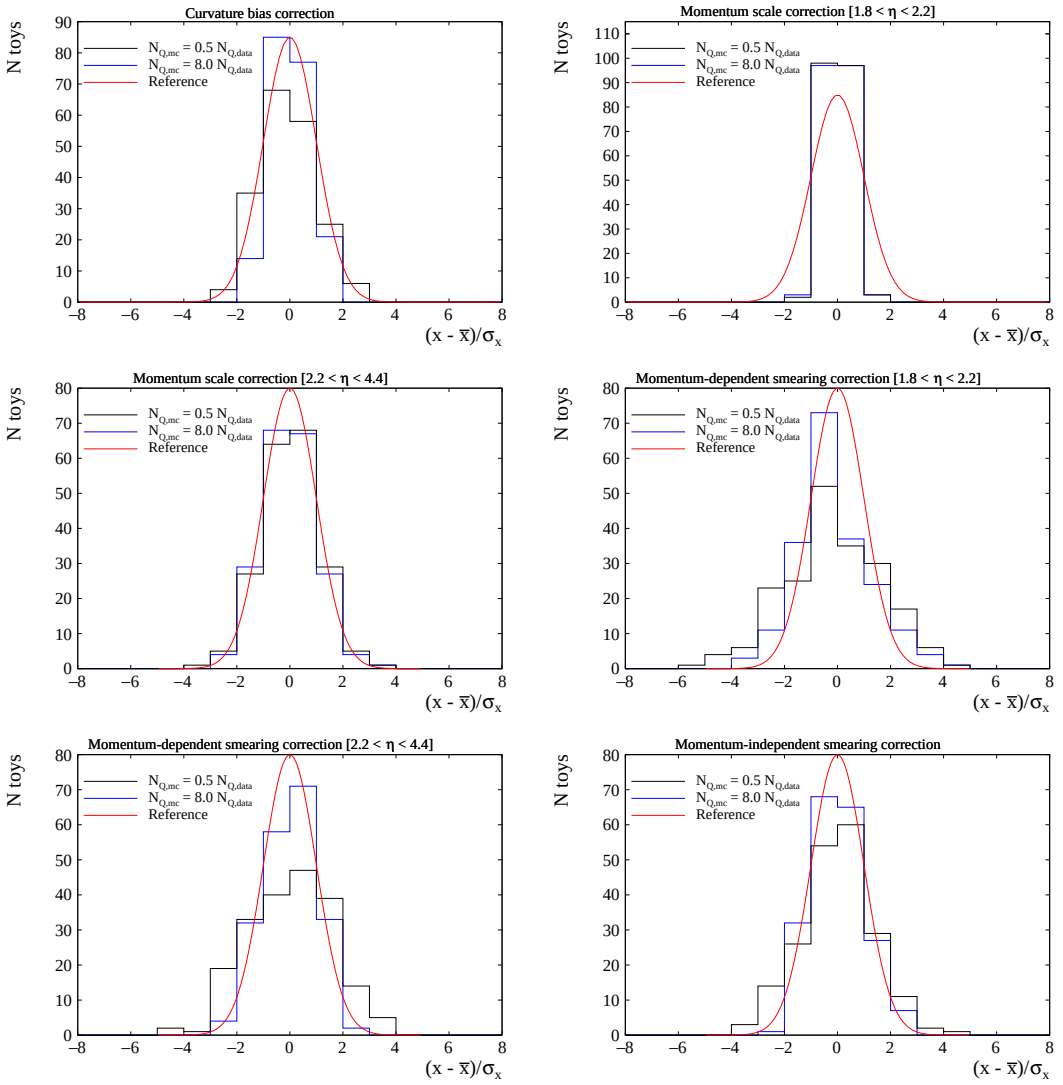

Figure 7.12: The pull distributions for 200 toys, for each parameter of the detector response model. The expected Gaussian distribution in case of perfect statistical coverage is shown in red; the distribution assuming Table 7.3 is shown in black; the distributions obtained assuming 8 times more quarkonia MC events are shown in blue.

fit covariance matrix using the following:

$$\bar{x}_{\text{new}} = \bar{x}_{\text{orig}} + A\bar{z}, \tag{7.4}$$

where $\bar{x}_{\text{orig}}$ is the original set of parameters determined by the fit, $\bar{z}$ is a set of Gaussian-distributed random numbers with zero mean and unit width, and A is the Cholesky decomposition [118] of the covariance matrix[2].

[2]The matrix A is defined such that $AA^T = C$, where C is the covariance matrix.

Fifty variations of the simulated events are thus generated and the m_W fit is run for each of them. The uncertainty, defined as the RMS of all the variations, is around 3 MeV. Other variations in the smearing model are accounted for as additional sources of systematic uncertainty:

- a $\pm 1\sigma$ variation in the PDG value of the $\Upsilon(1S)$ mass, which yields a ± 2 MeV uncertainty on m_W. The same variation in the Z mass has a $\mathcal{O}(10^{-2})$ MeV on m_W, therefore it is not included as an additional systematic uncertainty;
- four variations in the modelling of the radiative losses in the quarkonia MC samples (two for the J/ψ and two for the $\Upsilon(1S)$). The corresponding uncertainty on m_W is around 2.5 MeV;
- a ± 2 MeV energy loss offset corresponding to 10% of uncertainty in the determination of the material budged seen by muon tracks before the magnet. A η-weighted average is performed to account for the fact that tracks below and above $\eta = 3.6$ see different percentages of detector material budget [119]. The corresponding uncertainty on m_W is around 3 MeV;
- variations in the smearing terms, in particular: i) an alternative form of the $1/\cosh\eta$ scaling factor in the width of the curvature smearing (σ_δ) and ii) a shift from 3.3 to 3.5 in the η edge above which the multiple scattering smearing (σ_{MS}) width is scaled by a factor 1.5. The corresponding uncertainty on m_W is around 5 MeV.

The purely systematic uncertanties listed above are added in quadrature to the statistical uncertainty on the parameters determination to get the total uncertainty on m_W from the momentum smearing model, which is estimated to be 7.5 MeV.

The muon momentum calibration for the next measurement of m_W will benefit from a much larger dataset, and will use the approach described in this chapter as a starting point for improvement. Some ideas for improvement are the addition of dimuon mass resonances to better constrain the muon momentum scale, the possibility of splitting the dataset into more pseudorapidity categories, and the inclusion of new smearing parameters in the fit, such as a floating energy loss correction.

8

The fit method and results

In order to extract m_W, a binned simultaneous template fit of W and Z data is performed, where the templates are based on fully simulated events. The W and Z signal template shapes are allowed to vary according to changes in the parameters used to reweight to a specific physics model prediction. This chapter reports the details of the configuration of the m_W fit, the fit results, the evaluation of the systematic uncertainties to m_W as well as several cross-checks that have been performed in the pre-unblinding phase of the analysis.

8.1 Design of the fit

The m_W fit consists of the minimisation, using the ROOT MINUIT application [120] of a χ^2 with two terms:

- the W term includes the q/p_T distribution with a dominant $W \to \mu\nu$ signal, several electroweak and heavy flavour background components, and a prompt hadron decay component;
- the Z term includes the ϕ^* distribution already introduced in Chapter 6 with a $Z \to \mu\mu$ signal component and several small electroweak background components. In the early developments of the analysis, the fit observable used

for the Z component was p_T^Z. However, this was found particularly susceptible to momentum smearing systematic uncertainties in the region $p_T^Z < \mathcal{O}(2)\,\text{GeV}$. The ϕ^* distribution, instead, is independent of the muon momenta. Therefore, it is less sensitive to the details of the smearing model while still being sensitive to the parameters affecting the predicted vector boson p_T distributions.

The q/p_T distribution for the W term includes two fit regions covering the range $28 < p_T < 52\,\text{GeV}$. Projections of the q/p_T distribution cover a wider interval with $p_T > 24\,\text{GeV}$ that allows to show regions outside the fit, as illustrated in Fig. 5.1. Regarding the Z term, events with $\phi^* < 0.5$ are included in the fit but events with higher ϕ^* values are shown in the postfit projections. All fit components are derived from full simulation event samples with event-by-event weights (w). The weight assigned to each event is given by the product of the various weights that correct for the physics and detector differences described in Chapter 5. The finite statistical precision of the component templates is handled with the Beeston-Barlow "lite" prescription [116]. With this approach, the χ^2 term is modified by introducing a nuisance parameter β in each bin that accounts for the total MC estimate and the total statistic uncertainty in that bin. The two χ^2 terms described above are therefore computed as

$$\chi^2_{\text{term}} = 2\sum_i \left\{ \beta\mu - n\log(\beta\mu) + \frac{(\sum w)^2(\beta-1)^2}{2\sum w^2} \right\}, \tag{8.1}$$

where n and μ are the observed and expected number of events in bin i, respectively, after scaling the sum of weights to the total number of observed events.

The model of the q/p_T distribution includes the dominant $W \to \mu\nu$ signal component and several backgrounds. The largest background source is represented by $Z \to \mu\mu$ decays, with a fraction of around 5%. The contribution of $W \to \tau\nu$ and the prompt hadron decay background fraction is around a few percent. Rarer backgrounds such as $Z \to \tau\tau$, top-quark decays, di-bosons production, and heavy flavour decays (i.e. $b\bar{b}$, $c\bar{c}$) give a total contribution of fractions of percent. The model of the ϕ^* distribution, instead, includes backgrounds from $Z \to \tau\tau$ and top-quark decays.

The fractions of the $W \to \mu\nu$ signal components and the prompt hadron decay background are floating parameters in the fit. The fractions of all of the other components are fixed. In particular, the $W \to \tau\nu$ component is constrained relative to the floating $W \to \mu\nu$ fraction, using the known $\tau \to \mu\nu\bar{\nu}$ branching fraction [6]. The $W \to \tau\nu$ fraction is evaluated separately for each charge such that the charge asymmetry is consistent with the $W \to \mu\nu$ components. The other component fractions are predicted relative to the number of $Z \to \mu\mu$ candidates observed in the ϕ^* distribution using the fiducial cross-sections for the corresponding processes. A detailed list of the fit components and their predicted fractions is given in Appendix C.

The nominal physics model and reweighting method has been described in detail in Chapter 5 but is briefly summarised here. The unpolarised cross section is described by POWHEGPYTHIA with the `NNPDF31_nlo_as_0118` PDF set, but the fit allows freedom in the determination of the parton shower α_s and intrinsic k_T values. The angular coefficients are based on the DYTURBO predictions, with a floating A_3 scale factor. To summarise, the fit is configured to float the following parameters:

1. m_W,
2. the W^+ and W^- signal fractions ($f(W^{\pm})$),
3. the prompt hadron decay background fraction ($f_{\text{bkg}}^{\text{had}}$),
4. the α_s value for the Z processes (α_s^Z),
5. an independent α_s, shared between the W^+ and W^- processes (α_s^W),
6. a shared intrinsic k_T for all W and Z processes (k_T^{intr}),
7. a shared A_3 scaling factor for W^+ and W^- processes ($f(A_3)$).

In principle, the fit is able to float three different values for α_s and intrinsic k_T (i.e. separately for W^+, W^- and Z). It is anticipated that the nominal fit configuration chosen for the analysis is not particularly special, and several cross-checks have been performed to verify this assumption.

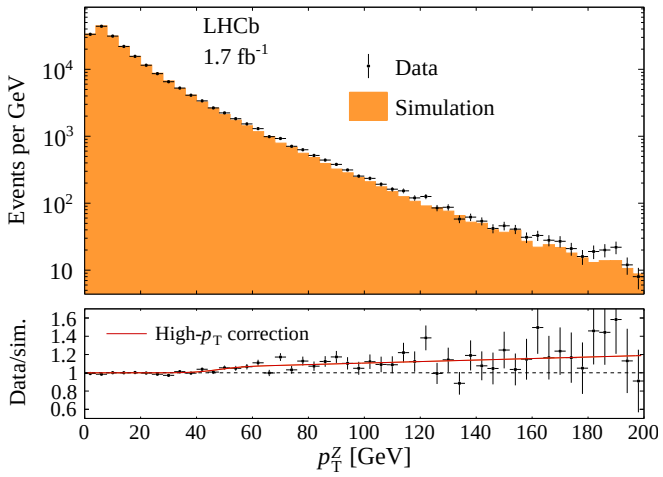

Figure 8.1: The prefit p_T^Z distribution from POWHEGPYTHIA compared to data. The lower panel shows the ratio overlaid with the parametric weight function.

8.1.1 Parametric correction at high transverse momentum

While POWHEGPYTHIA is able to describe the p_T^Z distribution in the region below 40 GeV, it is unable to adequately describe the higher p_T^Z region because the simulation does not account for the scenario of the production of a weak vector boson with more than one jet. Figure 8.1 shows the p_T^Z distribution in the data compared to the prediction by POWHEGPYTHIA when the α_s and k_T parameters are set close to the final fit values. It can be observed that the simulation underestimates the data up to $\mathcal{O}(10)\%$ for $p_T^Z \sim 100\,\text{GeV}$. In the lower panel of Fig. 8.1 the data/prediction ratio is overlaid with a parametric function which is flat in the region $p_T^Z < 40$ GeV, while it takes the form of an error function above 40 GeV so that it only influences the high p_T^Z tail. The function is used as an additional correction to the simulated events. It should be noted that only a small fraction of events with $p_T^Z > 40$ GeV, which influence the parameters of this function, leak into the fit region of the ϕ^* distribution. It was also verified that the shift in m_W corresponding to the inclusion of this correction is about 1 MeV which, as expected, is a small effect.

8.2 Results with the nominal fit model

The fit to the data returns a total χ^2 of 105 for 102 degrees of freedom. Figure 8.2 shows the postfit projections of the q/p_T (left) and ϕ^* distributions (right). The dashed lines delineate the fit region. The lower panels show the ratio between data and model including the envelope of the systematic uncertainties on m_W associated to the modelling of these distributions. The width of the band in each bin is defined by the quadrature sum of all systematic uncertainty sources which will be described in Section 8.4. The model is in good agreement with the data but underestimates the high p_T region of the muon q/p_T distribution by $\mathcal{O}(10)\%$. However, the underestimation is covered by the systematic uncertainty band shown in gray. Table 8.1 shows the postfit values and the statistical uncertainties on the floating parameters in the fit. A few postfit values of the floating parameters are worthy of comment:

- The *statistical* uncertainty on the m_W measurement with only 2016 data is around 23 MeV.
- The different fractions of W^+ and W^- signal components are motivated by the fact that the $W \to \ell\nu_\ell$ charge asymmetry is around +20% when the lepton is in the LHCb "forward" pseudorapidity range at $\sqrt{s} = 13\,\text{TeV}$ [121].
- The value of the α_s^Z components is around 0.124 as expected following the simplified fits described in Chapter 5.
- The value of α_s^W is 0.002 higher than α_s^Z but this can be attributed to the limited accuracy of parton shower based programs like POWHEGPYTHIA, which may translate into some process mis-modelling between W and Z production.
- The A_3 scaling factor is consistent with unity within standard deviation. This suggests that, within the statistics of the current dataset, the $\mathcal{O}(\alpha_s^2)$ predictions from DYTURBO are compatible with the data.

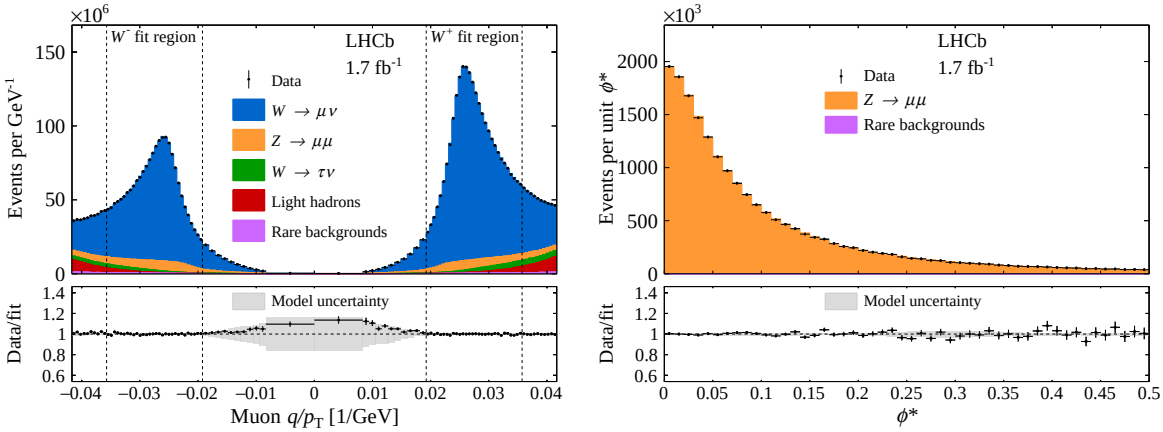

Figure 8.2: Projections of the postfit q/p_T and ϕ^* distributions, including the ratio between data and model and the systematic uncertainties band on the lower panel.

Table 8.1: The postfit values of the m_W fit with the NNPDF3.1 PDF set. The uncertainties quoted are statistical.

Floating parameter	Postfit value
Fraction of $W^+ \to \mu^+\nu$	0.5293 ± 0.0006
Fraction of $W^- \to \mu^-\nu$	0.3510 ± 0.0005
Fraction of hadron background	0.0151 ± 0.0007
α_s^Z	0.1243 ± 0.0004
α_s^W	0.1263 ± 0.0003
k_T^{intr}	$1.57 \pm 0.14\,\text{GeV}$
A_3 scaling	0.979 ± 0.026
m_W	$80362 \pm 23\,\text{MeV}$

8.3 Postfit plots

Several postfit plots are produced to ensure that the fit model describes some key target physics distributions. Figure 8.3 shows, for the Z sample, the postfit projections of the dimuon rapidity and the muon q/p_T distribution where the μ^+ and μ^- contributions have been filled separately with events that pass the W selection cuts on that charge. The model is found to be in good agreement with the data. It is also reassuring to note that the W-like muon q/p_T distribution is *not* normalised, which is a hint of the correct estimate of the muon reconstruction efficiencies.

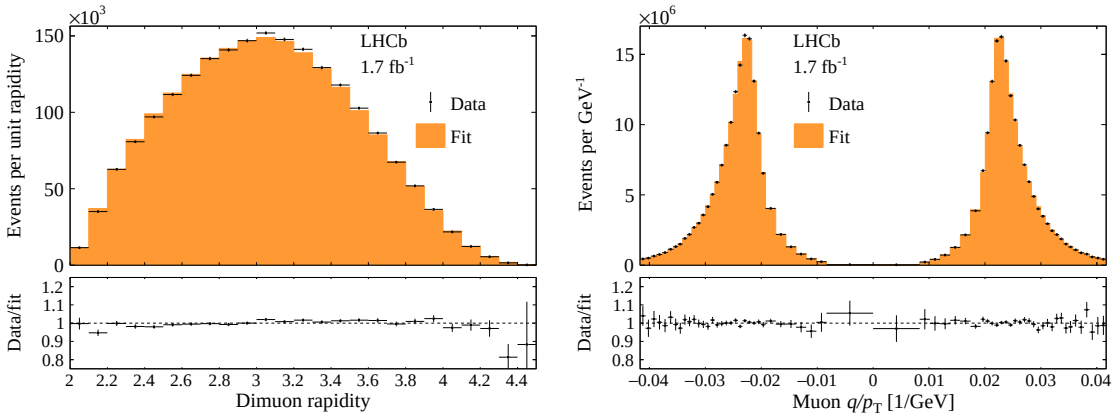

Figure 8.3: The postfit projections of key physics distributions for the Z sample: the dimuon rapidity (left) and the muon q/p_T distribution where the μ^+ and μ^- contributions have been filled separately including the W selection cuts on that charge (right).

8.4 Systematic uncertainties

Table 8.2 summarises the main contributions to the systematic uncertainty on the m_W measurement. The majority of sources are evaluated by running the fit on the real data but with variations in the configuration of the fit model. The dominant source of theory uncertainty in the m_W determination is represented by the modelling of the vector boson transverse momentum, followed by the uncertainty on the angular coefficients. The experimental systematic uncertainty is dominated by modelling of the detector response, but it is around 7 MeV smaller than the theory uncertainty. Table 8.2 also anticipates that the uncertainty on the PDFs is treated separately from the other modelling sources, since independent values of m_W are extracted from different PDF sets and the final result is calculated as the average of those values. This will be described in greater detail in Section 8.6. The total uncertainty, which is obtained by in quadrature the statistical uncertainty and the uncertainties on the Parton Distribution Functions, the theory and experimental uncertainties, is around 32 MeV.

Figure 8.4 shows a scatter graph of the fit χ^2 versus the shift in m_W for all fits that are included in the evaluation of the systematic uncertainties. The nominal fit result (at $\delta m_W = 0$) and the associated statistical uncertainty is also reported. All the model variations tend to shift m_W within the statistical

Table 8.2: List of contributions to the systematic uncertainty on m_W. Negligible contributions are not listed.

Source	Size [MeV]
Parton Distribution Functions	**9.0**
Theory (excl. PDFs) total	**17.4**
Transverse momentum model	12.0
Angular coefficients	9.0
QED FSR model	7.2
Additional electroweak corrections	5.0
Experimental total	**10.2**
Momentum scale and resolution modelling	7.3
Muon ID, trigger and tracking efficiency	5.5
Isolation efficiency	3.9
QCD background	2.3
Statistical	**22.7**
Total	**31.8**

uncertainty of the nominal fit and return reasonable fit χ^2 values. The only exception is represented by the points in magenta corresponding to the four variations in the modelling of the unpolarised cross-section described in Chapter 5, which return χ^2 values ten or twenty units larger.

8.5 Cross-checks

Several cross-checks have been performed before unblinding the value of m_W to check the consistency of the result. The first test consists in splitting the data and simulation into two orthogonal subsets by the muon η and ϕ, by magnet polarity and by the product of charge and polarity (so that each muon charge receives contributions from a single polarity dataset). These tests enhance the sensitivity to potential momentum scale and resolution mis-modelling. The results are reported in Table 8.3. It should be noted that, for all the reported cross-checks, the quoted uncertainties are only statistical. All differences are within, or just

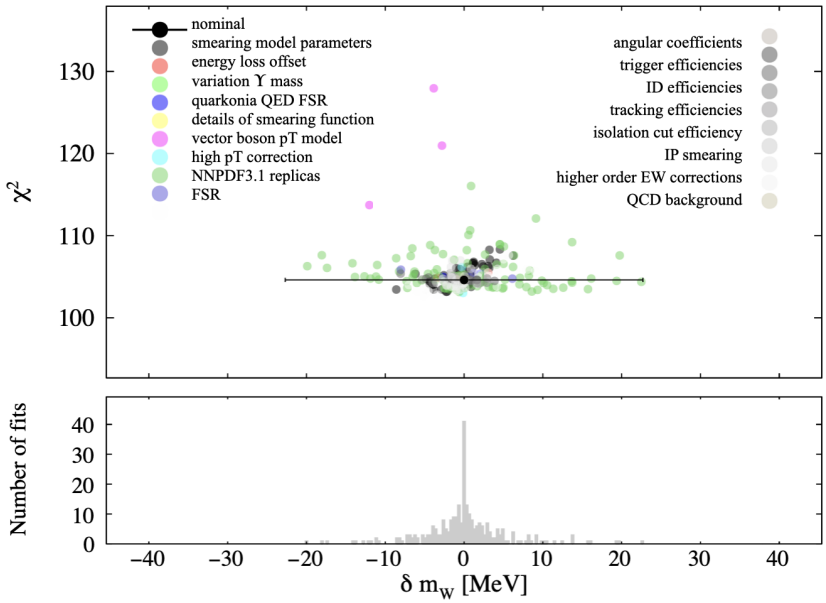

Figure 8.4: The χ^2 versus δm_W distribution including all model variations considered in the systematic uncertainty evaluation.

outside, two standard deviations, which was the criterion originally established to consider these tests as "passed".

The second set of cross-checks involves varying the fit range in the q/p_T distribution around the nominal values of $p_T^{\text{min}} = 28\,\text{GeV}$ and $p_T^{\text{max}} = 52\,\text{GeV}$. The shifts in m_W with respect to the nominal fit are reported in Table 8.4, together with the statistical uncertainties on m_W for each fit. It is concluded that the results are stable for variations in the fit range.

The third set of cross-checks consists in varying the freedom of the fit. The default fit configuration allows eight floating parameters. Table 8.5 reports how the fit result changes when other choices of floating parameters are made. The nominal fit has two floating α_s values, one for the Z processes and one shared between W^+ and W^-. Restricting the fit to a single α_s value yields an almost 40 MeV shift in m_W and an increase in the fit χ^2 by around 30 units. This confirms that POWHEGPYTHIA is unable to accurately describe W and Z processes with the same parameters. If three parameters are left floating there is almost no change in m_W or the fit quality. In the nominal fit a single shared k_T^{intr} parameter for all three processes is left floating. Neither the m_W value nor the fit χ^2 are strongly affected by

Table 8.3: A list of m_W fit results where the data and simulation samples are split into two orthogonal subsets. The uncertainties quoted are only statistical.

Subset	χ^2_{tot}/ndf	δm_W [MeV]
Polarity $= -1$	92.2/102	–
Polarity $= +1$	97.2/102	-57.5 ± 45.4
$\eta > 3.3$	115.5/102	–
$\eta < 3.3$	85.4/102	+56.9 ± 45.5
Polarity $\times$ $q = +1$	97.7/102	–
Polarity $\times$ $q = -1$	95.7/102	+16.1 ± 45.4
$\lvert\phi\rvert > \pi/2$ (tracker "A-side")	98.8/102	–
$\lvert\phi\rvert < \pi/2$ (tracker "C-side")	114.6/102	+66.7 ± 45.5
$\phi < 0$ (tracker upper-half)	91.7/102	–
$\phi > 0$ (tracker lower-half)	102.5/102	-100.5 ± 45.3

increasing to two or three parameters. Finally, if the A_3 scaling parameter is fixed to unity, the value of m_W shifts by around 4 MeV and the χ^2 increases by two units.

The consistency between m_W values for different W charges is also tested. An additional $\delta m_W = m_{W^+} - m_{W^-}$ parameter is left floating in the fit. This parameter is found to be consistent with zero within one standard deviation.

Finally, the method used to extract m_W is applied to the sample of $Z \to \mu\mu$ events to perform a W-like measurement of the Z boson mass (m_Z). The measured value of m_Z is found to be consistent with the PDG value [6] within one standard deviation.

8.6 PDF uncertainties

The uncertainty on m_W from the Parton Distribution Functions is estimated considering both variations in the replicas and variations in the value of α_s of the studied PDF sets. The measured value of m_W reported in Table 8.1 refers to the result obtained with the `NNPDF31_nlo_as_0118` set. Values of m_W are also obtained with two other PDF sets, namely CT18 [122] and MSHT20 [123], with one central replica and 58 and 64 (respectively) variations in the space of parameters. The

Table 8.4: A list of m_W fit results with variations in the fit range around the default $p_T^{\text{min}} = 28\,\text{GeV}$ and $p_T^{\text{min}} = 52\,\text{GeV}$. The second column reports the χ^2 values, the third column reports the shifts in m_W with respect to the default fit and the third column lists the statistical uncertainties on m_W.

Change to fit range	χ^2_{tot}/ndf	δm_W [MeV]	$\sigma(m_W)$ [MeV]
$p_T^{\text{min}} = 24\,\text{GeV}$	94.4/122	+6.8	19.7
$p_T^{\text{min}} = 26\,\text{GeV}$	95.9/102	+9.6	20.9
$p_T^{\text{min}} = 30\,\text{GeV}$	102.7/102	+3.0	25.7
$p_T^{\text{min}} = 32\,\text{GeV}$	85.0/102	-21.6	30.8
$p_T^{\text{max}} = 48\,\text{GeV}$	105.0/102	-3.8	23.2
$p_T^{\text{max}} = 50\,\text{GeV}$	102.6/102	-2.1	23.0
$p_T^{\text{max}} = 54\,\text{GeV}$	96.0/102	-8.6	22.6
$p_T^{\text{max}} = 56\,\text{GeV}$	103.4/102	-14.3	22.4

Table 8.5: A list of m_W fit results with variations in which physics parameters are floating.

Configuration change	χ^2_{tot}/ndf	δm_W [MeV]	$\sigma(m_W)$ [MeV]
$2 \to 3$ floating α_s params	103.3/101	-6.0	$\pm$ 23.1
$2 \to 1$ floating α_s param	128.2/103	+37.8	$\pm$ 21.1
$2 \to 1$ α_s and $1 \to 2$ k_T^{intr} params	116.0/102	+13.9	$\pm$ 22.4
$1 \to 2$ floating k_T^{intr} params	103.6/101	+0.4	$\pm$ 22.7
$1 \to 3$ floating k_T^{intr} params	102.6/100	-2.7	$\pm$ 22.9
Fixed $f(A_3) = 1$	105.3/103	+4.4	$\pm$ 22.2
Floating QCD background asymmetry	103.7/101	-0.7	$\pm$ 22.7

nominal events (generated with NNPDF3.1) are reweighted to match the description of a specific replica of a certain PDF set. The weight has the following form:

$$w_{\text{PDF}} = \frac{x_1 f(\text{id}_1, x_1, Q^2) \cdot x_2 f(\text{id}_2, x_2, Q^2)|_{\text{target}}}{x_1 f(\text{id}_1, x_1, Q^2) \cdot x_2 f(\text{id}_2, x_2, Q^2)|_{\text{nominal}}}, \tag{8.2}$$

where $\text{id}_{1,2}$ and $x_{1,2}$ are respectively the PDG identification number and Bjorken-x of the partons participating in the vector boson production, and f are the values of the PDFs calculated for a particular parton species at a given x and Q^2. This procedure is found to be, in first approximation, equivalent to the reweighting performed internally by POWHEG during the event generation, but it has the advantage of being less time consuming. New model histograms for the unpolarised

Table 8.6: The uncertainty in the determination of m_W for the NNPDF3.1, CT18NLO and MSHT20 PDF sets. The first column reports the shift in m_W with respect to the result based on the NNPDF3.1 set.

Set	δm_W [MeV]	$\sigma_{\text{PDF,base}}$ [MeV]	$\sigma_{\text{PDF},\alpha_s}$ [MeV]	σ_{PDF} [MeV]
NNPDF3.1	—	±8.3	±2.4	±8.6
CT18NLO	−11.0	±11.5	±1.4	±11.6
MSHT20	−12.0	±6.5	±2.1	±6.8

cross-section are filled with the weighted events, and then passed to the m_W fit. Table 8.6 shows the uncertainty in the determination of m_W for each PDF set. The metric used to evaluate the uncertainties of the replica variations are different, accordingly to the method used to construct each PDF set. In particular:

- for NNPDF3.1 the RMS of the shifts in m_W for the full set of 100 replicas is used;
- for CT18NLO the master formula [124], taking into account that the variations in the eigenvector space are given at 90% confidence level, is used. This means dividing the overall uncertainty by a factor 1.645;
- for the MSHT20 PDF set the nominal master formula (i.e. excluding the 1.645 factor) is used.

For each PDF set, the uncertainty from the replica variations is added in quadrature to the uncertainty from variations in the α_s values used in the PDF sets. Two variations of α_s - 0.116 and 0.120 (i.e. above and below the nominal choice of $\alpha_s = 0.118$) - are considered, and the uncertainty on m_W is taken as half of the absolute difference between the corresponding shifts in m_W [125].

Figure 8.5 shows the scatter graph of χ^2 versus m_W obtained with all the members of the considered PDF sets. For each PDF set, the plot reports the value of m_W for the central member (black points) with the associated error (as listed in Table 8.6).

Since the three PDF sets considered are equally reliable, the individual m_W results from the different PDF sets are reported independently. A “central” result is defined as the simple arithmetic mean of the three. The PDF uncertainties for

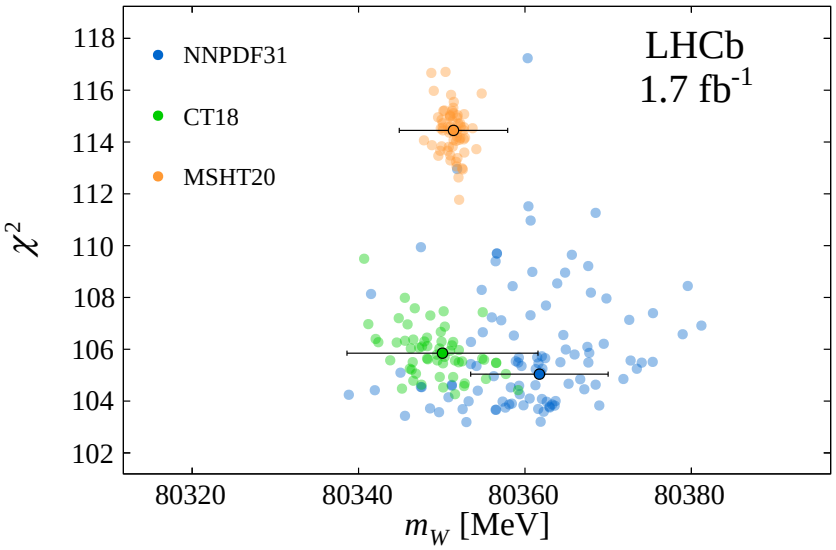

Figure 8.5: The χ^2 versus δm_W distribution including all PDF variations considered for the NNPDF3.1, CT18NLO and MSHT20 PDF sets.

the three sets are taken as fully correlated when performing this average, since the datasets used to derive them are largely the same. The PDF uncertainty of the central result is just the arithmetic mean of the three uncertainties as well, and it is found to be 9 MeV, as reported in Table 8.2.

8.7 Results

The W boson mass is measured for the first time at LHCb using roughly 1.7 fb^{-1} of data recorded during the year 2016. A simultaneous fit is performed on the q/p_T distribution of a sample of $W \to \mu\nu$ decays and the ϕ^* distribution of a sample of $Z \to \mu\mu$ decays. The value of m_W is determined to be [10]

$$m_W = 80362 \pm 23_{\text{stat}} \pm 10_{\text{exp}} \pm 17_{\text{theory}} \pm 9_{\text{PDF}} \text{ MeV},$$
$$m_W = 80351 \pm 23_{\text{stat}} \pm 10_{\text{exp}} \pm 17_{\text{theory}} \pm 12_{\text{PDF}} \text{ MeV},$$
$$m_W = 80350 \pm 23_{\text{stat}} \pm 10_{\text{exp}} \pm 17_{\text{theory}} \pm 7_{\text{PDF}} \text{ MeV},$$

using models based on the NNPDF3.1, CT18NLO and MHST20 PDF sets, respectively. The first uncertainty is statistical, the second is due to experimental systematic uncertainties, while the third and fourth are due to uncertainties

on the theoretical modelling and the PDFs. Treating these three sets equally the average result

$$m_W = 80354 \pm 23_{\text{stat}} \pm 10_{\text{exp}} \pm 17_{\text{theory}} \pm 9_{\text{PDF}} \text{ MeV},$$

is reported. The measured value of m_W is consistent with the current PDG average of direct measurements [6] and with the Global Electroweak Fit result [1]. Adding in quadrature the statistical uncertainty with the various systematic uncertainties yields a total uncertainty of about 32 MeV.

8.8 Prospects for future measurements of m_W at LHCb and the LHC

The proof-of-principle measurement of m_W described in this thesis lays the foundation for future measurements at LHCb, in particular the upcoming measurement with the full Run 2 dataset. This measurement is expected to benefit from more precise theory predictions on, for example, the angular coefficients, since DYTurbo at $\mathcal{O}(\alpha_s^3)$ recently became fully available. On the experimental side, future measurements plan to extend the $2.2 < \eta < 4.4$ fiducial region used in the m_W fit. This will require a much better control of the alignment and momentum scale calibration at the detector edges. Measurements of m_W in Run 3 will also benefit from a new magnetic field map, which aims at improving the description of the magnetic field below the $\eta = 2.2$ threshold. Finally, Ref. [9] shows that replacing the one-dimensional fit with a fit of the two-dimensional muon p_T versus η distribution could reduce the PDF uncertainty by roughly a factor of two. Therefore, this is another possible refinement that could be implemented for future measurements. The combination of measurements of m_W between LHC experiments and with the Tevatron results is highly awaited to finally reach enough precision to compare the results of direct measurements with the Global Electroweak Fit predictions.

Conclusion

This thesis has presented the first measurement of the W boson mass with the LHCb experiment at the Large Hadron Collider, using data collected in the year 2016 in pp collisions at centre-of-mass-energy $\sqrt{s} = 13\,\text{TeV}$. A simultaneous fit is performed on the q/p_T distribution of a sample of $W \to \mu\nu$ decays and the ϕ^* distribution of a sample of $Z \to \mu\mu$ decays. The value of m_W is determined to be

$$m_W = 80354 \pm 23_{\text{stat}} \pm 10_{\text{exp}} \pm 17_{\text{theory}} \pm 9_{\text{PDF}}\ \text{MeV},$$

based on an average of results with the NNPDF3.1, CT18 and MHST20 Parton Distribution Function sets. The measured value of m_W is consistent with the current PDG average of direct measurements and with the Global Electroweak Fit result. Figure 8.6 shows how the measured value compares to other published results, including measurements from the LEP experiments ALEPH, DELPHI, L3 and OPAL, the Tevatron collider experiments CDF and D0 and the ATLAS experiment at the LHC. The current prediction of m_W from the Global Electroweak Fit is also included. Even though a combination of the direct measurements shown in this plot will reduce the uncertainty on the m_W determination, more improvements are needed to ensure a fair comparison with the Standard Model prediction.

This thesis described the general strategy of the measurement of m_W, the challenges of the modelling of the observed distributions with the simulation, and the tools developed to reduce the main sources of systematic uncertainty. Particular attention has been given to the experimental challenges of the measurement. A precise knowledge of the muon momentum scale is crucial, and this is limited by the presence of mis-alignment effects in the data which are particularly complicated to solve due to the high p_T nature of the tracks involved. This thesis presented a detailed study of these mis-alignment trends in a sample of $Z \to \mu\mu$ data

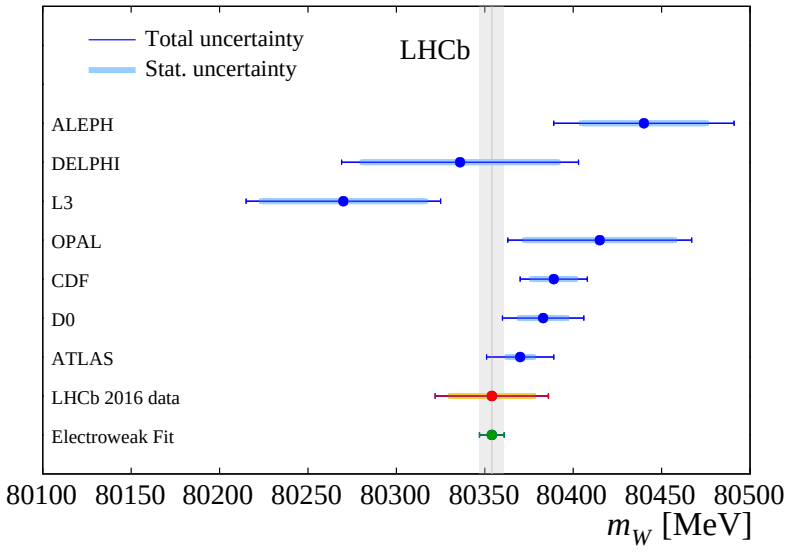

Figure 8.6: The measured value of m_W by LHCb with 2016 data compared to other published results, including measurements from the LEP experiments ALEPH, DELPHI, L3 and OPAL, the Tevatron collider experiments CDF and D0 and the ATLAS experiment at the LHC. The current prediction of m_W from the Global Electroweak Fit is also included.

collected by LHCb at $\sqrt{s} = 13\,\text{TeV}$. A method to solve the observed mis-alignment trends has also been presented and validated on a sample of simulated events. The full calculation of the uncertainty in the m_W determination due to the muon momentum measurement model has been reported. The improvements in the alignment and momentum scale calibration were fundamental in reducing this source of uncertainty down to less than 10 MeV. The modelling of the W and Z transverse momentum distribution dominates the total systematic uncertainty. Large contributions also arise from the modelling of the vector bosons decay process (via the Drell-Yan angular coefficients) and the PDFs. The theory uncertainty is found to be larger than the experimental one.

The proof-of-principle measurement of m_W presented in this thesis lays the foundation for the "legacy" measurement of m_W at LHCb with the full 13 TeV dataset. Future challenges will involve a more detailed understanding and control of the muon momentum scale for high p_T tracks, especially in those regions of the LHCb detector where the magnetic field determination is less accurate. On the theoretical side, greater improvement in the prediction of the angular coefficients

is also anticipated by the theory community for the next years. This thesis also presents the results of a standalone study which is potentially of interest for future measurements of m_W. It was observed that a fit to the double differential muon p_T versus η distribution, with the application of a PDF replica weighting procedure, can reduce the PDF uncertainty by roughly a factor of two with respect to a simple muon p_T fit. The study was based only on simulated events. The proposed two-dimensional fit approach could be tested on real data to understand its effective impact on the legacy measurement.

The total uncertainty on the measurement of m_W using only 2016 data is around 32 MeV. Given the encouraging results presented in this thesis, it is estimated that with the full 13 TeV dataset the legacy measurement of m_W could achieve the statistical precision of around 10 MeV and a target total uncertainty lower than 20 MeV. The measurement of m_W at LHCb could positivelly contribute to the combination of measurements with the ATLAS and CMS experiments at the LHC, since preliminary studies show that some of the systematic uncertainties are partially anti-correlated.

Finally, LHCb will enter a new data taking era in 2022. This thesis reported a brief description of the changes in the detector commissioned for the Upgrade I, as well as the important efforts made by the Oxford LHCb group, CERN, and other institutes in the upgrade of the new RICH1 detector. The new data taking phase, denoted as Run 3, will also be crucial for future measurements of m_W and other electroweak observables. Since much larger datasets are expected to be collected, a new level of precision for electroweak tests will be achievable.

Appendices

A

Event selection criteria used in the W mass measurement

This appendix reports the selection criteria for the sample of $W \to \mu\nu$, $Z \to \mu\mu$, $J/\psi \to \mu\mu$ and $\Upsilon(\mathrm{U1S}) \to \mu\mu$ events used in the W mass measurement presented in this thesis.

Table A.1: The Υ selection cuts used in the analysis.

Description	Cut
Mass	$\mathrm{Abs}(M - 9.460)/\mathrm{GeV} < 0.05$
Transverse momentum	Both muons with $p_T > 3\,\mathrm{GeV}$
Momentum error	Both muons with $\sigma(P)/P < 0.06$
Sanity check	Both muons with $P < 2000\,\mathrm{GeV}$
Trigger	Either muon passes `L0Muon`
Pseudorapidity	Both muons with $1.7 < \eta < 5$
Track quality	Both muons with $\chi^2_{\mathrm{trk}}/\mathrm{ndf} < 1.8$

Table A.2: The J/ψ selection cuts used in the analysis.

Description	Cut
Mass	$\text{Abs}(M - 3.097)/\text{GeV} < 0.02$
Transverse momentum	Both muons with $p_T > 3\,\text{GeV}$
Momentum error	Both muons with $\sigma(P)/P < 0.06$
Sanity check	Both muons with $P < 2000\,\text{GeV}$
Trigger	Either muon passes `L0Muon`
Pseudorapidity	Both muons with $1.7 < \eta < 5$
Track quality	Both muons with $\chi^2_{\text{trk}}/\text{ndf} < 1.8$
TT clusters	Both muons with number of TT clusters > 0

Table A.3: The W selection cuts used in the analysis.

Description	Cut
Z veto	second muon with $2.0 < \eta < 4.5$, $p_T < 25\,\text{GeV}$
Momentum error	$\sigma(P)/P < 0.06$
Sanity check	$P < 2000\,\text{GeV}$
Trigger	Passes `L0MuonEW`, `HLT1` and `HLT2`
Pseudorapidity	$2.2 < \eta < 4.4$
Hits in TT	TTClusters>0
Impact Parameter quality	$\chi^2_{\text{IP}}/\text{ndf} < 9$
Track quality	$\chi^2_{\text{trk}}/\text{ndf} < 1.8$
Energy deposit in HCAL	$E_T^{\text{HCAL}}/\text{GeV} < 5$
Isolation	$\mathcal{I}^{\text{PF},0.4}/\text{GeV} < 4$

Table A.4: The Z selection cuts used in the analysis.

Description	Cut
Mass	$91 - 14 < M/\text{GeV} < 91 + 14$
Transverse momentum	Both muons with $p_T > 20\,\text{GeV}$
Momentum error	Both muons with $\sigma(P)/P < 0.06$
Sanity check	Both muons with $P < 2000\,\text{GeV}$
Trigger	Either muon passes `L0MuonEW`, `HLT1` and `HLT2`
Pseudorapidity	Both muons with $1.7 < \eta < 5$
Isolation	Both muons with $\mathcal{I}^{\text{PF},0.4}/\text{GeV} < 10$
Energy deposit in HCAL	Both muons with $E_T^{\text{HCAL}}/\text{GeV} < 10$
Impact Parameter quality	Both muons with $\chi^2_{\text{IP}} < 100$
Track quality	Both muons with $\chi^2_{\text{trk}}/\text{ndf} < 3$

B

Additional plots on the muon momentum calibration

Chapter 7 reports the calibration of the muon momenta in simulated events, which represents an essential part of the measurement of m_W. In particular, Fig. 7.10 shows the dimuon invariant masses for Z, $\Upsilon(1S)$ and J/ψ resonance for events with both muons in the $2.2 < \eta < 4.4$ region, but the full set of plots corresponding to the mass categories entering the momentum scale fit are not reported. For completeness, they are presented in this appendix. Figure B.1 shows the postfit projections for Z events split by magnet polarity in six mass categories as specified in Table 7.1. Categories 4, 5, 6 are further split into three bins of the muon momentum asymmetry (A_P), to enhance the sensitivity of the fit to curvature biases. Figure B.2 shows the postfit projections for $\Upsilon(1S)$ and J/ψ in categories 4, 5, 6 split by magnet polarity. The split in bins of A_P is adopted only for the Z sample, since the majority of the sensitivity to curvature biases is given by high-momentum tracks. Each plot shows the dimuon invariant mass distributions for data (black), simulation *before* applying any smearing corrections (red) and *after* the smearing corrections derived from the fit (light blue template, with the background component shown in orange).

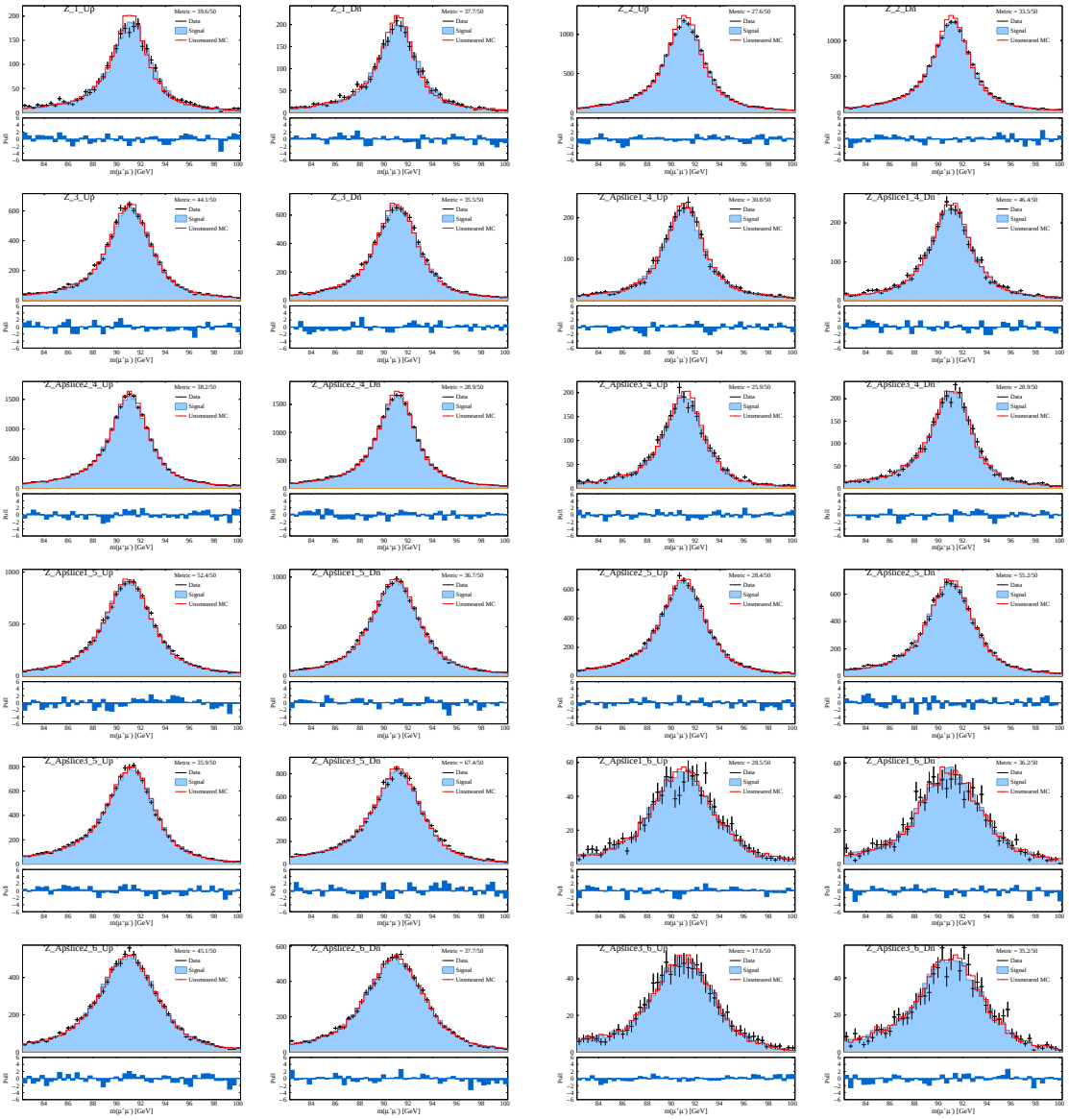

Figure B.1: The dimuon invariant mass distributions for the Z sample in each of the fiducial categories described in the text, for data (in black), unsmeared simulated events (red) and smeared simulated events using the best-fit corrections (light blue template, with the background component shown in orange).

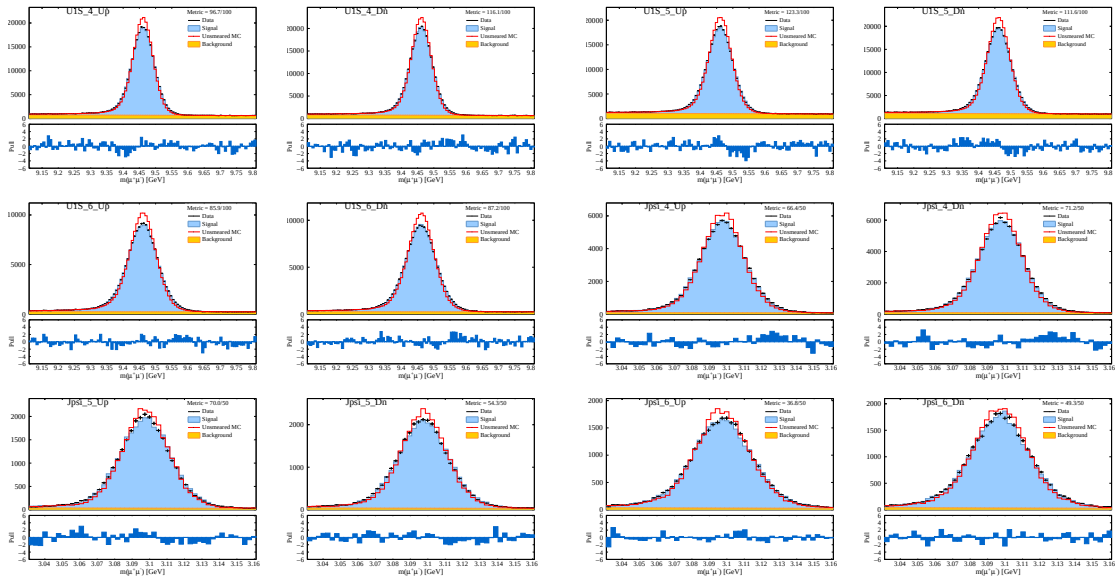

Figure B.2: The dimuon invariant mass distributions for the quarkonia samples in each of the fiducial categories described in the text, for data (in black), unsmeared simulated events (red) and smeared simulated events using the best-fit corrections (light blue template, with the background component shown in orange).

C

Additional information on the W mass fit configuration

In Chapter 8 the configuration of the m_W fit is discussed in detail. Tables C.1 and C.2 in this Appendix report the full list of components that are included in the fit for the Z and W terms. In Chapter 8 it is also discussed that all the fractions of fit components, except for the $W \to \mu\nu$ signal and the prompt hadron decay background, are fixed and estimated relative to the number of observed $Z \to \mu\mu$ events using the corresponding fiducial cross sections, listed in Table C.3. The fiducial selection for W and Z boson processes are the same as used in measurements of the corresponding cross-sections [121]. For all other processes the fiducial regions are obtained requiring a single muon in the region $p_T > 20$ GeV and $2 < \eta < 4.5$. The cross-sections for the rare backgrounds (e.g. $b\bar{b}$, $c\bar{c}$, top quarks, etc.) are determined using POWHEG with the `NNPDF31_nlo_as_0118` PDF set. The constraints on the fixed background fractions are calculated with the following expression:

$$f_{\text{comp}}^{\text{term}} = \frac{N_{\text{obs}}^{Z}}{N_{\text{obs}}^{W}} \times \frac{\sum w_{\text{comp}}^{\text{term}}}{\sum w_{\text{Z}}^{\text{Z}}} \times \frac{\sigma_{\text{comp}}^{\text{fid}}}{\sigma_{\text{Z}}^{\text{fid}}} \times \frac{N_{\text{Z}}^{\text{gen,fid}}}{N_{\text{comp}}^{\text{gen,fid}}}, \tag{C.1}$$

where the second factor involves the evaluation of the sum of event-by-event weights for the simulated events of the given component. The measured $Z \to \mu\mu$ cross-section is used [126]. The last two factors correspond to a luminosity ratio relative

Table C.1: Summary of the components included in the Z term in the default m_W fit configuration.

Term	Component	Fraction
Z	$Z \to \mu\mu$	Floating
Z	$Z \to \tau\tau$	Eq. C.1
Z	$t\bar{t}$ (gg)	Eq. C.1
Z	$t\bar{t}$ $(q\bar{q})$	Eq. C.1

Table C.2: Summary of the components included in the W term in the default m_W fit configuration.

Term	Component	Fraction
W	$W^+ \to \mu^+\nu$	Floating
W	$W^- \to \mu^-\nu$	Floating
W	$W^+ \to \tau^+\nu$	Eq. C.2
W	$W^- \to \tau^-\nu$	Eq. C.2
W	$Z \to \mu\mu$	Eq. C.1
W	$Z \to \tau\tau$	Eq. C.1
W	WW, WZ, ZZ	Eq. C.1
W	$t\bar{t}$ (gg)	Eq. C.1
W	$t\bar{t}$ $(q\bar{q})$	Eq. C.1
W	Single top	Eq. C.1
W	$c\bar{c}$	Eq. C.1
W	$b\bar{b}$	Eq. C.1
W	QCD background	Floating

to the number of $Z \to \mu\mu$ simulated events. The $N_{\text{comp}}^{\text{gen,fid}}$ count the numbers of simulated events in the corresponding fiducial regions. The $W \to \tau\nu$ component in the W term is constrained relative to the floating $W \to \mu\nu$ fraction ($f_{W\to\mu\nu}$):

$$f_{W\to\tau\nu} = f_{W\to\mu\nu} \times \frac{\sum w_{W\to\tau\nu}}{\sum w_{W\to\mu\nu}} \times \frac{\sigma^{\text{fid}}_{W\to\tau\nu}}{\sigma^{\text{fid}}_{W\to\mu\nu}} \times \frac{N^{\text{gen,fid}}_{W\to\mu\nu}}{N^{\text{gen,fid}}_{W\to\tau\nu}}. \tag{C.2}$$

Table C.3: The fiducial regions and cross-sections that are assumed in in the m_W fit.

Process	σ_{fid} [pb]	Fiducial region
$Z \to \mu\mu$	194.3	$p_T^\mu > 20$ GeV, $2 < \eta^\mu < 4.5$, $60 < M < 120$ GeV
$Z \to \tau\tau$	5.876	$p_T^\tau > 20$ GeV, $2 < \eta^\tau < 4.5$, $60 < M < 120$ GeV
$W \to \mu\nu$	3637	$p_T^\mu > 20$ GeV, $2 < \eta^\mu < 4.5$
$W \to \tau\nu$	632.4	$p_T^\tau > 20$ GeV, $2 < \eta^\tau < 4.5$
$\gamma^* \to \mu\mu$	1.038	$p_T^\mu > 20$ GeV, $2 < \eta^\mu < 4.5$, $20 < M < 40$ GeV
$q\bar{q} \to t\bar{t}$	2.415	$p_T^\mu > 20$ GeV, $2 < \eta^\mu < 4.5$
$gg \to t\bar{t}$	4.509	$p_T^\mu > 20$ GeV, $2 < \eta^\mu < 4.5$
tW	1.684	$p_T^\mu > 20$ GeV, $2 < \eta^\mu < 4.5$
WW	4.36	$p_T^\mu > 20$ GeV, $2 < \eta^\mu < 4.5$
$c\bar{c}$	2332	$p_T^\mu > 14$ GeV, $2 < \eta^\mu < 4.5$
$b\bar{b}$	1.063e+04	$p_T^\mu > 14$ GeV, $2 < \eta^\mu < 4.5$

References

[1] Johannes Haller et al. “Update of the global electroweak fit and constraints on two-Higgs-doublet models”. In: *Eur. Phys. J.* C78.8 (2018), p. 675. arXiv: 1803.01853 [hep-ph].

[2] Geoffrey T J Arnison, Michael G Albrow, and Allkofer. “Intermediate-vector-boson properties at the CERN Super Proton Synchrotron collider”. In: *Europhys. Lett.* 1.CERN-EP-85-185 (Apr. 1986), 327–345. 23 p. URL: https://cds.cern.ch/record/179775.

[3] T. Aaltonen et al. “Precise measurement of the W-boson mass with the CDF II detector”. In: *Phys. Rev. Lett.* 108 (2012), p. 151803. arXiv: 1203.0275 [hep-ex].

[4] Victor Mukhamedovich Abazov et al. “Measurement of the W Boson Mass with the D0 Detector”. In: *Phys. Rev. Lett.* 108 (2012), p. 151804. arXiv: 1203.0293 [hep-ex].

[5] Morad Aaboud et al. “Measurement of the W-boson mass in pp collisions at $\sqrt{s} = 7$ TeV with the ATLAS detector”. In: *Eur. Phys. J.* C78.2 (2018). [Erratum: Eur. Phys. J.C78,no.11,898(2018)], p. 110. arXiv: 1701.07240 [hep-ex].

[6] C. Patrignani et al. “Review of Particle Physics”. In: *Chin. Phys.* C40.10 (2016), p. 100001.

[7] Jr. Alves A.Augusto et al. “The LHCb Detector at the LHC”. In: *JINST* 3 (2008), S08005.

[8] G. Bozzi, J. Rojo, and A. Vicini. “The Impact of PDF uncertainties on the measurement of the W boson mass at the Tevatron and the LHC”. In: *Phys. Rev.* D83 (2011), p. 113008. arXiv: 1104.2056 [hep-ph].

[9] Stephen Farry et al. “Understanding and constraining the PDF uncertainties in a W boson mass measurement with forward muons at the LHC”. In: *Eur. Phys. J.* C79.6 (2019), p. 497. arXiv: 1902.04323 [hep-ex].

[10] Roel Aaij et al. “Measurement of the W boson mass”. In: (Sept. 2021). arXiv: 2109.01113 [hep-ex].

[11] S.L. Glashow. “Partial Symmetries of Weak Interactions”. In: *Nucl. Phys.* 22 (1961), pp. 579–588.

[12] Steven Weinberg. “A Model of Leptons”. In: *Phys. Rev. Lett.* 19 (21 Nov. 1967), pp. 1264–1266. URL: https://link.aps.org/doi/10.1103/PhysRevLett.19.1264.

[13] Abdus Salam. “Weak and Electromagnetic Interactions”. In: *Conf. Proc. C* 680519 (1968), pp. 367–377.

[14] Nicola Cabibbo. "Unitary Symmetry and Leptonic Decays". In: *Phys. Rev. Lett.* 10 (12 June 1963), pp. 531–533. URL: https://link.aps.org/doi/10.1103/PhysRevLett.10.531.

[15] Makoto Kobayashi and Toshihide Maskawa. "CP-Violation in the Renormalizable Theory of Weak Interaction". In: *Progress of Theoretical Physics* 49.2 (Feb. 1973), pp. 652–657. eprint: https://academic.oup.com/ptp/article-pdf/49/2/652/5257692/49-2-652.pdf. URL: https://doi.org/10.1143/PTP.49.652.

[16] S. Schael et al. "Precision electroweak measurements on the Z resonance". In: *Phys. Rept.* 427 (2006), pp. 257–454. arXiv: hep-ex/0509008.

[17] James Glimm. "The Yukawa coupling of quantum fields in two dimensions. II". In: *Comm. Math. Phys.* 6.1 (1967), pp. 61–76. URL: https://projecteuclid.org:443/euclid.cmp/1103840171.

[18] M. Awramik et al. "Precise prediction for the W boson mass in the standard model". In: *Phys. Rev. D* 69 (2004), p. 053006. arXiv: hep-ph/0311148.

[19] A. Sirlin. "Radiative corrections in the $\mathrm{SU}(2)_L \times \mathrm{U}(1)$ theory: A simple renormalization framework". In: *Phys. Rev. D* 22 (4 Aug. 1980), pp. 971–981. URL: https://link.aps.org/doi/10.1103/PhysRevD.22.971.

[20] Victor Mukhamedovich Abazov et al. "Measurement of the W Boson Mass with the D0 Detector". In: *Phys. Rev. Lett.* 108 (2012), p. 151804. arXiv: 1203.0293 [hep-ex].

[21] S. Chatrchyan et al. "The CMS Experiment at the CERN LHC". In: *JINST* 3 (2008), S08004.

[22] *W-like measurement of the Z boson mass using dimuon events collected in pp collisions at* $\sqrt{s} = 7$ TeV. Tech. rep. CMS-PAS-SMP-14-007. Geneva: CERN, 2016. URL: https://cds.cern.ch/record/2139655.

[23] Georges Aad et al. "Observation of a new particle in the search for the Standard Model Higgs boson with the ATLAS detector at the LHC". In: *Phys. Lett. B* 716 (2012), pp. 1–29. arXiv: 1207.7214 [hep-ex].

[24] Serguei Chatrchyan et al. "Observation of a New Boson at a Mass of 125 GeV with the CMS Experiment at the LHC". In: *Phys. Lett. B* 716 (2012), pp. 30–61. arXiv: 1207.7235 [hep-ex].

[25] "Theoretical view of collisions and simulating them". In: *Experimental Particle Physics*. 2053-2563. IOP Publishing, 2019, 4-1 to 4–40. URL: http://dx.doi.org/10.1088/2053-2563/ab1be6ch4.

[26] S. Bailey et al. "Parton distributions from LHC, HERA, Tevatron and fixed target data: MSHT20 PDFs". In: (Dec. 2020). arXiv: 2012.04684 [hep-ph].

[27] J. Pumplin et al. "New generation of parton distributions with uncertainties from global QCD analysis". In: *JHEP* 07 (2002), p. 012. arXiv: hep-ph/0201195.

[28] Richard D. Ball et al. "Parton distributions from high-precision collider data". In: *Eur. Phys. J.* C77.10 (2017), p. 663. arXiv: 1706.00428 [hep-ph].

[29] V.N. Gribov and L.N. Lipatov. "Deep inelastic e p scattering in perturbation theory". In: *Sov. J. Nucl. Phys.* 15 (1972), pp. 438–450.

[30] Yuri L. Dokshitzer. "Calculation of the Structure Functions for Deep Inelastic Scattering and e+ e- Annihilation by Perturbation Theory in Quantum Chromodynamics." In: *Sov. Phys. JETP* 46 (1977), pp. 641–653.

[31] Guido Altarelli and G. Parisi. "Asymptotic Freedom in Parton Language". In: *Nucl. Phys. B* 126 (1977), pp. 298–318.

[32] J.C. Collins, Davison E. Soper, and George Sterman. "Transverse momentum distribution in Drell-Yan pair and W and Z boson production". In: *Nuclear Physics B* 250.1 (1985), pp. 199–224. URL: http://www.sciencedirect.com/science/article/pii/0550321385904791.

[33] A. Kulesza and W.James Stirling. "Sudakov logarithm resummation for vector boson production at hadron colliders". In: *J. Phys. G* 26 (2000), pp. 637–642. arXiv: hep-ph/9912300.

[34] Giuseppe Bozzi et al. "Production of Drell-Yan lepton pairs in hadron collisions: Transverse-momentum resummation at next-to-next-to-leading logarithmic accuracy". In: *Phys. Lett. B* 696 (2011), pp. 207–213. arXiv: 1007.2351 [hep-ph].

[35] John C. Collins and Davison E. Soper. "Angular Distribution of Dileptons in High-Energy Hadron Collisions". In: *Phys. Rev.* D16 (1977), p. 2219.

[36] M. W. Krasny et al. "$\Delta M_W \leq 10 MeV/c^2$ at the LHC: a forlorn hope?" In: *Eur. Phys. J.* C69 (2010), pp. 379–397. arXiv: 1004.2597 [hep-ex].

[37] Juan Rojo and Alessandro Vicini. "PDF uncertainties in the extraction of the W mass at LHC: a Snowmass Whitepaper". In: *Proceedings, 2013 Community Summer Study on the Future of U.S. Particle Physics: Snowmass on the Mississippi (CSS2013): Minneapolis, MN, USA, July 29-August 6, 2013*. 2013. arXiv: 1309.1311 [hep-ph]. URL: http://www.slac.stanford.edu/econf/C1307292/docs/submittedArxivFiles/1309.1311.pdf.

[38] Giuseppe Bozzi, Luca Citelli, and Alessandro Vicini. "Parton density function uncertainties on the W boson mass measurement from the lepton transverse momentum distribution". In: *Phys. Rev.* D91.11 (2015), p. 113005. arXiv: 1501.05587 [hep-ph].

[39] Seth Quackenbush and Zack Sullivan. "Parton distributions and the W mass measurement". In: *Phys. Rev.* D92.3 (2015), p. 033008. arXiv: 1502.04671 [hep-ph].

[40] Roel Aaij et al. "LHCb Detector Performance". In: *Int. J. Mod. Phys.* A30.07 (2015), p. 1530022. arXiv: 1412.6352 [hep-ex].

[41] Roel Aaij et al. "Measurement of forward W and Z boson production in pp collisions at $\sqrt{s} = 8$ TeV". In: *JHEP* 01 (2016), p. 155. arXiv: 1511.08039 [hep-ex].

[42] Roel Aaij et al. "Measurement of the forward Z boson production cross-section in pp collisions at $\sqrt{s} = 13$ TeV". In: *JHEP* 09 (2016), p. 136. arXiv: 1607.06495 [hep-ex].

[43] Roel Aaij et al. "Measurement of the forward-backward asymmetry in $Z/\gamma^* \to \mu^+\mu^-$ decays and determination of the effective weak mixing angle". In: *JHEP* 11 (2015), p. 190. arXiv: 1509.07645 [hep-ex].

[44] Giuseppe Bozzi et al. “Prospects for improving the LHC W boson mass measurement with forward muons”. In: *Eur. Phys. J.* C75.12 (2015), p. 601. arXiv: 1508.06954 [hep-ex].

[45] *Impact of the LHCb upgrade detector design choices on physics and trigger performance*. Tech. rep. LHCb-PUB-2014-040. CERN. URL: https://cds.cern.ch/record/1748643.

[46] Roel Aaij et al. “Physics case for an LHCb Upgrade II - Opportunities in flavour physics, and beyond, in the HL-LHC era”. In: (2018). arXiv: 1808.08865.

[47] Simone Alioli et al. “NLO vector-boson production matched with shower in POWHEG”. In: *JHEP* 07 (2008), p. 060. arXiv: 0805.4802 [hep-ph].

[48] Jun Gao et al. “CT10 next-to-next-to-leading order global analysis of QCD”. In: *Phys. Rev.* D89.3 (2014), p. 033009. arXiv: 1302.6246 [hep-ph].

[49] Torbjorn Sjostrand, Stephen Mrenna, and Peter Z. Skands. “PYTHIA 6.4 Physics and Manual”. In: *JHEP* 05 (2006), p. 026. arXiv: hep-ph/0603175 [hep-ph].

[50] Robert Thorne et al. “MMHT 2014 Parton Distributions Functions”. In: *PoS* DIS2015 (2015), p. 056.

[51] Tie-Jiun Hou et al. “Reconstruction of Monte Carlo replicas from Hessian parton distributions”. In: *JHEP* 03 (2017), p. 099. arXiv: 1607.06066 [hep-ph].

[52] Roel Aaij et al. “Measurement of forward W and Z boson production in pp collisions at $\sqrt{s} = 8$ TeV”. In: *JHEP* 01 (2016), p. 155. arXiv: 1511.08039 [hep-ex].

[53] Elisabetta Manca et al. “About the rapidity and helicity distributions of the W bosons produced at LHC”. In: *JHEP* 12 (2017), p. 130. arXiv: 1707.09344 [hep-ex].

[54] Albert M Sirunyan et al. “Measurements of the W boson rapidity, helicity, double-differential cross sections, and charge asymmetry in pp collisions at $\sqrt{s} =$ 13 TeV”. In: *Phys. Rev. D* 102.9 (2020), p. 092012. arXiv: 2008.04174 [hep-ex].

[55] Richard D. Ball et al. “Reweighting NNPDFs: the W lepton asymmetry”. In: *Nucl. Phys.* B849 (2011). [Erratum: Nucl. Phys.B855,927(2012)], pp. 112–143. arXiv: 1012.0836 [hep-ph].

[56] Richard D. Ball et al. “Reweighting and Unweighting of Parton Distributions and the LHC W lepton asymmetry data”. In: *Nucl. Phys.* B855 (2012), pp. 608–638. arXiv: 1108.1758 [hep-ph].

[57] J Pumplin et al. “Uncertainties of predictions from parton distribution functions. II. The Hessian method”. In: *Physical Review D* 65 (Feb. 2001).

[58] Olli Lupton and Mika Vesterinen. “Simultaneously determining the $W^{\pm}$ boson mass and parton shower model parameters”. In: (2019). arXiv: 1907.09958 [hep-ex].

[59] Roel Aaij et al. “Design and performance of the LHCb trigger and full real-time reconstruction in Run 2 of the LHC”. In: *JINST* 14.04 (2019), P04013. arXiv: 1812.10790 [hep-ex].

[60] S et. al. Amato. *LHCb magnet: Technical Design Report*. Technical Design Report LHCb. Geneva: CERN, 2000. URL: https://cds.cern.ch/record/424338.

[61] Martina Pili. "Performance of the LHCb detector in the Run 2". In: *PoS* ICHEP2020 (2021), p. 767.

[62] Christian Lippmann. "Particle identification". In: *Nucl. Instrum. Meth. A* 666 (2012), pp. 148–172. arXiv: 1101.3276 [hep-ex].

[63] A Arefev et al. *Beam Test Results of the LHCb Electromagnetic Calorimeter.* Tech. rep. LHCb-2007-149. CERN-LHCb-2007-149. revised version submitted on 2008-05-15 09:09:53. Geneva: CERN, May 2008. URL: https://cds.cern.ch/record/1103500.

[64] C Coca et al. *The hadron calorimeter prototype beam-test results.* Tech. rep. LHCb-2000-036. Geneva: CERN, Oct. 2000. URL: https://cds.cern.ch/record/691519.

[65] Roel Aaij and Johannes Albrecht. *Muon triggers in the High Level Trigger of LHCb.* Tech. rep. LHCb-PUB-2011-017. CERN-LHCb-PUB-2011-017. Geneva: CERN, Sept. 2011. URL: https://cds.cern.ch/record/1384386.

[66] F. Archilli et al. "Performance of the Muon Identification at LHCb". In: *JINST* 8 (2013), P10020. arXiv: 1306.0249 [physics.ins-det].

[67] Roel *et al.* Aaij. "Design and performance of the LHCb trigger and full real-time reconstruction in Run 2 of the LHC. Performance of the LHCb trigger and full real-time reconstruction in Run 2 of the LHC". In: *JINST* 14.arXiv:1812.10790. 04 (2018).

[68] *The LHCb Moore project.* https://lhcbdoc.web.cern.ch/lhcbdoc/moore/. Accessed: 2020-01-08.

[69] S Borghi. "Novel real-time alignment and calibration of the LHCb detector and its performance". In: *Nucl. Instrum. Methods Phys. Res., A* 845 (2017), 560–564. 5 p. URL: https://cds.cern.ch/record/2291110.

[70] Sean Benson et al. "The LHCb Turbo Stream". In: *Journal of Physics: Conference Series* 664.8 (Dec. 2015), p. 082004. URL: https://doi.org/10.1088/1742-6596/664/8/082004.

[71] *The LHCb Brunel project.* https://lhcbdoc.web.cern.ch/lhcbdoc/brunel/. Accessed: 2020-01-08.

[72] *The LHCb DaVinci project.* https://lhcbdoc.web.cern.ch/lhcbdoc/davinci/. Accessed: 2020-01-08.

[73] Rene Brun and Fons Rademakers. ""ROOT — An object oriented data analysis framework"". In: *Nuclear Instruments and Methods in Physics Research Section A: Accelerators, Spectrometers, Detectors and Associated Equipment* 389.1 (1997). New Computing Techniques in Physics Research V, pp. 81–86. URL: http://www.sciencedirect.com/science/article/pii/S016890029700048X.

[74] Piotr Golonka and Zbigniew Was. "PHOTOS Monte Carlo: A Precision tool for QED corrections in Z and W decays". In: *Eur. Phys. J.* C45 (2006), pp. 97–107. arXiv: hep-ph/0506026 [hep-ph].

[75] D. J. Lange. "The EvtGen particle decay simulation package". In: *Nucl. Instrum. Meth.* A462 (2001), pp. 152–155.

[76] S. Agostinelli et al. "GEANT4: A Simulation toolkit". In: *Nucl. Instrum. Meth.* A506 (2003), pp. 250–303.

[77] I. Belyaev et al. “Handling of the generation of primary events in Gauss, the LHCb simulation framework”. In: *J. Phys. Conf. Ser.* 331 (2011), p. 032047.

[78] M. Gandelman and Eric Van Herwijnen. “Data quality check procedures and tools for Monte Carlo production”. In: (Dec. 2003).

[79] *Framework TDR for the LHCb Upgrade: Technical Design Report*. Tech. rep. CERN-LHCC-2012-007. LHCb-TDR-12. Apr. 2012. URL: https://cds.cern.ch/record/1443882.

[80] Massimiliano Fiorini. “The upgrade of the LHCb RICH detectors”. In: *Nuclear Instruments and Methods in Physics Research Section A: Accelerators, Spectrometers, Detectors and Associated Equipment* 952 (2020). 10th International Workshop on Ring Imaging Cherenkov Detectors (RICH 2018), p. 161688. URL: https://www.sciencedirect.com/science/article/pii/S0168900218318011.

[81] Massimiliano Fiorini. “The upgrade of the LHCb RICH detectors”. In: *Nuclear Instruments and Methods in Physics Research Section A: Accelerators, Spectrometers, Detectors and Associated Equipment* 952 (2020). 10th International Workshop on Ring Imaging Cherenkov Detectors (RICH 2018), p. 161688. URL: http://www.sciencedirect.com/science/article/pii/S0168900218318011.

[82] U.S. Military Performance Specification. “General specification governing the manufacturing, assembly, and inspection of Optical Components for Fire Control Instruments (Mil-PRF-13830B)”. In: (1997).

[83] C. Frei. *LHCb/RICH1: Quartz Windows - Inspection of the delivered panes*. EDMS-2081707-v0-Quartz-Window-Inspection-CF190125-1620.docx, Date: 25/01/2019.

[84] H. Bach and N. Neuroth. *The Properties of Optical Glass*. Springer Verlag, 1998.

[85] Heraeus. *Spectrosil*. https://www.photonicsonline.com/doc/synthetic-fused-silica-spectrosil-0001. [Online; accessed 19 Feb. 2019].

[86] Perkin Elmer. *Reliable results and high performance for demanding situations*. https://www.perkinelmer.com/lab-solutions/resources. Accessed 2019-01-10.

[87] Venkata Sai Kiran Chakravadhanula. *Vapor phase deposition of functional nanocomposite thin films and their modification by ion beam irradiation*. https://www.researchgate.net/publication/216107753_Vapor_phase_deposition_of_functional_nanocomposite_thin_films_and_their_modification_by_ion_beam_irradiation. PhD Thesis, 2011.

[88] Edmund Optics. *Laser Optics Resource Guide, Sec. 9.3*. https://www.edmundoptics.co.uk/knowledge-center/application-notes/lasers/laser-optics-resource-guide/. [Online; accessed 2 Dec 2020].

[89] *Understanding Surface Quality Specifications*. https://www.edmundoptics.co.uk/knowledge-center/application-notes/lasers/understanding-surface-quality-specifications/. Accessed: 2020-01-08.

[90] *Status of LHCb Upgrade I.* https://lhcb.web.cern.ch/lhcb_page/lhcb_documents/progress/Source/RRB/April_2021/CERN-RRB-2021-041.pdf. CERN-RRB-2021-041.

[91] Thomas Becher and Matthias Neubert. "Drell-Yan Production at Small q_T, Transverse Parton Distributions and the Collinear Anomaly". In: *Eur. Phys. J.* C71 (2011), p. 1665. arXiv: 1007.4005 [hep-ph].

[92] Giuseppe Bozzi et al. "Production of Drell-Yan lepton pairs in hadron collisions: Transverse-momentum resummation at next-to-next-to-leading logarithmic accuracy". In: *Phys. Lett.* B696 (2011), pp. 207–213. arXiv: 1007.2351 [hep-ph].

[93] R. Gauld et al. "Precise predictions for the angular coefficients in Z-boson production at the LHC". In: *JHEP* 11 (2017), p. 003. arXiv: 1708.00008 [hep-ph].

[94] Stefano Camarda et al. "DYTurbo: Fast predictions for Drell-Yan processes". In: (2019). arXiv: 1910.07049 [hep-ph].

[95] Georges Aad et al. "Measurement of the angular coefficients in Z-boson events using electron and muon pairs from data taken at $\sqrt{s} = 8$ TeV with the ATLAS detector". In: *JHEP* 08 (2016), p. 159. arXiv: 1606.00689 [hep-ex].

[96] Stefano Catani et al. "Vector boson production at hadron colliders: a fully exclusive QCD calculation at NNLO". In: *Phys. Rev. Lett.* 103 (2009), p. 082001. arXiv: 0903.2120 [hep-ph].

[97] Keith Hamilton, Paolo Nason, and Giulia Zanderighi. "MINLO: Multi-Scale Improved NLO". In: *JHEP* 10 (2012), p. 155. arXiv: 1206.3572 [hep-ph].

[98] S. Farry and M. A. Vesterinen. "Study of Final State Radiation in Electroweak Boson decays at LHCb". In: *CERN-LHCb-INT-2020-023* (CERN, Geneva, 2020.).

[99] Johannes Bellm et al. "Herwig 7.0/Herwig++ 3.0 release note". In: *Eur. Phys. J.* C76.4 (2016), p. 196. arXiv: 1512.01178 [hep-ph].

[100] Stefan Höche and Stefan Prestel. "The midpoint between dipole and parton showers". In: *Eur. Phys. J. C* 75.9 (2015), p. 461. arXiv: 1506.05057 [hep-ph].

[101] Nadine Fischer et al. "Vincia for Hadron Colliders". In: *Eur. Phys. J. C* 76.11 (2016), p. 589. arXiv: 1605.06142 [hep-ph].

[102] T. W. Anderson and D. A. Darling. "Asymptotic Theory of Certain "Goodness of Fit" Criteria Based on Stochastic Processes". In: *The Annals of Mathematical Statistics* 23.2 (1952), pp. 193–212. URL: https://doi.org/10.1214/aoms/1177729437.

[103] Rolf Hagedorn. "Multiplicities, p_T Distributions and the Expected Hadron $\rightarrow$ Quark - Gluon Phase Transition". In: *Riv. Nuovo Cim.* 6N10 (1983), pp. 1–50.

[104] A. Bodek et al. "Extracting Muon Momentum Scale Corrections for Hadron Collider Experiments". In: *Eur. Phys. J. C* 72 (2012), p. 2194. arXiv: 1208.3710 [hep-ex].

[105] Timo Antero Aaltonen et al. "Indirect measurement of $\sin^2\theta_W$ (or M_W) using $\mu^+\mu^-$ pairs from γ^*/Z bosons produced in $p\bar{p}$ collisions at a center-of-momentum energy of 1.96 TeV". In: *Phys. Rev. D* 89.7 (2014), p. 072005. arXiv: 1402.2239 [hep-ex].

[106] Albert M. Sirunyan et al. “Measurement of the weak mixing angle using the forward-backward asymmetry of Drell-Yan events in pp collisions at 8 TeV”. In: *Eur. Phys. J. C* 78.9 (2018), p. 701. arXiv: 1806.00863 [hep-ex].

[107] William Barter, Martina Pili, and Mika Vesterinen. “A simple method to determine charge-dependent curvature biases in track reconstruction in hadron collider experiments”. In: *Eur. Phys. J. C* 81.3 (2021), p. 251. arXiv: 2101.05675 [hep-ex].

[108] Peter Skands, Stefano Carrazza, and Juan Rojo. “Tuning PYTHIA 8.1: the Monash 2013 Tune”. In: *Eur. Phys. J. C* 74.8 (2014), p. 3024. arXiv: 1404.5630 [hep-ph].

[109] Victor Mukhamedovich Abazov et al. “Measurement of the ϕ^*_η distribution of muon pairs with masses between 30 and 500 GeV in 10.4 fb^{-1} of $p\bar{p}$ collisions”. In: *Phys. Rev. D* 91.7 (2015), p. 072002. arXiv: 1410.8052 [hep-ex].

[110] M. Vesterinen and T. R. Wyatt. “A Novel Technique for Studying the Z Boson Transverse Momentum Distribution at Hadron Colliders”. In: *Nucl. Instrum. Meth.* A602 (2009), pp. 432–437. arXiv: 0807.4956 [hep-ex].

[111] Tomasz Skwarnicki. “A study of the radiative cascade transitions between the Upsilon-prime and Upsilon resonances”. DESY-F31-86-02. PhD thesis. Institute of Nuclear Physics, Krakow, 1986.

[112] S. Borghi. “Novel real-time alignment and calibration of the LHCb detector and its performance”. In: *Nucl. Instrum. Meth. A* 845 (2017). Ed. by G. Badurek et al., pp. 560–564.

[113] W.D. Hulsbergen. “The global covariance matrix of tracks fitted with a Kalman filter and an application in detector alignment”. In: *Nuclear Instruments and Methods in Physics Research Section A: Accelerators, Spectrometers, Detectors and Associated Equipment* 600.2 (Mar. 2009), pp. 471–477. URL: http://dx.doi.org/10.1016/j.nima.2008.11.094.

[114] J. Amoraal et al. “Application of vertex and mass constraints in track-based alignment”. In: *Nucl. Instrum. Meth. A* 712 (2013), pp. 48–55. arXiv: 1207.4756 [physics.ins-det].

[115] M Needham and T Ruf. *Estimation of the material budget of the LHCb detector*. Tech. rep. Geneva: CERN, Mar. 2007. URL: https://cds.cern.ch/record/1023537.

[116] Roger Barlow and Christine Beeston. “Fitting using finite Monte Carlo samples”. In: *Computer Physics Communications* 77.2 (1993), pp. 219–228. URL: https://www.sciencedirect.com/science/article/pii/001046559390005W.

[117] G. A. Cowan, D. C. Craik, and M. D. Needham. “RapidSim: an application for the fast simulation of heavy-quark hadron decays”. In: *Comput. Phys. Commun.* 214 (2017), pp. 239–246. arXiv: 1612.07489 [hep-ex].

[118] Dariusz Dereniowski and Marek Kubale. “Cholesky Factorization of Matrices in Parallel and Ranking of Graphs”. In: *Parallel Processing and Applied Mathematics*. Ed. by Roman Wyrzykowski et al. Berlin, Heidelberg: Springer Berlin Heidelberg, 2004, pp. 985–992.

[119] V Fave. *Estimation of the material budget of the Inner Tracker*. Tech. rep. Geneva: CERN, Oct. 2008. URL: https://cds.cern.ch/record/1134016.

[120] Fred James and Matthias Winkler. *Minuit*. https://root.cern.ch/root/htmldoc/guides/minuit2/Minuit2.html. [Online; accessed 19 Feb. 2019].

[121] Roel Aaij et al. "Measurement of forward W and Z boson production in *pp* collisions at $\sqrt{s} = 8$ TeV". In: *JHEP* 01 (2016), p. 155. arXiv: 1511.08039 [hep-ex].

[122] Tie-Jiun Hou et al. "New CTEQ global analysis of quantum chromodynamics with high-precision data from the LHC". In: *Phys. Rev. D* 103.1 (2021), p. 014013. arXiv: 1912.10053 [hep-ph].

[123] S. Bailey et al. "Parton distributions from LHC, HERA, Tevatron and fixed target data: MSHT20 PDFs". In: (Dec. 2020). arXiv: 2012.04684 [hep-ph].

[124] J. Pumplin et al. "New generation of parton distributions with uncertainties from global QCD analysis". In: *JHEP* 07 (2002), p. 012. arXiv: hep-ph/0201195.

[125] Jon Butterworth et al. "PDF4LHC recommendations for LHC Run II". In: *J. Phys. G* 43 (2016), p. 023001. arXiv: 1510.03865 [hep-ph].

[126] Roel Aaij et al. "Measurement of the forward Z boson production cross-section in pp collisions at $\sqrt{s} = 13$ TeV". In: *JHEP* 09 (2016), p. 136. arXiv: 1607.06495 [hep-ex].